Thomas Forgber, M.Sc. B.Sc.

Resolved Simulations of Non-Isothermal Granular Flows

DISSERTATION

zur Erlangung des akademischen Grades

Doktor der technischen Wissenschaften

eingereicht an der

Technischen Universität Graz

Betreuer

Univ.-Prof. Dipl.-Ing. Dr.techn. Johannes Khinast
Institut für Prozess- und Partikeltechnik

Zweitbetreuer
Assoz. Univ.-Prof. Dr. Stefan Pirker

Graz, Mai 2017

Eidesstattliche Erklärung

Ich erkläre an Eides statt, dass ich die vorliegende Arbeit selbstständig verfasst, andere als die angegebenen Quellen/Hilfsmittel nicht benutzt, und die den benutzten Quellen wörtlich und inhaltlich entnommenen Stellen als solche kenntlich gemacht habe. Das in TUGRAZonline hochgeladene Textdokument ist mit der vorliegenden Dissertation identisch.

Datum	Unterschrift

Abstract

Computational Fluid Dynamics (CFD) and the Discrete Element Method (DEM) have been widely applied in academia and industry over the past two decades. Commercial and open-source toolboxes enable to perform coupled CFD-DEM simulations and gain insight in fundamental phenomena occurring on the particle scale. With the continuously increasing availability of computational resources, as well as advanced parallelization algorithms, detailed studies of real-world applications using these tools are nowadays in reach. However, CFD and CFD-DEM tools often do not resolve intra-particle properties (e.g., temperature or species concentration profiles), which can be of major importance for the thermal behavior of certain particulate systems. Only if all relevant physical phenomena are modeled correctly, reliable predictions of, e.g, overall reactor performance, are possible.

In this thesis, a well established framework for CFD-DEM-based simulations (i.e., *CFDEMcoupling*) is extended by the library *ParScale*. The latter is able to resolve intra-particle property profiles in beds of moving particles. Furthermore, *ParScale* can account for a wide range of modeling approaches, and is able to include chemical reactions or phase change phenomena inside the particle. Thereby, *ParScale* can be linked to a DEM solver (e.g., *LIGGGHTS*) or, in the most advanced case, a CFD-DEM solver (e.g., *CFDEMcoupling*).

These coupling capabilities add significant physics to currently available simulation tools. In the present thesis *ParScale* is coupled to *LIGGGHTS* and used to assess the importance of intra-particle temperature gradients under various flow conditions. Specifically, shear flows of non-isothermal particles are studied, and particle information is averaged to report thermal fluxes that can be used to build continuum models in future. Furthermore, a novel approach to determine radiative thermal transfer rates in coupled particle-based simulation is presented and embedded into the DEM solver *LIGGGHTS*. The relative importance of radiation as a heat transport mode is assessed for a wide range of system temperature. It is shown that the normalized radiative heat flux collapses onto a single curve if plotted versus the product of two dimensionless groups. This understanding can be used to inform the future development of a continuum formulation for predicting radiative heat fluxes in dense granular flows.

Kurzfassung

Computational Fluid Dynamics (CFD) und die Discrete Element Method (DEM) wurden in den letzten beiden Jahrzehnten von Industie und Universität verbreitet eingesetzt. Kommerzielle und öffentlich zugängliche "Simulationswerkzeugkästen" ermöglichen heutzutage gekoppelte CFD-DEM Simulationen mit großem Einblick in physikalische Abläufe. Mit kontinuierlich wachsenden Rechenressourcen und weiterentwickelten Parallelisierungsalgorithmen sind detailgetreue Studien von realen Problemen möglich. Jedoch ermöglichen diese Anwendungen oft keine Auflösung von interpartikulären Profilen (z.B., von Temperatur- oder Konzentrationsprofile), welche erheblichen Einfluss auf das thermische Verhalten granularer Systeme haben können. Nur wenn alle wichtigen Phenomäne richtig modelliert werden, sind verlässliche Aussagen im Hinblick auf, zum Beispiel, die Leistungsfähigkeit eines chemischen Reaktors, möglich.

In dieser Arbeit wird die bewährte Applikation *CFDEMcoupling* um die neue Anwendung *ParScale* erweitert. Diese ist in der Lage inter-partikuläre Profile in bewegten Partikelbetten aufzulösen. Weiterhin vereint *ParScale* eine Vielzahl von Modellierungsanzätze und ist in der Lage z.B. chemische Reaktionen und Phasenübergänge im Partikel einzubeziehen. *ParScale* kann mit einer DEM Applikation (z.B. *LIGGGHTS*) gekoppelt werden, oder, im fortgeschrittensten Fall, zusammen mit einer CFD-DEM Applikation (z.B. *CFDEMcoupling*) benutzt werden.

Diese Kopplungmöglichkeiten stellen eine erhebliche physikalische Erweiterung der Simulationswerkzeuge dar. In der vorliegenden Arbeit wird die Kopplung zwischen *ParScale* und *LIGGGHTS* genutzt um die Wichtigkeit von interpartikulären Temperaturgradienten unter unterschiedlichsten Strömungsbedingungen einzuschätzen. Speziell werden Scherströmungen von Partikeln mit unterschiedlicher Temperatur untersucht, wobei die Resultate, in Form von thermischen Flüssen, für die Formulierung eines kontinuierlichen Modelles verwendet werden können. Weiterhin wird eine neue Methode vorgestellt um Strahlung in gekoppelten Partikelsimulationen zu modellieren und diese in *LIGGGHTS* implementiert. Beschrieben wird der rellative Anteil von Strahlung als Wärmeleitmechanismus bei unterscheidlichen Systemtemperaturen. Es wird

gezeigt, dass der normierte Wärmestrom aufgrund von Strahlung nur eine Funktion des Produkt zweier dimensionloser Kennzahlen ist. Auch dieses Verständnis kann für die zukünftige Entwicklung von Kontinuums-basierten Schließbedingungen für die Vorhersage von Wärmetransport aufgrund von Strahlung in dichten granularen Strömungen eingesetzt werden.

Acknowledgement

I would like to express my gratitude to Prof. Johannes Khinast to give me an opportunity to this research and his trust to finish the thesis in time. I would like to thank my second assessor Prof. Stefan Pirker for his valuable time reading this manuscript and the kind and fruitful discussions during several conference meetings.

Special gratitude is given to Dr. Stefan Radl who was my supervisor during this thesis and spend an enormous amount of time helping me with programming, writing papers (and correcting them), reading this thesis and preparing presentations. It was not always easy, but in the end it is mainly due to his constant pushes and hard work that this thesis became possible after all.

Much gratitude goes to all the colleagues and friends at the Institute, especially the "SimuNerd@TUGraz" group (Benedict, Christian, Federico, Jakob, Sadegh, Minqiu, and our newest member Theresa) who made the time inside and outside the office much more enjoyable. More often than someone would think, the discussions directly lead to ideas that were realized within this thesis. Especially Federico dedicated a large amount of time thinking about my results (constantly complaining about the data ranges) and modeling approaches for the radiative transport.

I would also like acknowledge Christoph Kloss, Christoph Goniva and Andreas Aigner from DCS Computing for developing *CFDEMcoupling* and their fruitful input during conferences, meetings, academic trainings and co-authoring the publication.

Furthermore, I would like to thank the secretary group, namely Adela, Michaela and Silvia, not only for all the help with administrative forms, but also for the great stories during the coffee breaks.

Without Johann Grubbauer the experimental part of the thesis would not have been possible - many thanks for the help. Also, Stefan (Scheer) helped a lot, along with all the technical support.

Furthermore, I would like to thank the Continuous Processes group around Dr. Gruber-Wölfler (Bianca and Peter[2]) for creating such a friendly atmosphere to work in.

By far the biggest gratitude belongs to my parents, my whole family and my girlfriend Lea who always believed in me and behaved supportive in every image-able way. I would not be able to write these words if it was not for them.

Contents

Trademarks

LIGGGHTS® and CFDEM® are registered trademarks of DCS Computing GmbH, the producer of the LIGGGHTS® software and the CFDEM®coupling software. See www.cfdem.com for details.

OpenFOAM® is the name given to software produced by OpenCFD Ltd. and released free and open source to the general public. OpenFOAM® is a registered trade mark of OpenCFD Limited, producer and distributor of the OpenFOAM® software. See www.openfoam.com for details.

1 Introduction

Over the past two decades coupling Computational Fluid Dynamics (CFD) and the Discrete Element Method (DEM) has been widely applied in academia and industry (Wu et al. [1]). These coupling capabilities enable to resolve flow and discrete particle movement simultaneously including global force, momentum and energy balances. The active development of open-source toolboxes (e.g., Kloss et al. [2]) has drawn industrial and academic attention to CFD-DEM in a large variety of sectors. These tools combine advanced physical models with high computational efficiency, which provides a detailed understanding of granular flow behavior. New MPI/OpenMP hybrid parallelization algorithms ensure excellent scaling up to several million particles, and build the foundation for future studies and application to real-world processes (Berger et al. [3]). However, with the broad range of applications, modeling coupled thermal or chemical processes for a large ensemble of particles remains a challenging task. Typically, DEM and CFD-DEM tools do not take intra-particle transport phenomena into account. From the perspective of a researcher interested in reactive particulate systems, thermal and chemical conversion rates might significantly depend on intra-particle properties (since reaction rates may strongly depend on the local temperature and species concentration in the pores of a particle). Often, reaction rates, and consequently intra-particle profiles, play a central role in predicting the overall reactor performance (Dixon et al. [4]).

1.1 The NanoSim Project

With physical processes taking place on a certain characteristic length and time scale, they may also influence phenomena on other scales. Thus, an individual computational code might not be able to capture all rate limiting steps in a complex industrial process. The *NanoSim* project (*"A Multi-scale Simulation-Based Design Platform for Cost-Effective CO_2 Capture Processes using Nano-Structured Materials"*) aims towards the incorporation and connection of a broad range of models at different scales. Even though *NanoSim* is designed to allow the rational design of second generation gas-particle CO_2 capture technologies only,

it features generally applicable state of the art modeling approaches at each particular scale. Specifically, the open-source simulation platform (*Porto*) integrates computational codes from many different sources in order to solve related problems at five different scales. Furthermore, *NanoSim* aims on offering educational resource in computational science and engineering with particular focus on scale coupling and multi-scale modeling. One key element of *NanoSim* is *COSI* (i.e., a co-simulation tool) which combines the CFD-DEM solver *CFDEMcoupling* with the *ParScale* simulator: a tool to predict intra-particle property profiles. Fig. 1.1 outlines how this newly developed simulator integrates with the other tools involved in the co-simulation platform.

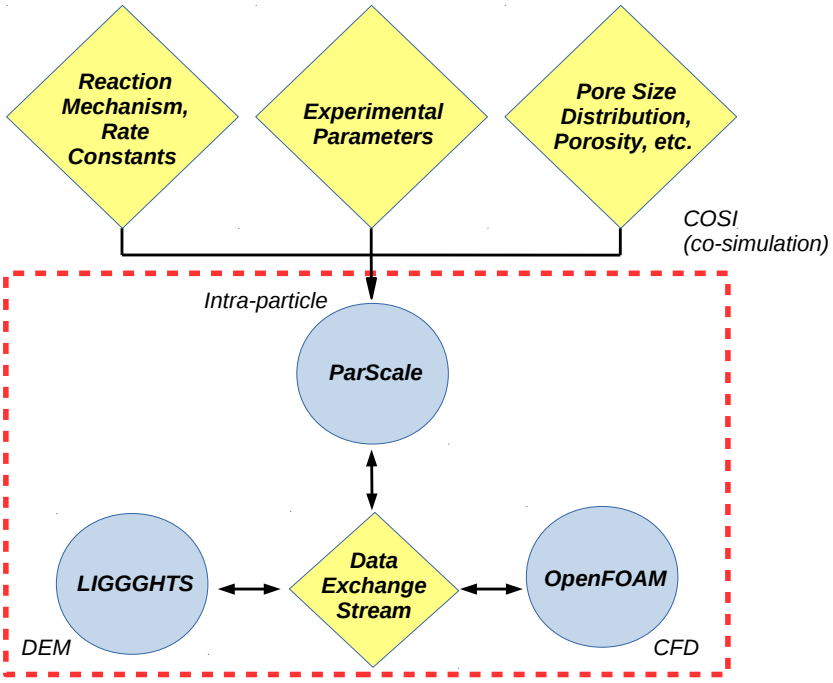

Figure 1.1: Interaction of simulators within the *COSI* simulation platform.

1.2 The ParScale Simulator

ParScale is developed within the current work, implemented in a C/C++ environment and publicly available through www.github.com [5]. At the current development state, *ParScale* contains a broad range of models that aim on predicting heat and mass transfer, as well as homogeneous and heterogeneous

reactions inside flowing porous particles. Also, it is possible to account for a single or multiple-reactions, i.e., a reaction network. Due to a modular class-based structure, and the integration into an automated test harness, easy extendibility and a high software quality is ensured. The library features run modes (i) stand-alone, (ii) coupled to a DEM solver (i.e. *LIGGGHTS*) and (iii) coupled to a CFD-DEM application (i.e. *CFDEMcoupling*). A detailed discussion of the models is available in the training material [6] accompaning the *ParScale* software. In the current state, *ParScale* is able to (i) resolve one-dimensional intra-particle property profiles (e.g., a reacting species or temperature) in spherical coordinates and (ii) perform simulations with a shrinking core model. Several physical models are implemented with focus on chemical reactions (i.e., single reactions, multi-reaction networks using input provided in CHEMKIN-II format) and phase change models (i.e., evaporation and equilibrium state approaches). For a detailed theoretical documentation the reader is referred to the comprehensive online documentation [7] and the set of verification and test cases [5].

The following Chapter outlines the goals that are addressed within the thesis, and also provides a short overview about the content of each Chapter.

1.3 Bibliography

[1] C. L. Wu, O. Ayeni, a. S. Berrouk, and K. Nandakumar. Parallel algorithms for CFD-DEM modeling of dense particulate flows. *Chemical Engineering Science*, 118:221–244, 2014.

[2] C. Kloss, C. Goniva, A. Hager, S. Amberger, and S. Pirker. Models , algorithms and validation for opensource DEM and CFD-DEM. *Progress in Computational Fluid Dynamics*, 12:140–152, 2012.

[3] R. Berger, C. Kloss, A. Kohlmeyer, and S. Pirker. Hybrid parallelization of the liggghts open-source dem code. *Powder Technology*, 278:234 – 247, 7 2015.

[4] A. G. Dixon, M. Ertan T., E. Hugh S., and M. Nijemeisland. 3D CFD simulations of steam reforming with resolved intraparticle reaction and gradients. *Chemical Engineering Science*, 62:4963–4966, 2007.

[5] https://github.com/CFDEMproject/ParScale-PUBLIC, accessed May 2017.

[6] https://www.tugraz.at/institute/ippt/downloads-software/, accessed May 2017.

[7] https://github.com/CFDEMproject/ParScale-PUBLIC/tree/master/doc/pdf, accessed May 2017.

2 Goals and Content

2.1 Goals

The present thesis follows four major goals which can be outlined as follows.

2.1.1 Goal I: Establish a new Simulation Tool

The library *ParScale* is developed, and integrated with the Discrete Element Method (DEM)-based code *LIGGGHTS*. This new simulation tool allows the resolution of intra-particle property profiles in flowing granular materials. The application of *ParScale* to such situations is presented, and important details regarding coupling algorithms, verification studies and governing equations are detailed. Finally, a careful verification is needed to support the chosen one-dimensional approach to approximate intra-particle property profiles at a manageable computational effort: also this is in the focus of the current development.

2.1.2 Goal II: Broaden the Understanding of Thermal Transport in Granular Shear Flow

We aim towards adding knowledge and understanding of thermal transport mechanisms in granular materials by considering a particle bed undergoing linear shear flow. The setup reflects that previously used by Mohan et al. [1], and relies on the widely-used Lees-Edwards boundary conditions to impose shear flow in the absence of walls [2]. Previously unexplored gaps in the parameter space are investigated by considering two additional physical phenomena: (i) non-uniform intra-particle temperature profiles caused by the finite rate of heat conduction within particles, as well as (ii) cooling of particles via the ambient fluid, i.e., non-vacuum boundary conditions. Also, focus is given on a correct calculation of thermal transport due to particle motion. Previous publications

established that granular shear flows bifurcate into three different stress regimes (Chialvo et al. [3]). Also, the significant contribution of the convective flux (Rognon et al. [4]) to the overall thermal transport rate in granular materials was previously underlined. We make an attempt to find similar scaling laws for the thermal transport by conduction, and extend the previously explored parameter space to probe the importance of convective transport for a broad range of flow situations. Thereby, all results are presented in a dimensionless manner to enable an efficient mapping into different industrial applications.

2.1.3 Goal III: Quantify Jamming and Crystallization Effects in Wall-Bounded Flows

For dense flows that may transition from an unjammed to a jammed state, it has been shown that the contact pressure fluctuates by several orders of magnitude upon such a transition (Chialvo et al. [3]). These fluctuations, together with the eigenstresses of the system, can be used to characterize the current state of a granular flow. Based on the original jamming diagrams proposed by Liu and Nagel [5], as well as the more recent work of Ciamarra et al. [6] and Brown et al. [7], we asses the thermal behavior of a granular material in case it undergoes a jamming transition. It is shown how to distinguish between jammed, unjammed and crystallized system states by purely considering the thermal behavior. Also, it is outlined how to prevent crystallization in DEM-based simulations of wall-bounded shear flows by adjusting the coefficient of friction.

2.1.4 Goal IV: Explore Radiative Heat Transfer in Dense Granular Matter

With the background of, e.g. CO_2 capturing techniques, high temperatures are relevant, and thermal transport via radiation might be the leading heat transfer mechanism. The computational cost when accounting for radiation in case of moving particles is typically very high. This is since until now primarily statistical methods have been applied (e.g., Monte Carlo or ray tracing methods) to accurately simulate how radiative energy propagates in the void space of a granular material. We show a novel way of calculating radiative thermal exchange rates in a computationally efficient way. We apply this approach to the same sheared bed of particles as used in our previous studies. Thereby, particular focus was placed on the implementation into the CPU-based DEM solver *LIGGGHTS*. Such an implementation is challenging since CPU-based

codes rely on the assumption of short distance interactions (i.e., they typically employ spatially-confined neighbor lists), whereas radiation is by definition a long range interaction phenomenon. We then aim towards a rigorous assessment of flow situations in which radiation should be accounted for or not. Also, a careful evaluation of the relative contribution of radiation on the total thermal transport rate in a granular flow is performed.

Approaching the above defined goals must follow a well-designed software implementation strategy, careful verification, testing, documentation and ultimately a transfer of the gained knowledge to the public. This was achieved by preparing screencasts and training material, which is now freely available to the public [8], [9]. The scientific work load presented above was divided into three major parts. Each part was documented in the form of a journal publication - these publications also constitute the main body of the present thesis, and a short introduction into each of them is given in the next section.

2.2 Thesis Content

2.2.1 Thermal Behaviour of Unbounded Granular Shear Flows considering Non-Uniform Intra-Particle Temperature Profiles

In Chapter 3 we aim for an assessment of the importance of intra-particle temperature profiles in granular flows utilizing a co-simulation of *LIGGGHTS* and *ParScale*. Therefore, all important governing equations are outlined, ranging from (i) the description of discrete particle motion, via (ii) the temperature distribution in a spherically-symmetric particle, to (iii) the classical Navier-Stokes equations solved in a CFD simulation. Special focus is placed on the verification if an one-dimensional approach is applicable within the current setup or not. Therefore, results from direct numerical simulations are used to substantiate this assumption. After the explanation of coupling routines between *LIGGGHTS* and *ParScale*, an analytical solution for the temperature distribution in an abstracted granular shear flow setup is presented. Subsequently, this abstraction step is verified by comparing the calculated temperature profiles with simulation data. Specifically, the numerical setup consisted of a fully periodic box filled with particles, and Lees-Edwards boundary conditions (Lees and Edwards [2]), where particles are forced to follow a predefined shear rate, were employed. The temperature gradient is enforced by a constant

particle temperature difference between the top and bottom region of the box. After reaching a statistical steady state (in terms of thermal fluxes and contact pressure), thermal fluxes are averaged and modeled over a wide range of (i) particle volume fractions, (ii) particle stiffnesses, (iii) shear speeds and (iv) Biot numbers. Scaling laws are presented, and it is shown that the conductive thermal flux (i.e., the thermal inter-particle transport rate in case of collisions) bifurcates into three regimes. This bifurcation is similar to the behavior of the contact pressure. The work was published in *Granular Matter* [10].

2.2.2 Thermal Behaviour of Wall Bounded Shear Flow during a Jamming Transition

Moving to Chapter 4, we shift our focus to a more application oriented boundary condition: we use a moving wall of constant speed to bound a granular shear flow at the top and bottom. Particles cannot cross the wall freely (in contrast to previous work), which allows us to display the transition between unjammed, jammed and crystallized states within our setup. We present a way to determine the state of the granular flow, just relying on the evaluation of the conductive flux. Also, we present trends that help to prevent crystallization by adjusting the coefficient of friction. An enhancement of up to six orders of magnitude is found for the conductive flux if a system undergoes a jamming transition. Interestingly, the convective thermal transport rate stays almost unaffected by the jamming transition. Finally, a collapse for the conductive flux over the dimensionless contact pressure is identified, which also takes transferred heat to the ambient fluid into account. The work was published in *Powder Technology* [11].

2.2.3 A Novel Approach to Model Radiation in CPU Based DEM Simulations and an Assessment of the Relative Importance of Radiative Fluxes

In Chapter 5, a novel approach for calculating radiative thermal exchange in coupled particle simulations is introduced. The algorithm is described in detail, together with the equations needed to account for radiation in a continuum-based framework, such as provided by the finite volume discrete ordinate method (fvDOM) available in *OpenFOAM*. In fact, we use fvDOM together with literature data to ensure a rigorous verification of our model. Specifically, we consider (i) a two particle setup, (ii) a three particle setup to verify shadowing effects, and (iii) a fixed bed of particles featuring a broad range of volume

fraction. The latter supports the ranges of particle concentrations considered in the subsequent studies. The model is embedded into *LIGGGHTS* and is subsequently used to perform fully periodic shear flow simulations including thermal radiation. Thereby, special focus is placed on stiff particles and high temperature levels, which are relevant for engineering applications involving reactive particles. We aim towards an assessment of regimes in which radiation plays a dominant role related to other thermal transport mechanism. We find that especially at high temperatures radiation remains the most important thermal flux to model. Last, we demonstrate a collapse onto a single curve in case we relate the radiative flux to an appropriate dimensionless group. The work has been submitted to *Powder Technology* in April 2017 [12].

Chapter 6 summarizes the presented work and identifies future challenges related to the developed software and algorithms. Ultimately, Chapter 7 contains a complete list of all peer-reviewed articles published in scientific journals and conference proceedings that were prepared during the present thesis. Also, technical reports prepared during the thesis are listed.

2.3 Bibliography

[1] B. Mohan, C. Kloss, J. Khinast, and S. Radl. Regimes of Liquid Transport through Sheared Beds of Inertial Smooth Particles. *Powder Technology*, 264:377–395, 2014.

[2] A. W. Lees and S. F. Edwards. The computer study of transport processes under extreme conditions. *Journal of Physics C: Solid State Physics*, 5:1920–1921, 1972.

[3] S. Chialvo, J. Sun, and S. Sundaresan. Bridging the rheology of granular flows in three regimes. *Physical Review E - Statistical, Nonlinear, and Soft Matter Physics*, 85:021305, 2012.

[4] P. Rognon and I. Einav. Thermal transients and convective particle motion in dense granular materials. *Phys. Rev. Lett.*, 105:218301, 2010.

[5] A. J. Liu and S. R. Nagel. Nonlinear dynamics: Jamming is not just cool any more. *Nature*, 396(6706):21–22, 1998.

[6] M. P. Ciamarra, R. Pastore, M. Nicodemi, and A. Coniglio. Jamming phase diagram for frictional particles. *Phys. Rev. E*, 84:041308, 2011.

[7] E. Brown and H. M. Jaeger. Dynamic jamming point for shear thickening suspensions. *Phys. Rev. Lett.*, 103:086001, 2009.

[8] https://www.tugraz.at/institute/ippt/downloads-software/, accessed May 2017.

[9] https://github.com/CFDEMproject/ParScale-PUBLIC/tree/master/doc/pdf, accessed May 2017.

[10] T. Forgber, B. Mohan, C. Kloss, and S. Radl. Heat transfer rates in sheared beds of inertial particles at high biot numbers. *Granular Matter*, 19(1):14, 2017.

[11] T. Forgber and S. Radl. Heat transfer rates in wall bounded shear flows near the jamming point accompanied by fluid-particle heat exchange. *Powder Technology*, 315:182 – 193, 2017.

[12] T. Forgber and S. Radl. A novel approach to calculate radiative thermal exchange in coupled particle simulations. *submitted to Powder Technology*, 2017.

3 Heat Transfer Rates in Sheared Beds of Inertial Particles at High Biot Numbers [1]

3.1 Introduction

The reliable prediction of local temperatures in reactors for, e.g., CO_2 absorption, or biomass combustion is a research field of high interest. In these reactors particles undergo thermal or chemical transformation processes such as heating, drying, gasification, combustion, or reduction. The parallel sequence of these phenomena is still not fully understood (Ding et al. [2], Rickelt et al. [3]), and often highly dependand on the local temperature gradient inside the particle [4]. When using materials with a low heat conductivity, these gradients become extremely important in order to predict, e.g., reaction fronts. These fronts may lead to a significant change of the particle properties. Also, the surrounding flow field is typically also affected.

In addition, an accurate understanding of heat flow through static (or slowly moving) granular materials is needed in various heat treatment processes, e.g., for clayed soils, or thermal granular compaction. These systems have been investigated in detail by Smart et al. [5], Shi et al. [6], or Vargas et al. [7]. Also, a hotly debated question is the heating of brittle rocks in fault gouges during earthquakes in the field of geophysics, for instance as discussed in Rice [8]. The rising temperature in these systems has a significant effect on the overall behaviour since it leads to a pressurization of the fluid, and might cause fluidization (Sulem et al. [9], Rice [8]). In the field of siliceous materials it is well known that rising temperatures even lead to grain melting as shown by Otsuki et al. [10]. A temperature rise in such particle beds can be seen even without any kind of external heat source, but just through the dissipation of

[1] This Chapter is based on [1]. T.F. has implemented parts of the computer code, set up and post-processed all simulations, formed the analytical solution and has written the manuscript.

mechanical energy, and the inability of a layer of particles to transfer heat to the environment (Alonso et al. [11]).

Many researchers (e.g. Chialvo et al. [12], Luding et al. [13]) aimed towards the development of a rheological model in the context of a continuum description of granular materials. The study of Chialvo et al. [12] can be seen as a breakthrough in these studies, since different stress regimes (and the associated transitions between these regimes) for granular flow were quantitatively described for the first time. Mohan et al. [14] showed the existence of different regimes in the context of conductive and convective liquid transport in a sheared particle bed. In this latter work similarities between the transport of thermal energy and liquid adhering to the surface of the particles have been already discussed. Thereby, a dimensionless shear rate and a Peclet number were identified as the key dimensionless parameters. Unfortunately, the work of Mohan et al. [14] relied on the assumption of zero heat flux to the ambient fluid, critically limiting the applicability of their conclusions. Recently, Morris et al. [15] made a step towards more efficient simulations by introducing correction terms that account for the artificial softening of the particles in order to correctly calculate the conductive thermal flux.

The above mentioned previous work relied on the Discrete Element Method (DEM), and mostly focussed on the rheological behaviour of granular matter. In case heat transfer was studied, typically a rather rudimentary approach for the local particle temperature distribution was adopted. Thus, often a spatially homogeneous particle temperature (i.e., no intra-particle temperature gradient) is considered. A good example for such an approach is the work of Tsory et al. [16]. Also, heat transfer to the ambient fluid is often not accounted for. For example, Rognon et al. [17], [18] did not even attempt to model the transferred heat from the particle to the ambient fluid (e.g., air), in line with the assumptions of Mohan et al. [14]. A more advanced study was perfromed by Shi et al. [6], who performed a thermally coupled CFD-DEM simulation in a rotary kiln under conduction-dominated flow conditions. Unfortunately, they used strongly simplified models for the fluid and solid phase. Most important, they also neglected intra-particle property profiles, which clearly limits the predictive capabilities of their model.

In related fields, Batchelor and O'Brien [19] obtained results for the effective conductivity of the granular material in the case of non-flowing uniform spherical particles embedded in a non-flowing matrix material. Thus, particles and the surrounding matrix were not allowed to move, and hence their analytical solution is rather limited. Shimizu [20] carried out thermal simulation using an Euler-Lagrange approach. He relied on a "thermal pipe network" to represent

heat conduction due to particle-particle interactions, and failed to resolve intra-particle temperature gradients. Cheng et al. [21] were able to model the effective conductivity of a non-moving packing by performing simulations that take (i) conduction through the solid particles, (ii) conduction through the contact area between contacting particles, and (iii) the conduction via the ambient (but stagnant) fluid into account.

Only some research groups include more refined models for the temperature distribution inside individual particles. Relevant studies include the work of Feng et al. [22], [23] or Oschmann et al. [24]. The former propose a so-called Discrete Thermal Element Model (DTEM), which can be readily integrated with the DEM. Unfortunately, also this previous work made strong simplifications, e.g., by neglecting direct heat transfer in the contact zones, or by relying on a pipe-network structure to compute thermal fluxes. The model of Oschmann et al. can be seen as the ultimate model for heat conduction within a particle bed: they discretize each particle with ca. 20,000 computational nodes, and are hence able to predict the full three-dimensional temperature distribution within each single particle. Clearly, such an approach is computationally very demanding. This critically limits the size of the particle bed to be studied. Consequently, the number of parameter variations considered in the work of Oschmann et al. is too small to draw more general conclusions.

In summary, there is still very little quantitative knowledge about the thermal behaviour of particle beds that consist of particles with a non-uniform temperature distribution. This is especially true for beds that are sheared, and for which convective heat transport (i.e., transport due to individual particle motion) might be the dominating transport mechanism. Clearly, a thorough understanding of the relative rates of (i) the transferred heat to the ambient fluid, (ii) the convective heat transport, and (iii) the heat that is transported via conduction is still missing in literature.

When introducing thermal fluxes in the context of the granular flow simulations considered in our present contribution, it is important to consider the exact meaning of their definition. Critically, the term ”convective flux” is fundamentally different from its meaning in classical continuum models: convective fluxes in the context of the present work are caused by random motion of individual particles. This is in contrast to the convective transport of thermal energy due to macroscopic (i.e., particle-average) motion: this ”macroscopic” convective transport can be modeled with relative ease in continuum models [25]. Hence, this mode of thermal transport is not discussed in the present work. Another term is the transferred heat to the ambient fluid: in our present contribution this refers to the heat exchanged between the fluid and individual particles. At

this point we reference the reader to our presentation in Section 3.2.4 which provides a more holistic view of all relevant thermal fluxes. Most important, these fluxes are the main output of our simulations, and can be subsequently used in continuum models to describe thermal transport in granular materials and fluid-particle systems. Unfortunately, rigorous closures for these fluxes are still missing in literature, currently limiting the application of continuum models to engineering problems. In this study, we focus on suspensions characterized by a large Stokes number ($St = 2/9\,\rho_p \mathbf{u} d_p/\mu_f$) which are relevant for a number of practical applications involving gas-particle suspensions (Yin et al. [26]).

It is our goal to improve this situation by coupling DEM-based simulations to a tool that is capable of resolving intra-particle temperature profiles: our tool *ParScale* (see Radl et al. [27], Forgber et al. [28]) allows us to efficiently solve an one-dimensional heat conduction equation within each particle. This enables us to provide answers to questions related to the occurence of situations in which intra-particle temperature profiles are significant. Clearly, this is of utmost importance for the correct selection of an appropriate simulation model for a certain fluid-particle heat transport problem. Specifically, we analyse the relevance of intra-particle temperature gradients by probing an adequate space of dimensionless parameters, most important the Biot and Peclet number. This allows us to identify critical *dimensionless* system parameters for which heat conduction inside the particle becomes limiting. Most important, the use of dimensionless parameters allows us to draw conclusions that are applicable to a wider range of real-world applications compared to previous work. Specifically, our contribution is meant to extend the work of Rognon et al. [17] to (i) a wider range of volume fractions, (ii) to fluid-particle systems with heat transfer to the ambient fluid, and (iii) includes the temperature distribution inside the particles. Same as Mohan et al. [14] we attempt to collapse the predicted conductive flux into one curve. This is done to lay the foundation for the development of an unified continuum model for predicting thermal transport in high-Biot number fluid-particle suspensions.

We note in passing that including heat transfer to the ambient fluid requires the specification of a heat transfer coefficient (details will be discussed in Section 3.2.4), or its dimensionless counterpart the Nusselt Number. Ranz and Marshall [29] developed one of the first Nusselt number correlations for thermal transfer between spheres and ambient fluid. Clearly their correlation is not applicable in dense particle flow which we focus on in the current manuscript. Gunn [30] proposed a still widely-used correlation for the Nusselt number in the porosity range of 0.35-1.0 for various Reynolds numbers. Thus, using Gunn's results it is straight forward to estimate the heat transfer rate, and consequently also the

Biot number, in any given fluid-particle flow systems.

Our paper is structured as follows: in Section 3.2 we describe the simulation method, including the governing equations for the DEM and the intra-particle heat transport model. Furthermore, we provide details about the coupling sequence between *LIGGGTHS* and *ParScale*. Section 3.3 summarizes our theoretical analysis of transport of thermal energy in a sheared particle bed. Subsection 3.3.2 considers effects due to heat conduction with the particles, and subsection 3.3.3 aims on presenting results for limiting cases in order to better interpret our numerical data in Section 3.4. These subsections hence constitute the first part of our results. The second part of our results is placed in Section 3.4 where the sheared particle simulation setup is described in detail, including the effect of all relevant dimensionless numbers. Section 3.5 views our results in light of previous findings, and comments on possible future applications of *ParScale*. A consistent list summarizing the nomenclature used, including all quantities of secondary importance which are not mentioned after their first appearance in the paper, is available in Section 3.6.

3.2 Simulation Method

An overview of all relevant transport equations used in our simulations is provided in Table 3.1. Also, we have summarized the corresponding unknown simulation variables in Table 3.2. Note that some of the equations are discussed in more detail in the next Section. We want to emphasize that we solve the transport equations for the fluid only in Section 3.3.2, while in all other parts of our contribution we consider (i) the fluid to be held at a fixed temperature, and consider (ii) a fixed particle-fluid heat transfer coefficient. Also, as implied by our title, we consider inertial particles, i.e., particle motion is not affected by fluid motion. This is done to avoid the large computational effort needed to resolve local fluid flow and temperature, which would make our study unaffordable considering our current computational resources.

3.2.1 Particle Flow Model

The open-source software package *LIGGGHTS* [31], [14] is a well established Discrete Element Method-based tool and was used in combination with a spring-dashpot model [31] in the present work. Note that we do not solve any transport equations for the fluid, but consider (i) the fluid to be held at a fixed temperature, and consider (ii) a fixed particle-fluid heat transfer coefficient. Specifically, the following contact force models in the tangential (i.e., $\mathbf{f}^{t}_{i,j}$) and normal direction (i.e., $\mathbf{f}^{n}_{i,j}$) were applied:

$$\mathbf{f}^{t}_{i,j} = -k^{t}\,\mathbf{u}^{t}_{ij} - \eta^{t}\mathbf{v}^{t}_{ij} \tag{3.1}$$

$$\mathbf{f}^{n}_{i,j} = k^{n}\,\delta_{ij}\mathbf{n}_{ij} - \eta^{n}\,\mathbf{v}^{n}_{ij} \tag{3.2}$$

with:

$$\delta_{ij} = r_i + r_j - \mid \mathbf{r}'_i - \mathbf{r}'_j \mid . \tag{3.3}$$

Thereby δ_{ij} indicates the normal overlap, which is positive in case of overlapping particles. Below we summarize the most important quantities that are relevant for the interpretation of our work. For the meaning of other symbols we refer to the Nomenclature. The characteristic contact time t_{co} of the above linear

spring-dashpot model is defined as:

$$t_{co} = \pi \,/\, \omega \tag{3.4}$$

with

$$\omega = \sqrt{(k/m_{eff} - \eta^2)\,/\,(4\,m_{eff}^2)}. \tag{3.5}$$

This contact time t_{co} limits the time step $\triangle t$ for the integration of Newtons equation of motion. The coefficient of restitution e_n is defined as

$$e = \exp\left(\frac{-\pi\eta}{m_{eff}\sqrt{(k/m_{eff} - \eta^2)\,/\,(4\,m_{eff}^2)}}\right) \tag{3.6}$$

and was adjusted to 0.9. In our simulations, the spring stiffness and damping coefficient in the normal and tangential direction are set equal. In order to obtain a certain restitution coefficient, and a certain dimensionless shear rate γ^*, we adjust η and k. For more information on the used parameter ranges and routines to calculate, e.g., the effective Young's modulus, we refer the interested reader to Section 3.4 and Appendix 3.7.

3.2.2 Transport within a Particle

In order to calculate intra-particle properties, a tool called *ParScale* (short for *Particle Scale*) [32] was developed. It is capable of resolving individual property profiles (e.g., that of the temperature, or a dissolved chemical species) inside a particle. Specifically, *ParScale* relies on the so-called Method of Lines (MoL) as outlined in the next paragraph. The resulting system of equations is solved by an already established multi-step solver called *CVODE*. This enables *ParScale* to perform flexible and stable simulations, even in case of fast changing environmental conditions, or (numerically) stiff systems that are typical for non-isothermal reactive porous particles.

The next sections outline the governing equations, provide more detailed information on the solution procedure, and give an overview of the parallel coupling strategy.

Governing Equations

In this paper only heat conduction inside non-porous particles is taken into account. Note, the current development state of *ParScale* already allows the treatment of mass transfer, multiple chemical reactions, as well as phase change phenomena (e.g., evaporation) taking place inside porous particles. However, these phenomena are not accounted for in our present study.

The basic approach of the MoL is to (i) discretize the transport equation related to all intra-particle properties in space, and (ii) then integrate the discretized equations in time. At this stage, an one-dimensional spatial discretization in a radial coordinate system centered at the particle position has been employed. Therefore, every particle is spatially split in a fixed number of grid points. At each of these points, the differential heat balance in spherical coordinates is solved (see Eqn. (3.8)). We want to amplify that the thermal boundary condition of the heat transfer equation solved in *ParScale* is a combination of the transferred heat flux to the surrounding q^{trans} and the per-particle heat conduction rate (which is calculated by summing over all particle-particle contact points, similar to what is done in Eqn. (3.9). Since we are only tracking solid, non-porous particles, we can assume for the particles' mean heat conductivity $\lambda_p = const$. After introducing the thermal diffusivity a, the differential heat balances reads:

$$a = \frac{\lambda_p}{\rho\, c_p} \tag{3.7}$$

$$\frac{\partial T}{\partial t} = a \left(\frac{\partial^2 T}{\partial r^2} + \frac{2}{r} \frac{\partial T}{\partial r} \right) \tag{3.8}$$

For discretisation in physical space, a second order central differencing scheme is used. A verification case, i.e., the convective cooling of a sphere, was used to ensure a correct implementation of the discretization schemata, and the integration of *ParScale* with the solver *CVODE*. For details of the differencing scheme, as well as results of the verification studies, the reader is referred to Appendix 3.7 and Section 3.7.

Reference System	Equation
Particle flow	$\frac{d\,\mathbf{x}_i}{d\,t} = \mathbf{v}_i$ $m\,\frac{d\,\mathbf{v}_i}{d\,t} = \sum_j (\mathbf{f}^t_{ij} + \mathbf{f}^n_{ij})$ $I_i\,\frac{d\,\boldsymbol{\omega}_i}{d\,t} = \sum_j \mathbf{f}^t_{ij} \times \mathbf{r}_{ij}$
Fluid Flow	$\boldsymbol{\nabla} \cdot \mathbf{u} = 0$ $\frac{\partial\,\mathbf{u}}{\partial\,t} + \boldsymbol{\nabla} \cdot (\mathbf{u}\mathbf{u}) = -\boldsymbol{\nabla} p + Re^{-1}\nabla^2\mathbf{u}$ $\frac{\partial\,\theta}{\partial\,t} + \boldsymbol{\nabla} \cdot (\mathbf{u}\theta) = Pe^{-1}\nabla^2\theta$
Internal thermal transport	$\frac{\partial T}{\partial t} = a\left(\frac{\partial^2 T}{\partial r^2} + \frac{2}{r}\frac{\partial T}{\partial r}\right)$

Table 3.1: Covering equations for particle flow (Newtons equation of motion), fluid flow (Continuity equation, Navier-Stokes equation, scalar transport for e.g. temperature) and equations regarding internal thermal transport in spherical coordinates in one-dimensional form.

Reference System	Unknown quantities
Particle flow	Particle positions $\mathbf{x}_i$
	Particle velocities $\mathbf{v}_i$
	Angular velocity $\boldsymbol{\omega}_i$
Fluid Flow	Fluid velocities $\mathbf{u}$
	Pressure p
	Scalar quantity θ e.g. temperature
Internal thermal transport	Particle temperature T

Table 3.2: List of unknown simulation quantities.

3.2.3 Code Architecture and Parallel Coupling Strategy

ParScale is developed in a C++ environment, relies on a hierarchical class structure, and is packaged in a library that can be easily integrated with other particle-based simulation tools. Most important, *ParScale* is equipped with well-structured data containers for the easy transfer of particle information during a parallel simulation run. Note, that data containers are separated from an external particle simulator, in order to ensure a maximum level of compatibility with different simulators and parallelization strategies. In summary, *ParScale* is scalable, flexible, and can be adapted to the users needs by the simple addition of user-defined classes. *ParScale* is currently hosted on a public Github repository [32], together with detailed installation instructions and a comprehensive user documentation. *ParScale* has two different run modes: (i) a stand-alone mode, and (ii) a coupling mode in which *ParScale* acts as a slave to an external DEM or CFD-DEM simulator. At the current development state *ParScale* features coupling to *LIGGGHTS*, as well as *CFDEMcoupling*. Example cases placed in the public repository demonstrate the usage of *ParScale*, contain several verification cases to prove the correct implementation, and provide some post-processing and plotting routines. Since *ParScale* is combined with the open-source solver *LIGGGHTS* in the current work, an overview of a single time step of a coupled *LIGGGHTS-ParScale* simulation is shown in Fig. 3.1. At the beginning of every time step *LIGGGHTS* is running as the master program. It solves for the particle movement (i.e., all DEM-based calculations) and hands over surface temperatures, actual heat transfer coefficients, and fluxes due to an eventual conductive heat transfer between contacting particles. Some other coupling options are available, e.g., setting a specific environment temperature for each particle, which is used in the present contribution. Furthermore, it is possible to reset the whole particle temperature to a constant value. After all calculations of *LIGGGHTS* are completed, *ParScale* initializes from the last know time step and reacts to changes due to the coupling of the particle motion solver. Specifically, it updates the surface temperature, calculates source terms (e.g., due to reactions or phase change phenomena), and pushes these particle properties back to *LIGGGHTS* for the next time step. For visualisation and post-processing purposes, additional information (e.g., core, or the volume-averaged temperature, as well as conductive, or convective heat fluxes) can be exchanged with *LIGGGHTS*.

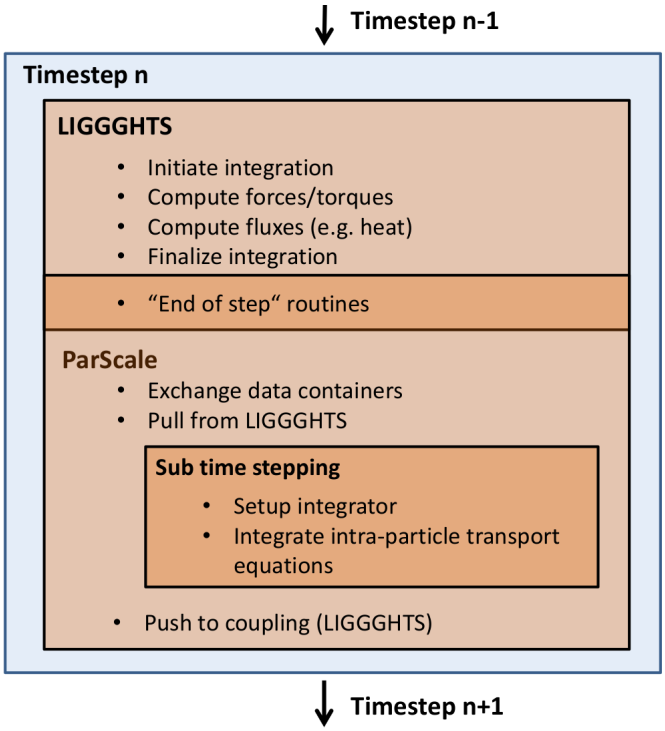

Figure 3.1: Coupling between *LIGGGHTS* and *ParScale* for one time step including required coupling parameters and additional coupling options.

3.2.4 Thermal Fluxes

The definition of thermal fluxes is taken from the work of Mohan et al. [14] and a simplified example assemble including a description of coordinates can be found in Fig. 3.7. Physically seen, the convective flux (Eqn. (3.9)) is defined as the redistribution of thermal energy of the particles due to its macroscopic movement inside the simulation domain. In the contrary, the conductive thermal flux (Eqn. (3.10)) accounts for the heat exchanged between two particles in case of a collision. Drawing back to classical thermodynamics, the transferred heat flux (Eqn. (3.11)) describes the exchange of thermal energy between fluid and particle. This transferred amount of heat is mainly a function of the heat transfer coefficient α and the temperature difference between particle and ambient fluid. Note that $\mathbf{q}^{cond}$ is defined for particles with equal physical properties regarding thermal conductivity and is calculated for the sum of all contacts in the domain with the volume V.

$$\mathbf{q}^{conv} = \frac{1}{V} \sum_{i} m_{eff,i}\, c_{p,i}\, T_{vol,avg,i}\, \mathbf{v}_i \tag{3.9}$$

$$\mathbf{q}^{cond} = \frac{1}{V} \sum_{co} 2\, \lambda_p\, A_{co}^{1/2}\, (T_i - T_j)\, \mathbf{r}_{ij} \tag{3.10}$$

$$q_i^{trans} = \alpha\, (T_i - T_{f,i}) \tag{3.11}$$

The conditional claim of a fully periodic, sheared bed with Lees-Edwards boundary conditions is that the domain-averaged particle velocity equals zero. When considering the sheared particle ensemble used in our work (see Section 3.4), it is important to note that we consider three different "thermal" regions as shown in Fig. 3.7 in Section 3.4. Most important, we only consider the center region (i.e., region B in Fig. 3.7) to calculate the fluxes. In such a case one has to correct the calculation of the convective flux as discussed in the next paragraph. Even though the above conditional claim related to the domain-averaged particle velocity is fulfilled for the full box, this does not apply for our center region in which the thermal calculations are performed. Since we fix the temperature of the particles located inside the top and bottom region to enforce a predefined temperature gradient, the number of particles in these regions fluctuates over time. Also, dividing the domain into three regions causes a temporal fluctuation of the number (as well as the average speed) of the particles in each region. Thus, we see a drift convective flux due to the average macroscopic movement of the

particles in the center region, which is characterized by the velocity $v^{y,drift}$:

$$q^{y,conv} = \frac{1}{V} \sum_i m_{eff,i}\, c_{p,i}\, T_{vol,avg,i}\, (v_i^y + v_{drift,i}^y) \tag{3.12}$$

or explicitly calculated

$$q^{y,drift} = \frac{1}{V} v_{drift}^y \sum_i m_{eff}\, c_p\, T_{vol,avg,i}. \tag{3.13}$$

As mentioned above, the number of particles in our center region is not fixed and can change due to the deformation of the box. Consequently, we need to weight our already corrected convective flux with the number of particles in the region when computing a time-average flux:

$$\mathbf{q}^{conv} = \frac{\mathbf{q}^{conv,i}\, n_{p,i}}{1/i \sum_i n_{p,i}}. \tag{3.14}$$

For the reference flux we choose the conductive flux in case our computational domain is completely filled with solid material. Thus, the reference heat flux is calculated as:

$$q_s = -\lambda_p \frac{\partial T}{\partial y} \tag{3.15}$$

where $\partial T/\partial y$ is the temperature gradient in the gradient direction of the shear flow.

3.3 Theoretical Analysis

3.3.1 Dimensional Analysis

The key dimensionless flow parameters, i.e., the coefficient of restitution, the friction coefficient, the dimensionless stresses, the particle volume fraction, and the dimensionless shear rate have been well documented by Chialvo et al. [12], and Mohan et al. [14]. In agreement with Chialvo et al. [12] we define a scaled shear rate as

$$\dot{\gamma} = \gamma \, d_p^{3/2} / \sqrt{k_n / \rho_p}. \tag{3.16}$$

According to the experiments by Nordstrom et al. [33], and recent simulations (Hatano et al. [34], Otsuki et al. [35], Alonso-Marroquín et al. [11]), simple expressions that correlate the above defined dimensionless quantities can be found. Specifically, the scaled stress-shear rate data can be collapsed into curves by appropriately adjusting the critical volume fraction (ϕ_c), as well as a set of exponents as shown below. This scaling will be an inspiration for the re-scaling of the conductive heat flux in the present contribution (see Section 3.4). Thus, of key relevance are the three resulting stress regimes (here illustrated by the pressure), which are characterized by the following expressions:

$$p_{inert} \sim |\phi - \phi_c|^{-2} \tag{3.17}$$

$$p_{QS} \sim |\phi - \phi_c|^{2/3} \tag{3.18}$$

$$p_{int} \sim |\phi - \phi_c|^{0}. \tag{3.19}$$

Previous work only considered the conductive and convective heat transport rate in a sheared, but uncooled, particle bed (see, e.g., Rognon et al. [18]). As pointed out by Mohan et al. [14], the Peclet number is the most influential parameter for heat transport in granular materials and reads:

$$Pe = \frac{(d_p/2)^2}{\lambda_p / (\rho_c \, c_p)} \, \gamma. \tag{3.20}$$

Clearly, Pe characterizes the relative rates of convective and conductive heat transport within the particles in the *absence* of heat transfer to the ambient fluid. In the present work, however, we consider exactly this heat transfer rate to the ambient fluid, which is characterized by the heat transfer coefficient α. Therefore, we must introduce a new dimensionless quantity, which we choose

to be the Biot number defined as:

$$Bi = \frac{\alpha\, d_p}{\lambda_p}. \tag{3.21}$$

The Biot number can be interpreted as the ratio of (i) the intra-particle and (ii) the external resistance to heat transport. Thus, for high Biot numbers we expect intra-particle temperature profiles to be significant. We will see that also the Peclet number affects intra-particle temperature profiles, since conductive transport between particles (caused by particle-particle collisions) leads to a heat up of the outer shell of the particles.

As an alternative to the Peclet number, one could define a dimensionless convective heat transport rate by using the transferred heat flux (to the ambient fluid) as the reference, i.e.,

$$\Pi = \frac{Pe}{Bi} = \frac{\rho_p\, c_p\, d_p\, \gamma}{\alpha}. \tag{3.22}$$

Π can be interpreted as a scaled length over which convective transport is able to balance the cooling (or heating) caused by the ambient fluid. This dimensionless number is useful in situations in which one wants to probe the effect of the the particles' heat conductivity on the results: for fixed values of Π one can illustrate the effect of heat conduction within the particles by varying the Biot number. Note, that for fixed Pe a variation of Bi does not lead to such a transparent illustration, since also Pe is a function of the particles' heat conductivity, and both dimensionless numbers are zero in the limit of infinitely fast heat conduction within the particles. Since Π is proportional to Pe and Bi, it is straight forward to interpret our results also in light of this new dimensionless quantity. We have already attempted this in most parts of the present contribution.

3.3.2 Effect of Heat Conduction within the Particle

The goal of this Section is to theoretically investigate the cooling of a sphere under different conditions, and justify the assumption of spherical symmetry made in the current work. As pointed out by Schmidt et al. [36], as well as Oschmann et al. [24], the computational cost for a fully resolved particle is enormous: calculation time and data storage increase by a factor of about $1,000$ when using three-dimensionally resolved simulations. Fortunately, an one-dimensional discretization (as followed in the current work) is often an

excellent approximation (in case of a sphere) when considering heat exchange in a certain Reynolds number range (see Nikrityuk et al. [37]). To support this finding, we study the transient cooling of a sphere, and consider different Reynolds numbers. We then compare the temperature change over the radius with the data provided by Nikrityuk et al. [37]. The latter performed a fully three-dimensional simulation, including a resolved flow and temperature profile simulation in the fluid surrounding the particle. For the simulation details we refer to Nikrityuk et al. [37]. We have summarized the key dimensionless parameters in the caption of Fig. 3.2.

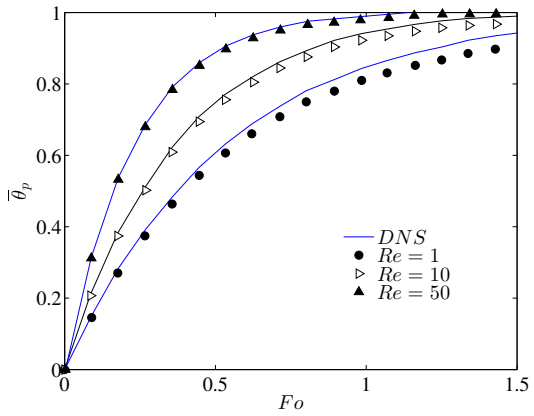

Figure 3.2: Comparison of the volume-averaged temperature profiles derived from the DNS data of Nikrityuk et al. [37], and a 1-D simulation performed with *ParScale* for $Re = 1, Bi \approx 0.365$; $Re = 10, Bi \approx 0.532$; $Re = 50, Bi \approx 1.065$, $\lambda_p / \lambda_f = 7$.

In general, an excellent agreement between the DNS data and simulations performed with *ParScale* over a wide range of dimensionless times, i.e., Fo numbers, can be observed. This is especially true for large Re numbers, where only marginal differences between DNS data and predictions by *ParScale* are observed. As already pointed out by Nikrityuk et al. [37], the maximum difference between a fully three-dimensional simulation and an one-dimensional simulation is between 2% and and $\approx$ 5%. To support this finding, we investigated conjugate heat transfer associated with the flow around a single sphere under significant internal heat transport limitation (see Fig. 3.3 for details). We listed all boundary conditions in Table 3.3 and governing equations in Table 3.1. As can be seen, the temperature profiles inside the particles approach spherical symmetry for higher Reynolds numbers. The reason for this behaviour is that the the temperature distribution in the ambient fluid becomes more uniform, since the rate of convective heat transport in the fluid increases with increasing Reynolds number. At low Reynolds numbers (see panel (a) of Fig. 3.3) a certain

temperature gradient in the fluid in the main flow direction is observed. This temperature gradient leads to a shift of the maximum intra-particle temperature towards the rear stagnation point, causing a significant temperature gradient in the azimuthal direction. Fortunately, most industrial applications are concerned with improving external transport limitations, and hence operate at Reynolds numbers larger than unity. Also, a closer inspection of the global temperature difference in the left panel of Fig. 3.3 indicates a temperature fluctuation of about 0.17 dimensionless units. This is because $Bi < 1$, i.e., the external heat exchange rate is typically much smaller than the heat conduction rate in the particle in case of low Reynolds number flows. In summary, the results in Fig. 3.2 and Fig. 3.3 support our assumption of a spherically-symmetric temperature profile within particles for most gas-particle systems. Of course, this statement only holds for flows involving single spherical particles, and cannot be easily generalized to non-spherical particles, or dense particle ensembles. Thus, we currently cannot provide a rigorous justification for spherical symmetry in dense granular flows where particle-particle heat conduction occurs. Fortunately, this mode of thermal transport (i.e., heat conduction through the contact areas) is typically small: an analysis of the amount of heat exchanged due to conduction (denoted as $\mathbf{Q}^{cond}$) and transfer to the surrounding fluid (i.e., Q^{trans}) on a per particle basis helps to support this argument. Specifically, one finds that the ratio of these heat exchange rates is (based on the expressions for the heat fluxes introduced in Eqn. (3.10) and (3.11):

$$\frac{\mathbf{Q}^{cond}}{Q^{trans}} = \frac{1}{Bi}\,\frac{2\epsilon}{\pi}\,\frac{\langle \triangle T_{co} \rangle}{T_i - T_{f,i}}. \tag{3.23}$$

Here we have introduced ϵ as a parameter that characterizes a typical overlap area, which is typically much smaller than unity. Also, we have denoted with $\langle \triangle T_{co} \rangle$ a mean temperature difference of the contacting particles. If we now accept that the term $\langle \triangle T_{co} \rangle / T_i - T_{f,i}$ is of order unity, we find

$$\frac{\mathbf{Q}^{cond}}{Q^{trans}} = \frac{\epsilon}{Bi}. \tag{3.24}$$

Thus, the relative importance of the conductive heat flux decreases with increasing Biot number. It is now obvious that the heat exchange rate due to particle-particle contacts will not impact the shape of intra-particle temperature profiles, since the latter are significant only for $Bi > 1$. Thus, one can readily transfer the findings related to intra-particle temperature profiles in a single particle to a cooled bed of particles in case one considers Biot numbers of order unity or larger.

Table 3.3: Boundary conditions used for the cooled sphere simulations.

Field/Patch	Quantity	Type/Value
Inlet	Velocity	Fixed value, to realize Re
	Pressure	Zero gradient
	Temperature	Fixed value $\theta = 0$
Outlet	Velocity	Zero gradient
	Pressure	Fixed value, o
	Temperature	Zero gradient
Lateral walls	Velocity	Slip
	Pressure	Zero gradient
	Temperature	Zero gradient
Sphere Surface	Velocity	No slip
	Pressure	Zero gradient
	Temperature	identical flux fluid and particle domain

3.3.3 Analytical Solution for Heat Conduction in a Cooled Particle Bed

In the following we present an analytical approach to calculate the temperature distribution in a sheared bed with a constant ambient fluid temperature T_f, and study the limiting cases with respect to the Biot number. To the best of our knowledge no analytical solution for the mean temperature profile in a cooled bed of moving particles exists. To approach this issue, we first calculate the mean particle temperature distribution inside a static bed of cooled particles. Therefore, we use the particle heat conductivity λ_p, as well as simple geometrical factors that describe the morphology of the particle bed. Specifically, we assume that the bed has an average effective cross-sectional area A, and an average effective cross-sectional perimeter U (see Fig. 3.4 that also illustrates their local counterparts). We note that the calculation of the effective area and perimeter cannot be done by taking a simple arithmetic mean of their local counterparts. This is due the fact that in the governing equation for heat conduction in the fin (discussed in the next paragraph) the cross-sectional area A comes into play in a non-linear fashion. Consequently, A will be also impacted by the average particle-particle contact area, which depends on ϕ_p, and hence the applied stress. Fortunately, in what follows it is not necessary to provide an expression for the

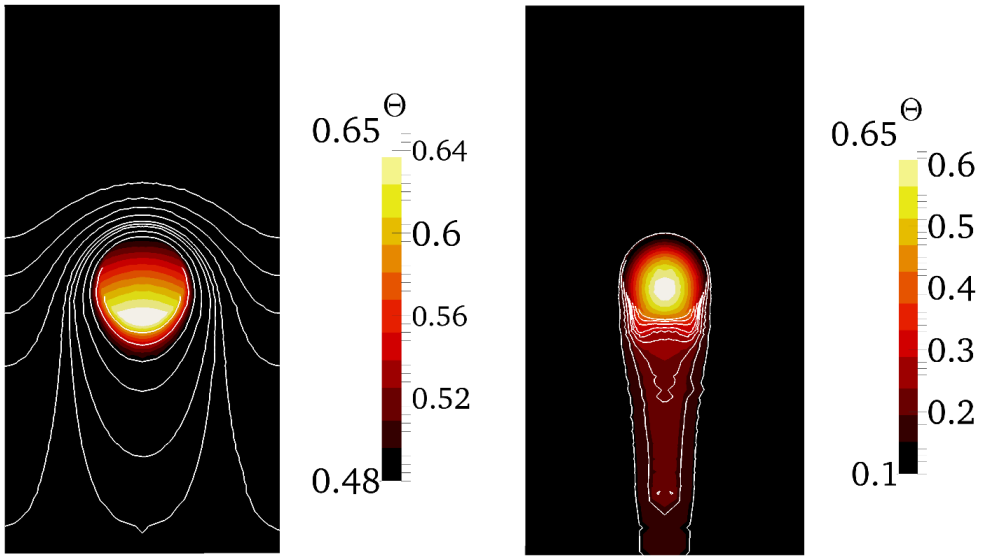

(a) (b)

Figure 3.3: Temperature distribution in the fluid and in the particle when cooling a single sphere initially having the temperature $\theta_{init} = 1$, at $Pr = 4.3$ and $\lambda_p/\lambda_f = 1.37$ - internal limitation problem; flow vertically downwards; white lines are temperature iso-contours in the fluid; (a) $Re_p = 1$, $Fo = 2.6$, $Bi \approx 0.15$; (b) $Re_p = 100$, $Fo = 0.17$, $Bi \approx 7.65$.

effective cross-sectional area and perimeter. We will see that considering these effective quantities is sufficient to explain the qualitative features of the mean particle temperature distribution.

In case we accept the above simplification, we can reduce the problem of heat conduction inside a static bed to the problem of heat transport in and around a convectively-cooled fin (see Fig. 3.4, left panel). The steady-state solution of this classical heat transport problem is straightforward, and relies on the following differential heat balance:

$$\lambda_p \frac{\mathrm{d}^2 T}{\mathrm{d}y^2} \quad - \frac{\alpha\, U}{A}(T - T_f) = 0. \tag{3.25}$$

Note that the above expression only considers thermal transport through the particles, and hence avoids complexities arising due to, e.g., heat conduction via the ambient fluid as mentioned in Kuipers et al. [25]. We feel that such complexities should be incorporated by a separate model for thermal transport in the surrounding fluid, and hence can be added in the future.

Normalization of the above heat balance equation by introducing

$$y^* = \frac{y}{d_p} \tag{3.26}$$
$$\theta = T - T_f \tag{3.27}$$
$$\mathrm{d}\theta = \mathrm{d}T \tag{3.28}$$
$$\mathrm{d}^2\theta = \mathrm{d}^2T \tag{3.29}$$

leads to

$$\frac{\mathrm{d}^2\theta}{\mathrm{d}y^{*2}} = \underbrace{\frac{d_p\,\alpha}{\lambda_p}}_{Bi}\ \underbrace{\frac{d_p\,U}{A}}_{g^*(Pe,\phi_p,\dot{\gamma})}\ \theta. \tag{3.30}$$

The first term on the right hand side of the above equation is equal to the Biot number. The second term, i.e., (g^*), represents a dimensionless metric for the bed morphology. The latter fluctuates in case the bed of particles is sheared (see our discussion below). However, it is reasonable to assume that this is irrelevant for the steady-state solution to a first approximation.

We next consider thermal transport in a sheared bed. Clearly, the rate of heat transport through the bed will be increased due to the motion of particles in such a case. This will not change the structure of the above differential equation as long as we assume that particle motion in the gradient direction leads to a diffusive transport of thermal energy. In other words, we assume that the additional heat flux caused by particle motion linearly scales with the temperature gradient. Consequently, only the magnitude of the heat conductivity will change, and one could simply introduce an effective heat conductivity of the sheared particle bed, i.e., λ_{eff} in Eqn. (3.30). This effective heat conductivity will be some function of ϕ_p, $\dot{\gamma}$ and the particle parameters. Naturally, one would express λ_{eff}/λ_p as some function of the Peclet number, the particle concentration and the dimensionless shear rate. Hence, one can easily split off the particles' heat conductivity from λ_{eff} and remain the general structure of Eqn. (3.30). Thus, we simply lump the effect of particle flow, i.e., the convective heat transport due to random particle motion, and the consequent change of A into the (unknown) function $g^*(Pe, \phi_p, \dot{\gamma})$. Clearly, g^* will decrease with increasing shear rate and increasing Peclet number (i.e., softer particles moving faster), since the effective heat conductivity and the area available for conduction will increase with increasing speed of shearing (or increasing particle softness). While g^* lumps a large number of phyical effects, we have not attempted to decouple these effects in the present contribution. This is done since such a

decoupling is not essential to understand the qualitative features of the particle temperature profiles discussed in the next paragraphs. Also, we note in passing that in the following, we have set T_f to be constant as indicated in Fig. 3.4.

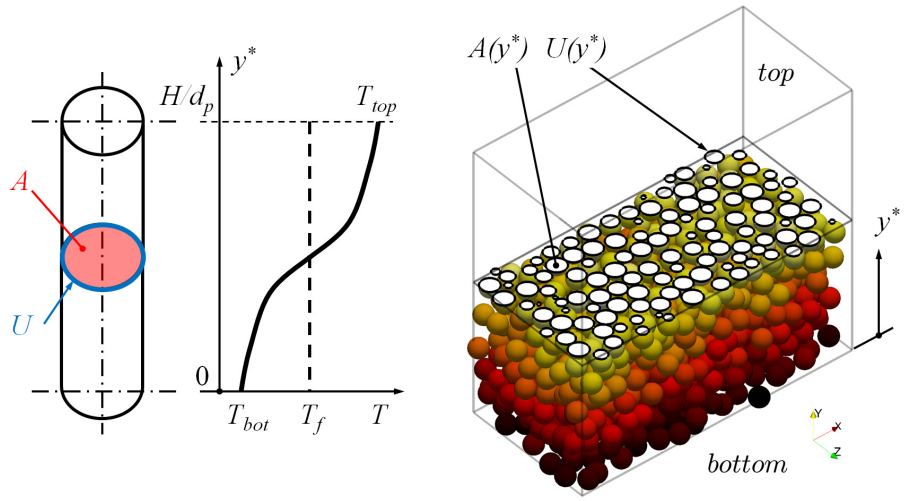

Figure 3.4: Schematic illustration of the cooled fin approach (left panel) for computing the mean particle temperature based on an effective cross-sectional area A and perimeter U. Similar to the sheared box setup we assume $T_f = (T_{top} + T_{bot})/2$. The right panel illustrates the corresponding local perimeter $U(y^*)$ and the local cross sectional area $A(y^*)$.

We now use the following Ansatz for the solution of the temperature profile:

$$\theta = c_1 e^{(Bi\, g^*) y^*} + c_2 e^{-(Bi\, g^*) y^*} \tag{3.31}$$

with the boundary conditions

$$(1) \quad \text{for } y^* = 0 : \theta = \theta_0 = T_{bot} - T_f \tag{3.32}$$

$$(2) \quad \text{for } y^* = H/d_p = H^* : \theta = \theta_H = T_{top} - T_f. \tag{3.33}$$

This leads us to the following constants:

$$c_1 = \theta_0 - \frac{\theta_0\, e^{(Bi\, g^*) H^*} - \theta_H}{e^{(Bi\, g^*) H^*} - e^{-(Bi\, g^*) H^*}} \tag{3.34}$$

$$c_2 = \frac{\theta_0\, e^{(Bi\, g^*) H^*} - \theta_H}{e^{(Bi\, g^*) H^*} - e^{-(Bi\, g^*) H^*}}. \tag{3.35}$$

Combining these constants with Eqn. (3.31) one obtains the following mean

particle temperature distribution:

$$\theta = \left(\theta_0 - \frac{\theta_0\, e^{(Bi\, g^*)H^*} - \theta_H}{e^{(Bi\, g^*)H^*} - e^{-(Bi\, g^*)H^*}}\right) e^{(Bi\, g^*)y^*} + \left(\frac{\theta_0\, e^{(Bi\, g^*)H^*} - \theta_H}{e^{(Bi\, g^*)H^*} - e^{-(Bi\, g^*)H^*}}\right) \mathrm{e}^{-(Bi\, g^*)y^*}. \tag{3.36}$$

This equation does not allow us to explicitly calculate the effect of the shear rate on the resulting temperature profile. However, it provides us with an analytical solution to study certain limiting cases, namely sheared beds under the influence of high and low thermal heat exchange rates to the ambient fluid. Also, this analytical solution allows us to draw qualitative conclusions on the effect of the particle shear rate as mentioned above: faster shearing (i.e., increasing Π or Pe) will lead to a more uniform temperature profile, since convective heat transport (due to random particle motion) becomes the dominating mode of thermal transport compared to heat transfer to the ambient fluid.

We note in passing that after calculating the temperature gradient from the above temperature profile, as well as integrating over the bed height, the mean heat flux based on the above analytical solution bed can be calculated as:

$$\begin{aligned} \frac{\partial\theta}{\partial y^*} = \theta' &= \left(\theta_0 - \frac{\theta_0\, e^{(Bi\, g^*)H^*} - \theta_H}{e^{(Bi\, g^*)H^*} - e^{-(Bi\, g^*)H^*}}\right) (Bi\, g^*)\, e^{(Bi\, g^*)y^*} \\ &\quad - \left(\frac{\theta_0\, e^{(Bi\, g^*)H^*} - \theta_H}{e^{(Bi\, g^*)H^*} - e^{-(Bi\, g^*)H^*}}\right) (Bi\, g^*)\, e^{-(Bi\, g^*)y^*} \qquad (3.37) \\ \overline{q^{y,analyt}}^* &= \frac{\lambda_{eff}}{\lambda_p}. \qquad (3.38) \end{aligned}$$

This heat flux has been normalized with the reference flux (i.e., q_s), and requires the knowledge of λ_{eff}/λ_p or, alternatively, g^*. Unfortunately, the latter quantities are unknown, and hence must be modelled (e.g., via models for the conductive and convective fluxes developed in the present contribution). In the following we study certain limiting cases, and only compare the qualitative features of the temperature profiles inside the sheared bed between the simulation and the above analytical solution. Note, that g^* has been adjusted in the following such that the difference between analytical solution and simulation data is a minimum. Thus, the following comparison is only helpful to judge whether the shape of the temperature profiles can be predicted. Models for the

effective heat flux (due to conduction and convection) are proposed in Section 3.4, which can be used to compute the effective heat conductivity in a straight forward manner.

Small Biot Number Limit

The first limiting case we study is a sheared bed without any heat transfer to the ambient fluid. This is in line with the work of Rognon et al. [17] and Mohan et al. [14]. Therefore, it is clear that for a steady-state situation the temperature profile is linear, as seen in Fig. 3.5. A very good agreement can be observed from

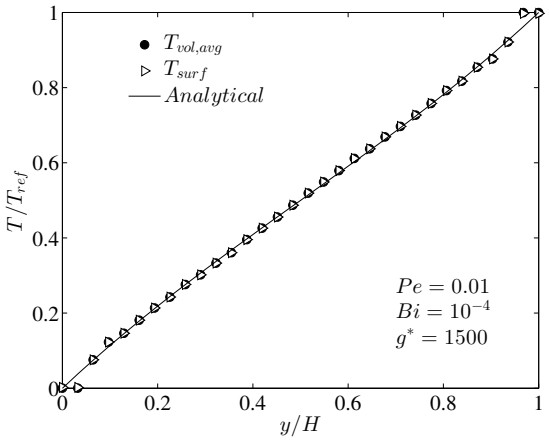

Figure 3.5: Temperature profile for $\dot{\gamma} = 10^{-3}, \phi_p = 0.64$. (a) $Pe = 0.01$, $Bi = 10^{-4}$, $g^* = 1500$, $T_f = (T_{top} + T_{bot})/2$.

the above figure. Volume-averaged and surface temperature are collapsing in one point since the Biot number is small (and in the limit of thermally insulated particles, i.e., no heat exchange with the ambient fluid, $Bi = 0$). Due to the low Biot number the solution is independent of the fluid temperature, the dimensionless shear rate and the volume fraction. Unfortunately, this solution does not lead to a deeper understanding of the total fluxes inside the bed and the relative contributions of convective and conductive transport rates. Thus, in the following we study a set of dimensionless parameters for which the temperature distribution is mainly governed by the heat transferred to the ambient fluid, and hence might help us to better understand the associated heat fluxes.

High Biot Number Limit

The second limiting case is a sheared bed which is strongly cooled by the ambient fluid, i.e., heat transfer to the ambient fluid is fast. It is obvious that in this limiting case the temperature of the ambient fluid is of key importance. Also, we expect that for Π approaching zero (at finite Bi) the convective and conductive flux will vanish, since the particle temperature approaches the fluid temperature. To illustrate this, we study high Biot number flows to highlight the mean particle temperature profiles in a sheared particle bed. For the shown set of

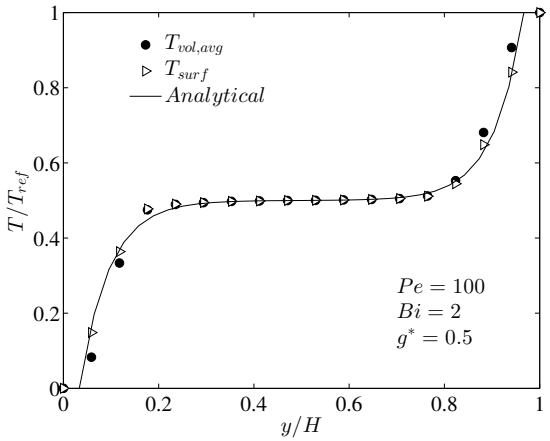

Figure 3.6: Temperature profile for $\dot{\gamma} = 10^{-3}, \phi_p = 0.64$. (a) $Pe = 100$, $Bi = 2$, $g^* = 0.5$, $T_f = (T_{top} + T_{bot})/2$.

dimensionless parameters a clear difference to Fig. 3.5 can be observed. The heat transfer to the ambient fluid leads to a fast relaxation of the bed temperature to the fluid temperature. Also, for even higher Biot numbers we observe a steeper gradient near the top and bottom of the bed (data not shown). This is explained by the corresponding decrease of $\Pi = Pe/Bi$, i.e., the dimensionless distance over which convective heat transport outbalances heat transfer to the ambient fluid decreases. In contrast, this gradient decreases with increasing Peclet number: fast shearing in combination with a low thermal conductivity of the particles smoothens out temperature gradients.

Another key observation is that in case of low Π-number flows, the temperature gradient (and hence the thermal fluxes through the particle bed) is no longer constant over the simulation domain. Consequently, the size of the considered domain may affect the predicted mean thermal fluxes in that domain. Hence, in what follows it is essential to consider the size of the simulation domain for a correct interpretation of the results. Specifically, we now explore a wider range

of dimensionless parameters to establish a more quantitative understanding of thermal fluxes through sheared particle beds.

3.4 Simple Shear Flow

We now investigate the thermal behaviour of a sheared particle bed under different flow and thermal conditions. By applying Lees-Edwards boundary condition to a fully periodic box driven by a homogeneous shear flow, a combination of *LIGGGHTS* and *ParScale* can be used to study various influence parameters. The dimensions of the box are chosen to be $H/d_p = 15$ with a wide range of particle volume fractions (ϕ_p = 0.30-0.64) studied. The z-direction serves as the spanwise direction, whereas in x-direction the homogeneous shear flow is driven. In y-direction we apply a temperature gradient by fixing the temperatures in the top and bottom layer. Fig. 3.7 summarizes this setup in the $y - x$ plane, in which region A and C are the hot and cold region, respectively. In region B the temperature of the particles is allowed to evolve freely. Consequently we do not take the top and bottom layer into account during our post processing procedures, and just analyse thermal transport in the center region, i.e., region B. In order to study the transferred heat to the ambient fluid (note that Mohan et al. [14], Rognon et al. [17] considered particles in vacuum, i.e., perfectly insulated), the fluid temperature is set equal to the average of the top and bottom temperature. Note, that the number of particles, as well as their mean velocity is not constant in the center region, a fact that needs to be accounted for in the analysis. Wide ranges of various parameters and their influence on the thermal fluxes (corresponding to Mohan et al. [14], Rognon et al. [17]) are studied in what follows. An overview of these ranges is given in Tab. (3.4).

These parameter ranges in Tab. (3.4) are chosen according to realistic scenarios involving solids particles in a gas. Relevant industrial applications for the high Biot number are, for example, 'thermally thick' biomass particles (Mehrabian et al. [38]). The volume fraction covers more dilute flows ($\phi_p = 0.3$), but also includes the densest packing possible under the assumption of mono-disperse spheres ($\phi_p = 0.64$). Dimensionless shear rate and Peclet number relate to Rognon et al. [17] and account for soft and hard spheres and particle movement that can typically be found in earthquakes, landslides and general granular lubrication, respectively. Biot numbers up to $Bi = 25$ are typical for granular flows involving highly porous particles with low heat conductivity (e.g., wood,

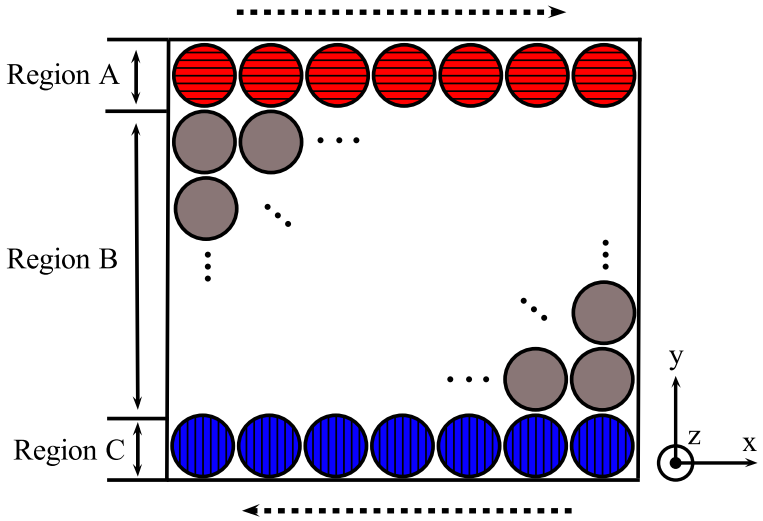

Figure 3.7: Sheared bed assemblies considering three thermal regions A, B and C. The main flow direction is x as indicated by the dashed arrows, y denotes the gradient direction, and z indicates the spanwise direction.

Table 3.4: Dimensionless input parameters for the sheared box simulations.

Parameter	Min. Value	Max. Value
ϕ_p	0.3	0.64
$\dot{\gamma}$	10^{-4}	10^{-1}
Pe	10^{-2}	10^{2}
Bi	10^{-5}	25
μ	0.1	fixed
e	0.9	fixed
T_f	$(T_{top} + T_{bot})\,/\,2$	fixed

or polymeric materials), a typical size of $d_p \sim 5 - 10$ mm, and a Reynolds number of $Re = 100$ or higher.

In our simulations all particles are initialized with an uniform temperature, are forced to the temperatures in the top and bottom layer, and are sheared according to a predefined set of dimensionless parameters. After a certain shear deformation, the flow has converged into a statistical quasi-steady state, in which convective and conductive fluxes through the bed (i.e., region B) can be averaged and compared. Fig. 3.8 shows typical results at such a state. In order to visualize the variety of flow situations, Fig. 3.8 summarizes results for certain limiting cases. Specifically, Fig. 3.8 (a) shows the lowest Peclet and Biot

number studied (compare Table 3.4). Fig. 3.8 (b) shows results for a flow that is dominated by the transferred flux to the ambient fluid, whereas Fig. 3.8 (c) and (d) show results for the highest Peclet number studied and the extrema in the Biot number. As can be seen, a non-trivial distribution of particle temperatures develops in the simulation domain, depending on the combination of Peclet and Biot number. Interestingly, intra-particle temperature gradients appear for the situations characterized by a high Peclet number (see Fig. 3.8 c and d). As expected, these gradients are most significant for the combination of a high Pe and Bi. We next study the influence of the particle stiffness (i.e., the

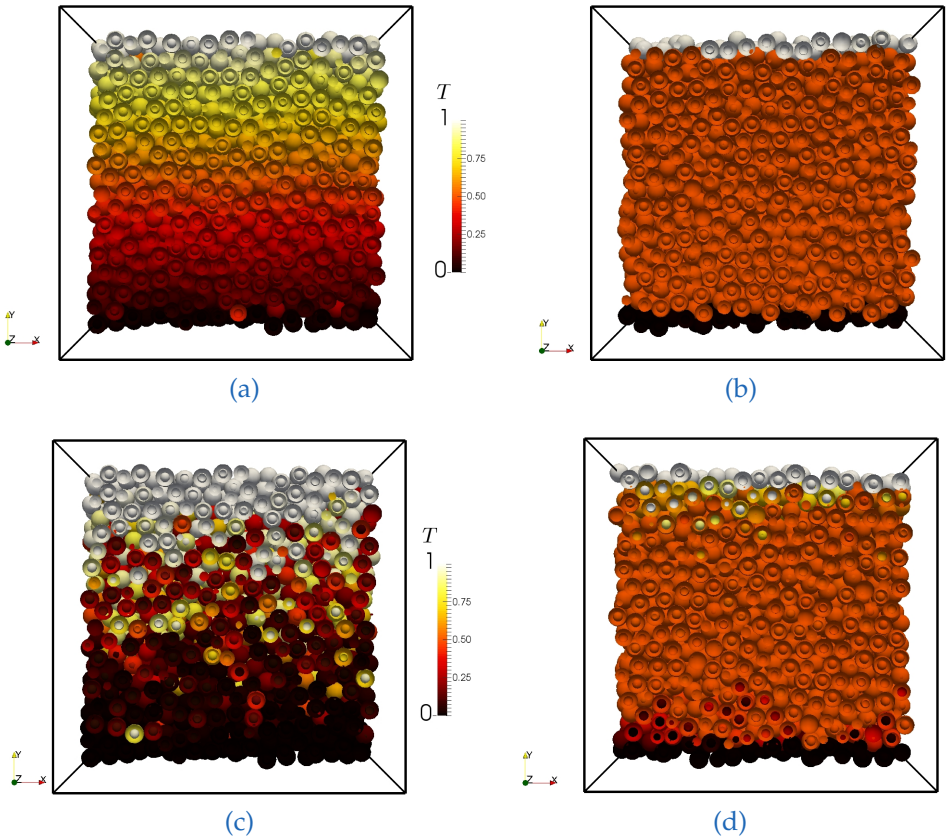

Figure 3.8: Typical result before the statistical steady state for $\phi_p = 0.64$, $\dot{\gamma} = 10^{-3}$, (a) $Pe = 0.01$, $Bi = 10^{-5}$,(b) $Pe = 0.01$, $Bi = 25$, (c) $Pe = 100$, $Bi = 10^{-5}$, (d) $Pe = 100$, $Bi = 25$.

dimensionless shear rate) on conductive fluxes in the sheared bed over a wide range of Biot and Pelcet numbers. This analysis is motivated by the regimes observed for the evolution of the stresses in granular materials.

3.4.1 Effect of Particle Stiffness on Conductive Fluxes

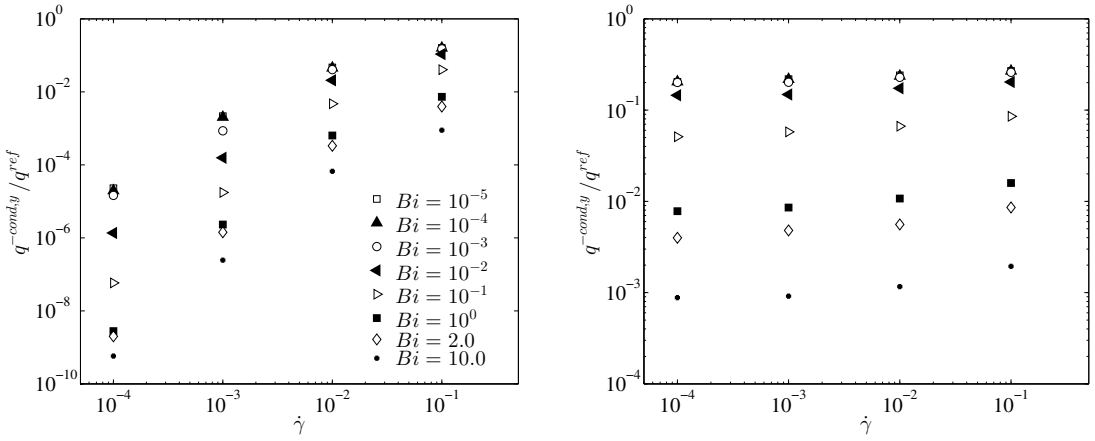

Figure 3.9: Influence of the particle stiffness ($\dot{\gamma} = 10^{-4}, 10^{-3}, 10^{-2}, 10^{-1}$) for different particle volume fractions over a variety of Biot numbers, and at $Pe = 0.01$. (a) ϕ_p = 0.58, (b) ϕ_p = 0.64.

Due to the large difference of the conductive flux depending on the particle concentration, Fig. 3.9 only depicts the influence of the particle stiffness for high particle loadings. Namely we study (a) ϕ_p = 0.58 and (b) ϕ_p = 0.64 for a Peclet number of 0.01. Thereby, higher dimensionless shear rates $\dot{\gamma}$ indicate softer particles (compare Eqn. (3.16)). Note, for lower particle concentrations the conductive flux dramatically decreases, and hence is of no significance for the practical application.

As seen on the left side of the figure, the dimensionless conductive heat flux drops to 10^{-5} (low Biot limit) and 10^{-9} (high Biot limit) for situations involving very stiff particles, i.e., at $\dot{\gamma} = 10^{-4}$. With increasing dimensionless shear rate the dimensionless conductive heat flux increases with a constant slope of two in double logarithmic space. This is observed over a wide range of Biot numbers. Thus, the transferred heat to the environment has no influence on this scaling law. Only at the highest studied shear rate this is not true any more, since the flow approaches an intermediate regime of heat conduction, similar to the one observed for stresses in sheared granular matter. This trend can also be observed for smaller particle volume fractions (data not shown), with the only difference that conductive fluxes are generally much smaller in such a flow.

In the intermediate regime the contribution of the conductive heat flux reaches a noticeable value. Most important, this is also the case for intermediate Biot

numbers which are relevant for some industrial applications (i.e., $Bi \approx 1$). In contrast, the contribution for higher Biot numbers remains in the negligible range (e.g., for $Bi = 10$, the conductive flux is only $1/1000$ of the reference flux). Investigating a higher particle volume fraction (i.e., $\phi_p = 0.64$, see Fig. 3.9 panel (b)), the dimensionless conductive heat flux is not affected by the dimensionless shear rate anymore, and can be assumed to be constant for every shear rate. The results for the higher volume fraction and the dimensionless value are in agreement with Rognon et al. [17], even though their study was limited to one volume fraction. In our present work the flow reached the quasi-static regime where the ratio of contact forces and stiffness, which can be interpreted as a mean particle-particle overlap, does not change when changing the particles' stiffness. Thus, the widely accepted fact [12] that for dense quasi-static granular (i) the dimensional contact stress scales linearly with the particles' stiffness, and (ii) that the normalized stress is independent of the (dimensionless) shear rate in fixed volume simulations is of crucial importance: since contact stress and contact force are directly proportional, this also means that a typical inter-particle (contact) force scales linearly with the particles' stiffness. Hence, the ratio of contact forces and stiffness, which can be interpreted as a mean particle-particle overlap, does not change when changing the particles' stiffness in a fixed volume quasi-static flow. Since particle-particle conductive heat flux is affected by the overlapping area between particles, one would also expect that for dense granular flow in the quasi-static regime the conductive heat flux is not affected by the particles' stiffness. Exactly this is what we observe in panel (b) of Fig. 3.9.

Again, as already seen in Fig. 3.9 panel (a), the conductive flux near a shear rate of $\dot{\gamma} = 10^{-1}$ has an exceptional character also for the very dense regime: a slight increase of the conductive heat flux can be observed, indicating the shift to the intermediate regime. After evaluating the influence of a variety of Biot numbers and particle stiffness on the conductive flux, we will now investigate their effect on the convective fluxes as defined in Eqn. (3.12).

3.4.2 Effect of the Peclet Number and Shear Rate on Convective Fluxes

A number of research groups already made an attempt to model the convective heat flux in sheared beds. Mohan et al. [14] investigated the convective transport in combination with wet particles including liquid bridge formation, but never studied the influence on the resulting thermal flux. Rognon et al. [17] investigated the scaling of the convective heat flux in the gradient direction, and found

that $q^{conv,y} \approx 10^{-2}\, q_s\, \tau$. The thermal number τ introduced by Rognon et al. scales linearly with the Peclet number defined in our contribution. Specifically, by assuming that the stress scales with k_n/d_p, we find from a comparison with Rognon et al.'s paper that $\tau =\sim \dot{\gamma} Pe$. Most important, since Rognon et al. [17] found that the particle stiffness has very little influence on the thermal transport rate for high Peclet numbers, τ and Pe are expected to be directly proportional and not affected by $\dot{\gamma}$. The previous work of Rognon et al. showed a regime map where the convective flux exceeds the conductive flux for $\tau \geq\approx 20$. We extend this previous analysis of Rognon et al. [17] to a variety of particle volume fractions, and have summarized our results in Fig. 3.10. For the moment we focus

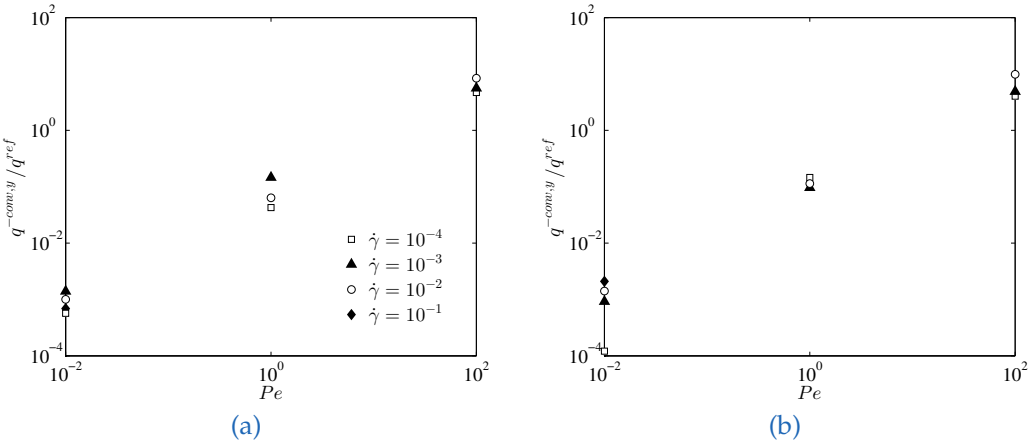

Figure 3.10: Influence of the Peclet number and dimensionless shear rate on the dimensionless convective flux. (a) $\phi_p = 0.54$, (b) $\phi_p = 0.62$.

on a low Biot number in order to be consistent with Rognon et al. [17]. Both particle volume fractions considered in the present work show similar values for the dimensionless convective heat flux, indicating that random particle motion is only mildly influenced by the particle concentration in our simulations. For high particle concentrations (i.e., flow in the quasi-static regime, see Fig. 3.10 (b)) our results are in good agreement with Rognon et al. [17]. This is true for both the slope with respect to the Peclet number, as well as the range of values. However, Rognon et al. [17] presented results in which an increase of the inertial number (i.e., $I \sim \dot{\gamma}$) does not necessarily cause an increase in the convective flux. This was reported to be especially the case at high Peclet numbers. We find that this is not always the case for somewhat lower particle concentrations: the dimensionless convective heat flux derived from our simulations indicated a significantly different, i.e., 1.5 times larger heat flux when increasing $\dot{\gamma}$ from 10^{-4} to 10^{-1}. In other words: our results indicate that softer particles clearly

lead to higher convective fluxes in dilute flows characterized by a low Peclet number.

We now have a closer look at the dependency of the convective fluxes near the critical particle concentration, i.e., the jamming point. Specifically, we consider the convective heat flux for the same particle stiffness (equal $\dot{\gamma}$) over a wide range of particle volume fractions. Fig. 3.11 (a) summarizes our findings for

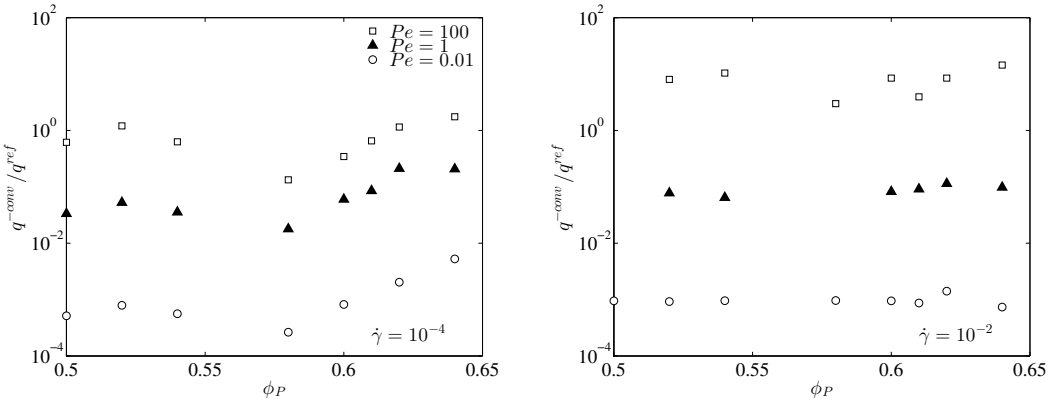

(a) (b)

Figure 3.11: Influence of the Peclet number and dimensionless shear rate on the dimensionless convective flux for a variety of particle volume fractions (a) $\dot{\gamma} = 10^{-1}$, (b) $\dot{\gamma} = 10^{-2}$.

comparably stiff particles, specifically, we observe a minimum for the convective flux at $\phi_p \approx 0.58$. We can only speculate on the origin of this minimum, which is clearly a result of the dependency of the particles' random motion on the particle concentration. A tentative explanation is that below the critical volume fraction the velocity in Eqn. (3.9) is the leading term. For $\phi_p > 0.58$ the internal energy of the particles ($m_{eff}\, c_p\, T_{vol,avg}$) is increasing, simply because more particles fit into a certain volume. However, the convective flux increases by approximately one order of magnitude in case we increase the particle volume fraction by just 5 percent. Hence, our simple explanation cannot fully describe such a strong increase in the thermal transport rate.

We finally note that according to Chialvo et al. [12] the critical particle volume fraction for transition to the quasi-static regime (in the context of granular rheology) is system dependant, and mainly influenced by the inter-particle friction coefficient. Specifically, this previous study identified a minimum critical volume fraction for $\mu = 1.0$ of ($\phi_c = 0.581$), and a maximum for $\mu = 0.0$ at ($\phi_c = 0.636$). Thus, when applying the results of our study, one needs to consider the inter-particle friction coefficient used in our present contribution.

Next, we consider the effect of the Biot number on the conductive fluxes.

3.4.3 Impact of the Biot Number on Conductive Fluxes

Fig. 3.12 depicts the influence of the Biot number on the conductive flux over a wide range of particle volume fractions. Thereby we focus on the highest and smallest studied Peclet number in order to gain some understanding how the speed of shearing affects the heat fluxes. As can be seen, the dimensionless conductive heat flux is constant for very low Biot numbers, and monotonically decreases with increasing Biot number (there are some fluctuations for $Pe = 100$, situations involving stiff particles, and comparably dilute particle beds. Conductive fluxes are very small for these systems, and hence not of primary interest). This trend is also seen for other Peclet numbers and dimensionless shear rates (data not shown). Most important, the point at which the the Biot number influences the conductive heat flux shows a minor dependence on the particle volume fraction ϕ_p and shear rate $\dot{\gamma}$. For $Pe = 0.01$ this point is $Bi \approx 10^{-2}$, while for $Pe = 100$ this point is located at $Bi \approx 1$. As seen before the scattering of conductive fluxes is inversely proportional to the dimensionless shear rate: higher dimensionless shear rates lead to less scattering (compare Fig. 3.12 (a) and (b)).

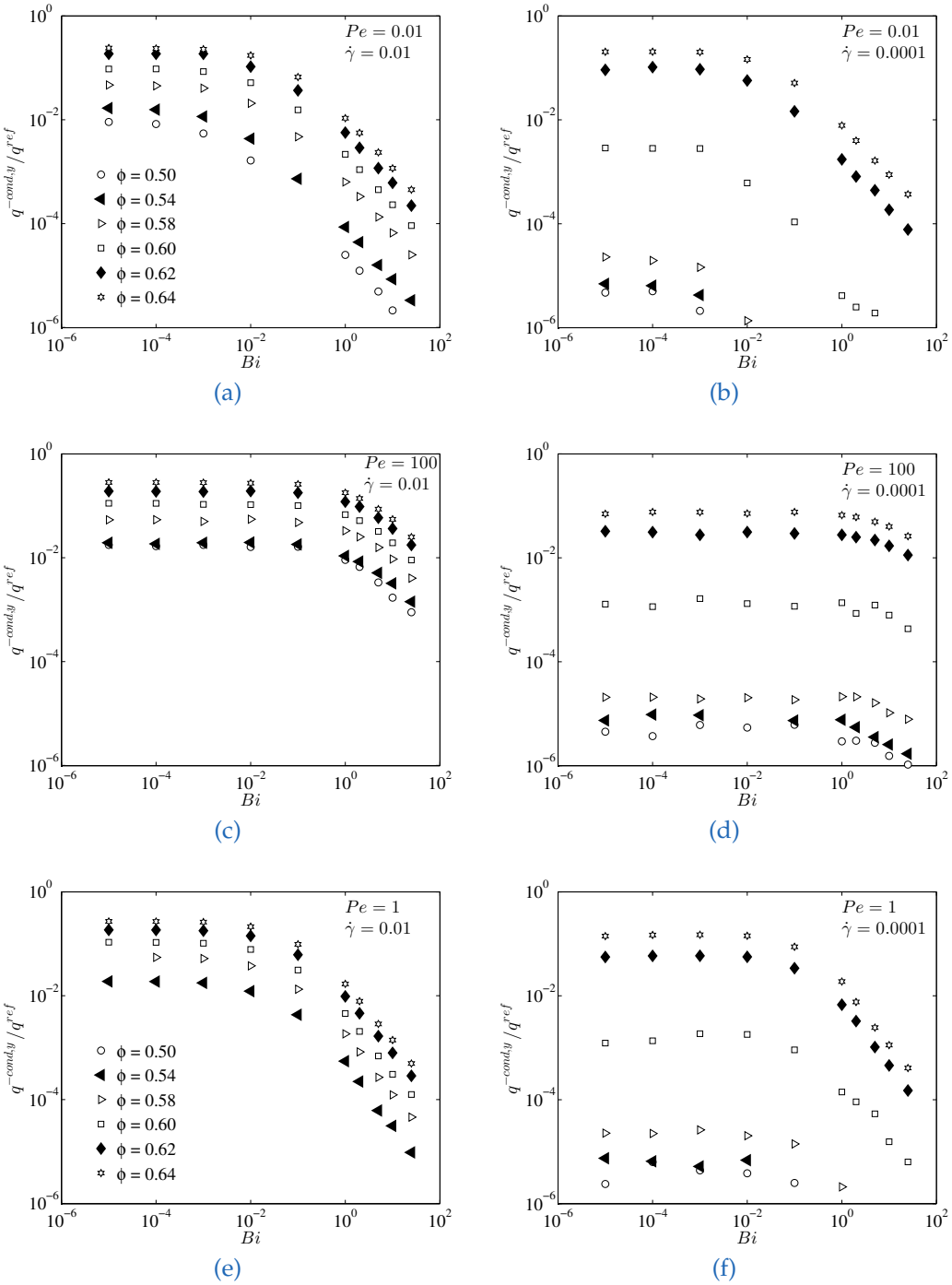

Figure 3.12: Influence of the Biot number on the conductive flux over a wide range of particle volume fractions. (a) $Pe = 0.01$, $\dot{\gamma} = 10^{-2}$, (b) $Pe = 0.01$, $\dot{\gamma} = 10^{-4}$, (c) $Pe = 100$, $\dot{\gamma} = 10^{-2}$, (d) $Pe = 100$, $\dot{\gamma} = 10^{-4}$, (e) $Pe = 1$, $\dot{\gamma} = 10^{-2}$, (f) $Pe = 1$, $\dot{\gamma} = 10^{-4}$.

A major dependency of the dimensionless conductive heat flux on the Peclet number is observed, especially for high Bi. According to Eqn. (3.20), at the same dimensionless shear rate and cooling rate (i.e, fixed α), an increase in the particles' thermal conductivity results in a lower Peclet number. However, in such a scenario the Biot number would also decrease inversely proportional to the heat conductivity. Thus, it is instructive to plot the conductive heat flux as a function of Π^{-1}, since then the particles' heat conductivity does not influence Π. Fig. 3.13 illustrates these data, where we can now easily identify the effect of intra-particulate heat transfer: for a fixed value of Π and a fixed dimensionless shear rate, a decrease in Pe reflects an increase of the particles' heat conductivity, and hence smaller intra-particle temperature gradients.

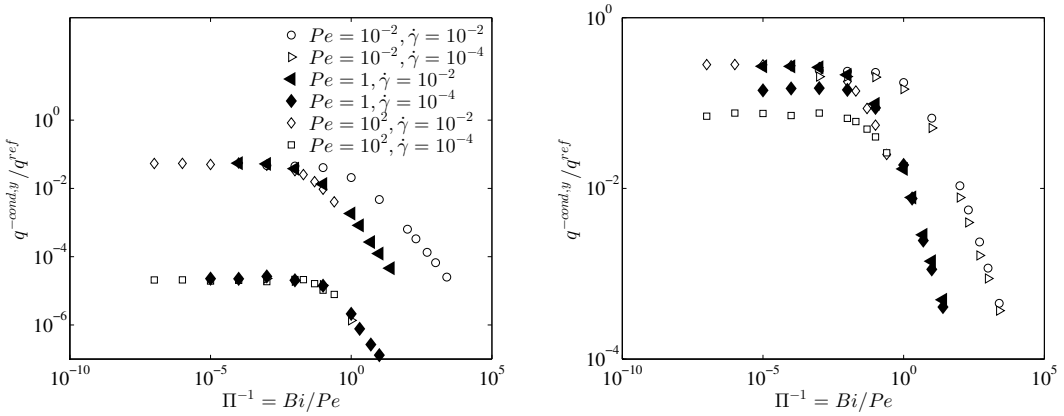

Figure 3.13: Influence of Π on the dimensionless conductive heat flux for (a) $\phi = 0.58$ and (b) $\phi = 0.64$.

If we now consider the data for $\dot{\gamma} = 10^{-2}$ in Fig. 3.13 panel (a), we observe that the conductive heat flux decreases upon an increase of the Peclet number (i.e., increasing intra-particle temperature gradients). Thus, the surface temperature for the case of $Pe = 100$ is closer to that of the ambient fluid, leading to a suppressed heat conduction. Surprisingly, this effect is less pronounced for stiff particles, i.e., $\dot{\gamma} = 10^{-4}$. The conductive heat transfer rate for such stiff and rapidly cooled particles is, however, small, and hence of no technological relevance. Considering a more dense particle bed (i.e., the data shown in Fig. 3.13 panel (b)), we see similar trends, illustrating the importance to account for intra-particle temperature gradients in situations in which dense particle beds are rapidly cooled or slowly sheared (i.e., Π is small). Interestingly, in particle beds undergoing fast shearing (characterized by large values for Π), the effect of intra-particle temperature gradients is rather small for $\phi = 0.58$. However,

as illustrated in Fig. 3.13 panel (b), for $\phi = 0.64$ and stiff particles, an increase of the Biot number (for $\Pi = const$) results in a large drop of the conductive flux. We have not systematically explored the origin of this effect. We speculate that it is due to the drop of the surface temperature in high Bi-number flows that greatly affects the conductive flux through the bed. After evaluating the influence of the Biot number, we now look more closely on the influence of the Peclet number in dense packed beds for a fixed Bi number. This is to illustrate the important effect of the speed of shearing on the conductive heat flux, which has been identified in the previous paragraph.

3.4.4 Effect of the Peclet Number on Conductive Flux at several Biot Numbers

In Fig. 3.14 we plot the dimensionless conductive heat flux over various Peclet numbers with different dimensionless shear rates and Biot numbers ranging from 10^{-5} to 25. As mentioned before, a higher Peclet number reflects a fast shearing of the particle bed. From Fig. 3.14 (panel (a) to (d)) we see that a change in the Peclet number has very little influence on the conductive heat flux for situations characterized by low Biot numbers (e.g. $Bi \leq 0.1$). This is in good agreement with Rognon et al. [17], and simply indicates that cooling caused by the ambient fluid is irrelevant since particles are quickly dispersed. In contrast, the dimensionless heat flux for higher Biot numbers strongly depends on the Peclet number: in some cases (e.g., Fig. 3.14, panel (a), $Bi = 25$) we observe changes up to three orders of magnitude in the conductive heat flux. In other flow situations (Fig. 3.14 (b),(c),(d)) the enhancement of the conductive heat flux is only seen for relatively high Peclet numbers. In summary, in dense particulate flows that are characterized by a larger Peclet number, a smaller difference of the conductive heat transfer rate is observed upon a change of the Biot number. The physical argument is, that in these quickly sheared beds heat is re-distributed by random particle motion, and hence intra-particle temperature gradients are of secondary importance.

As mentioned before, Rognon et al. [17] showed the existence of a general scaling law for the heat flux in sheared beds, and Mohan et al. [14] adapted and extended this to the flux of liquid adhering to the particles. We next make an attempt to establish a regime map that also accounts for the cooling by the ambient fluid.

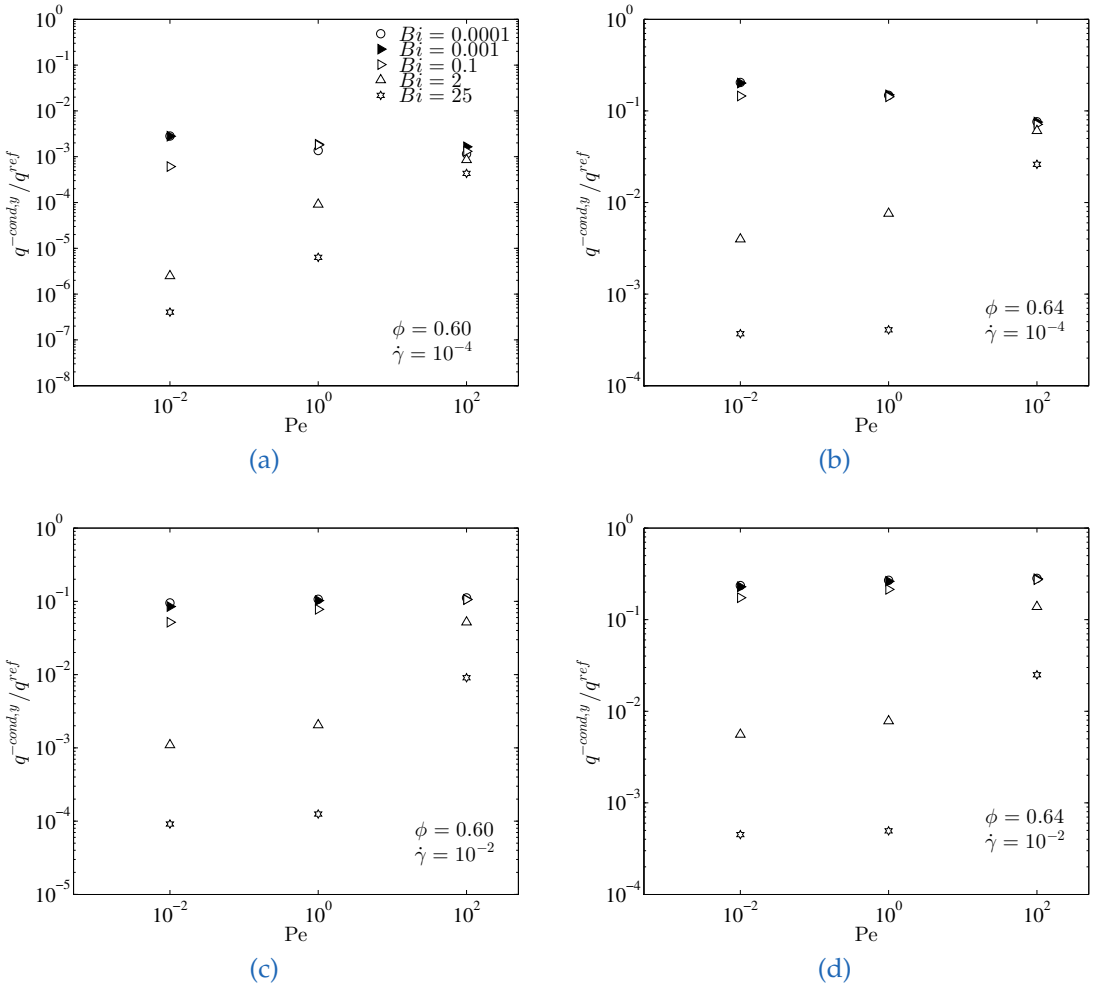

Figure 3.14: Influence of the Pelect number on the convective flux for (a) $\phi_p = 0.60$, $\dot{\gamma} = 10^{-4}$, (b) $\phi_p = 0.64$, $\dot{\gamma} = 10^{-4}$, (c) $\phi_p = 0.60$, $\dot{\gamma} = 10^{-2}$ (d) $\phi_p = 0.64$, $\dot{\gamma} = 10^{-2}$.

3.4.5 Regimes of Conductive Heat Transport

As demonstrated by Mohan et al. [14], a regime map for the conductive fluxes can be constructed by appropriate re-scaling of the dimensionless shear rate and fluxes. The idea is to perform simulations for a variety of particle concentrations (in our case ϕ was varied between 0.50 and 0.64), and then hope for a collapse of the data after the re-scaling operation. We also follow such and idea in the present contribution, and use for the re-scaling operation the exponents $a = 1/3, b = 7/5$ and $\phi_c = 0.613$ as shown in the axis labels of Fig. 3.15. Most important, in addition to the particle concentration, we have also varied the

Peclet and Biot number in our study. A collapse of the regimes for this variation in the thermal parameters would indicate that the (normalized) conductive flux is only a function of the flow parameters of the system (i.e., $\dot{\gamma}$ and ϕ). We now probe if this is truly the case.

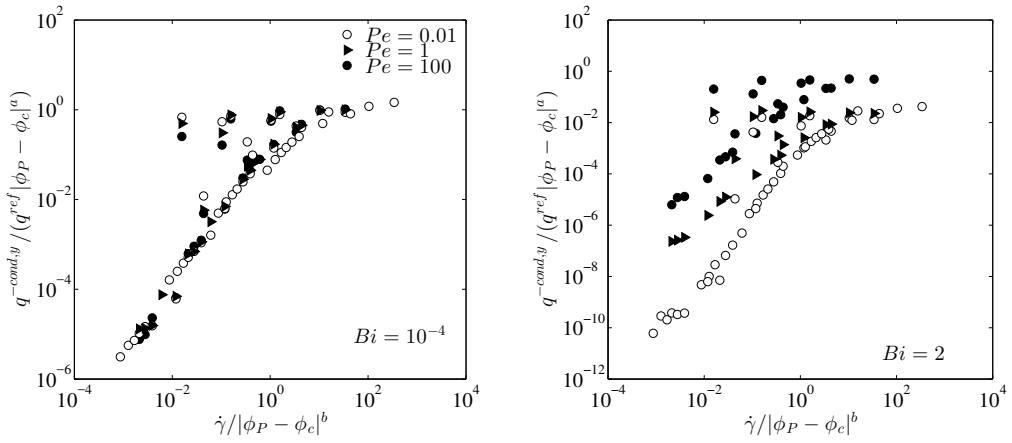

Figure 3.15: Influence of the Pelect number on the interial and quasi-static regime for (a) $Bi = 10^{-4}$, as well as (b) $Bi = 2$.

First, we investigate the influence of the Peclet number on the inertial and quasi-static regime at fixed Biot numbers. Fig. 3.15 panel (a) reveals the dependency of the re-scaled fluxed on the Peclet number for a slow rate of cooling, i.e., $Bi = 10^{-4}$. Our data indicates a reasonable agreement of the re-scaled data for all studied Peclet numbers (note that we studied $Pe = 0.01$ in most detail). Since we focus on particle volume fractions with $\phi_p \geq 0.50$, all three flow regimes known from granular rheology can be identified: (i) an interial regime characterized by a quadratic increase of the conductive flux with the shear rate, (ii) a quasi-static regime where fluxes are independent of the shear rate, and (iii) an intermediate regime that is only relevant for very soft particles. Most important, our data is also in good agreement with the previous work of Mohan et al. [14]. Clearly, this is due to the small amount of heat transferred to the ambient fluid: in Fig. 3.15 panel (a) we considered a very small Biot number, and large values for Π ranging from 10^2 to 10^6. The latter hints to the fact that the rate of cooling is small compared to convective heat transport, i.e., the redistribution of thermal energy due to particle motion in our simulation domain is fast.

As one might anticipate, a different behaviour will develop at higher Biot numbers, i.e., in case particles are rapidly cooled by the ambient fluid. Specifically, at

a Biot number of $Bi = 2$, and as shown in Fig. 3.15 panel (b), we observe that the Peclet number has a critical effect on the conductive heat flux. First, considering the data for $Pe = 100$ (i.e., $\Pi = 50$) we observe that conductive heat fluxes are still of comparable magnitude to that observed for $Bi = 10^{-4}$. Also, the three regimes can be identified, all with the same scaling with respect to the shear rate. The physical interpretation is that the redistribution of thermal energy is still fast compared to the cooling rate as indicated by the large value for Π. Thus, particles cannot cool down significantly while they move through the shear flow in our simulations. Consequently, the Biot number (characterizing the intra-particle temperature distribution) has little effect for large Peclet number flows as long Π is large. This is due to the fact that the overall cooling of the particles is small, and hence intra-particle temperature gradients are (relative to the temperature gradient applied to the simulation domain) also small.

Most important, the situation changes as we decrease the Peclet number: for $Pe = 1$ (i.e., $\Pi = 0.5$) we already see a substantial decrease of the conductive heat flux, and with decreasing Pe (and hence $\Pi \ll 1$) thermal transport due to conduction is increasingly suppressed. Also, the slope of the curve characterizing the normalized conductive heat flux in the inertial regime appears to gradually increase with decreasing Π. However, this increase is rather small. We do not attempt to speculate on the physical origin of this finding due to the lack of more data that can support our arguments.

The physical interpretation of the observed decrease of the conductive heat flux for intermediate and small Pe numbers is that a layer of "equilibrated" particles forms: these particles have a temperature close to that of the ambient fluid. Consequently, this layer of equilibrated particles chokes off the conductive heat flux through the simulation box, since heat is primarily transferred to the ambient fluid. Clearly, this layer becomes thicker (and the layer in which particles still having an appreciable temperature gradient becomes thinner) when decreasing Π. As already discussed in our theoretical analysis presented in Section 3.3.3, the size of the simulation domain is important in these situations: clearly, the size of the simulation domain determines the relative thickness of the layer containing equilibrated particles, and hence affects the computed (domain-averaged) heat fluxes.

3.5 Conclusions

We investigated the heat transfer through a sheared bed of inertial particles that is cooled with a fixed rate by an ambient fluid. Also, we presented the newly developed library *ParScale* which we coupled to the well established DEM solver *LIGGHHTS*. This library, which models intra-particle transport processes, was used to resolve radial temperature profiles within every single particle. This enabled us to model the effect of the transferred heat flux (to the ambient fluid) on intra-particle temperature profiles. Hence, we accounted for the competition of heat transferred to the surrounding fluid, and the rate of heat conduction within the particles.

Next, we presented a simple analytical solution for the temperature profile in a sheared bed, and proved the consistency of this solution with our simulation data. Our solution is applicable over a wide range of flow situations, and requires the specification of only one additional system-dependent parameter if applied to simple shear flow.

Furthermore, we showed that our approach to discretize the particle in only one spatial direction (i.e., radially) is in good agreement with data obtained from direct numerical simulations (DNS) that utilize a full three-dimensional discretiztion. Specifically, our simulations indicate that the difference between DNS data, and the data obtained from an one-dimensional discretization is decreasing with rising Reynolds numbers. Also, the ratio of the thermal conductivities of the particle and the surrounding fluid is of a certain significance. Often, intra-particle temperature gradients are of industrial relevance only in high Reynolds number flows (i.e., large particles), and less important in case fluid-particle relative motion is slow (i.e., small Reynolds numbers). This suggests that our approach that relies on *ParScale* is an affordable, yet accurate way to account for intra-particle temperature gradients.

We then studied thermal transport rates for granular flows characterized by a low Biot number (i.e., slow heat transfer to the surrounding fluid), and found good agreement with literature data that considered particles in vacuum. Also, we extended the analysis by studying a wide range of particle volume fractions. Most important, in situations characterized by a small dimensionless shear rate we found that the convective flux shows a global minimum at the critical particle volume fraction. This finding coincides with the well known maximum in the fluctuations of the (normalized) pressure at the critical state. For softer particles (i.e., flows characterized by a large dimensionless shear rate) this minimum vanishes. The convective heat flux is then nearly unaffected by the particle concentration.

Subsequently, we focused on higher Biot numbers, and studied the influence of the Biot and Peclet number on the conductive heat flux through a sheared particle bed. We found that the conductive heat flux remains almost constant for relevant Biot numbers (i.e., speeds of cooling) at high Peclet numbers. For dense flows only a weak dependency is seen with respect to the particle stiffness, whereas for more dilute flows the conductive heat flux drops by more than one order of magnitude in case the particle stiffness is increased. This clearly hints to different regimes of heat conduction in dense and dilute beds, in analogy to the three stress regimes that are well accepted in granular rheology.

In order to make one step towards an unified model to predict thermal transport through sheared particle beds, we made an attempt to collapse the scaled conductive heat fluxes. We find that for some of the investigated flow situations the conductive heat fluxes can be collapsed into a single curve. This is a strong indication that an unified regime map that characterizes the mode of heat conduction in a cooled bed of particles can be constructed. Specifically, we showed that for high Peclet and small Biot numbers (i.e., large values for the parameter Π) the map characterizing the conductive heat flux is nearly independent of the Biot number. Thus, our data can be used to make reliable predictions of conductive heat transfer rates for these situations. In contrast, for small Peclet and high Biot numbers still challenges remain to close our model. Clearly, in order to create a rigorous regime map that allows a precise calculation of conductive, convective and transferred heat transfer rates, a deeper analysis of the data presented in this study is necessary. Most important, such an analysis has to account for the (normalized) size of the simulation domain. This is due to the nature of particle cooling in a granular shear flow, which leads to a non-uniform temperature gradient. We expect that the newly introduced parameter Π, as well as the newly derived expression for the local temperature gradient (see Section 3.3.3), will be inspiration for future work that may account for these effects.

The work of Morris et al. [15] discussed the effect of stiffness on the results, and provides a stiffness correction. Similarly, our results could be used to propose such a stiffness correction. Indeed, and as outlined in Morris et al. [15], developing such a correction for dense granular flows remains a delicate task.

Our study certainly has some limitations: especially in dense flows of soft particles, our approach to model the transferred heat flux should be extended by accounting for the surface area of the particle that is covered due to particle deformation during a collision. For example, this could be done using well established expressions for the particle-particle contact area, or (in more extreme situations with respect to particle concentration and softness) once could adopt

a Monte Carlo area integration method. Such a method is already implemented in *LIGGGHTS*. Another important assumption of the present analysis was that the ambient fluid is kept at a fixed temperature. This assumption is valid as long as the heat transferred to the fluid is quickly removed, e.g., convection in the ambient fluid is sufficiently strong. Specifically, this means that the spatial fluid temperature variation is small over a characteristic distance (i.e., a few particle diameters), which is the case for high fluid Peclet numbers, and depends on the particle concentration (Munichi et al. [39]). This assumption of fast convective transport holds for most applications involving comparably large (i.e., mm-sized) particles suspended in a gas. However, future thoughts may extend our present work to applications that are characterized by extreme temperature gradients, i.e., systems involving smaller particles and low fluid Peclet numbers (i.e., slow fluid-particle relative motion). Also, since we fixed the ambient fluid temperature and the heat transfer coefficient, both quantities must be provided from a supplementary fluid model (e.g., that used in Kuipers et al. [25]). This exceeded the current study, however, can be implemented in a straight forward manner. Future considerations could then establish an even more rigorous understanding of thermal transport in flowing granular matter and the ambient fluid encountered in a number of engineering applications.

3.6 Nomenclature

3.6.1 Latin Characters

Variable	Unit	Meaning
a, b		Fitting constants for regime map
a	$\mathrm{m^2\,s^{-1}}$	Thermal diffusivity
A	$\mathrm{m^2}$	Cross sectional area
c		Integration constant
c_p	$\mathrm{J\,kg^{-1}\,K^{-1}}$	Heat capacity
C		Number of contacts
d	m	Diameter
e		Coefficient of restitution
Fo		Fourier number
$\mathbf{f}$	N	Force on particle
g^*		Dimensionless bed morphology parameter
h		Spatial index
H	m	Height of simulation domain
I	$\mathrm{kg\,m^2}$	Moment of inertia, Inertia number
k	$\mathrm{N\,m^{-1}}$	Spring stiffness
m	kg	Mass
n		Number of particles
p	$\mathrm{m^2\,s^{-2}}$	Pressure normalized with density
Pe		Peclet number
Pr		Prandt number
q	$\mathrm{W\,m^{-2}}$	Heat flux
Q	W	Heat exchange rate
r	m	Particle radius
Re		Reynolds number
U	m	Perimeter
$\mathbf{u}$	$\mathrm{m\,s^{-1}}$	Fluid velocity
t	s	Time
T	K	Temperature
$\mathbf{v}$	$\mathrm{m\,s^{-1}}$	Particle velocity
V	$\mathrm{m^3}$	Domain volume
Y	$\mathrm{N\,m^{-2}}$	Young's modulus
$\mathbf{x}$	m	Particle position

3.6.2 Greek Characters

Variable	Unit	Meaning
α	$\mathrm{W\,m^{-2}\,K^{-1}}$	Heat transfer coefficient
δ	m	Overlap distance during a particle–particle contact
$\dot{\gamma}$		Dimensionless shear rate
γ	$\mathrm{s^{-1}}$	Shear rate
μ		Friction coefficient
μ	Pa s	Dynamic viscosity
η	$\mathrm{N\,s\,m^{-1}}$	Viscous damping coefficient
ω	$\mathrm{rad\,s^{-1}}$	Eigen frequency of damped harmonic oscillator
θ	K	Temperature difference
ϕ		Particle volume fraction
ϵ		Overlap area in case of particle-particle contact
Π		Dimensionless length characterizing convective heat transport
λ	$\mathrm{W\,m^{-1}\,K^{-1}}$	Thermal conductivity
ρ	$\mathrm{kg\,m^{-3}}$	Density
τ		Thermal number

3.6.3 Superscripts

Variable	Meaning
$conv$	Convection
$cond$	Conductive
$drift$	Drift value
n	Normal direction
t	Tangential direction
$trans$	Transferred
x, y, z	Direction

3.6.4 Subscripts

Variable	Meaning
0	Initial state
avg	Average Value
bot	Bottom
c	Critical Value
$char$	Characteristic value
co	Contact points in system
cyl	Cylinder
$drift$	Drift value
eff	Effective value
f	Fluid
i, j	Particle index
$inert$	Inertial
int	Intermediate
p	Particle
QS	Quasi-static
top	Top
s	Summation
vol	Volumetric Value
x, y, z	Directions

3.7 Appendices

Appendix A: DEM Parameters and Calculation Routines

The normal spring stiffness and the coefficient of restitution were set by adjusting the effective Young's modulus Y_{eff} and the damping coefficient η. Thus, the following equations were applied:

$$k = \frac{16}{15}\sqrt{r_{eff}}\,Y_{eff}\left(\frac{15\,m_{eff}\,v_{char}^2}{16\sqrt{r_{eff}}\,Y_{eff}}\right)^{1/5}, \tag{3.39}$$

$$Y_{eff} = \left[\frac{(\gamma/\gamma^*)^2 d_p^3 \rho_p}{(16/15)^{4/5}(r_{eff})^{2/5}(m_{eff})^{1/5}(v_{char})^{2/5}}\right]^{5/4}, and \tag{3.40}$$

$$\eta = \sqrt{\frac{4\,m_{eff}\,k}{1+\left(\frac{\pi}{\ln(e)}\right)}} \tag{3.41}$$

Note that the characteristic impact velocity v_{char} drops out of Eqn. (3.39) after inserting Eqn. (3.40) and therefore is irrelevant for the subsequent dimensional analysis. Tab. (3.5) outlines the adjusted parameter in order to obtain the dimensionless shear rate $\dot{\gamma}$.

Table 3.5: Adjusted DEM parameters.

$\dot{\gamma}$	Y_{eff}	$\triangle t$
10^{-1}	$1.32\,10^{3}$	$2.50\,10^{-3}$
10^{-2}	$4.18\,10^{5}$	$2.50\,10^{-4}$
10^{-3}	$1.32\,10^{8}$	$2.50\,10^{-5}$
10^{-4}	$4.18\,10^{10}$	$2.50\,10^{-6}$

Appendix B: CDS scheme

For discretisation in physical space a second order accurate scheme (i.e., a central differences scheme) is used for the first and second derivative:

$$\frac{\partial T}{\partial r} = \frac{T_{h+1} - T_{h-1}}{2 \triangle r} + O(\triangle r^2) \tag{3.42}$$

$$\frac{\partial^2 T}{\partial r^2} = \frac{T_{h+1} + T_{h-1} - 2T_h}{\triangle r^2} + O(\triangle r^2) \tag{3.43}$$

Appendix C: Verification Case - Cooling of a Sphere

The verification case considers a situation in which a spherical particle, initialized with the uniform temperature T_0, is cooled by an ambient fluid with temperature T_f. Tab. (3.6) summarizes the parameters of this case. Fig. 3.16 illustrates the comparison between the numerical solution by *ParScale* and the analytical solution provided by [40] for a number of time coordinates. A very good agreement can be found over all investigated times and spatial coordinates with an average relative error of 10^{-5}.

Table 3.6: Parameters for the verification case 'cooling of a sphere'.

c_p	300	$[\mathrm{J\,m^{-3}\,K}]$
ρ	1000	$[\mathrm{kg\,m^{-3}}]$
λ_p ,h,h	1	$[\mathrm{W\,m^{-1}\,K^{-1}}]$
α	100	$[\mathrm{W\,m^{-2}\,K^{-1}}]$
r_p	$5 \cdot 10^{-3}$	[m]
T_0	800	[K]
T_f	300	[K]
t_1, t_2, t_3, t_4	2,5,8,10	[sec]

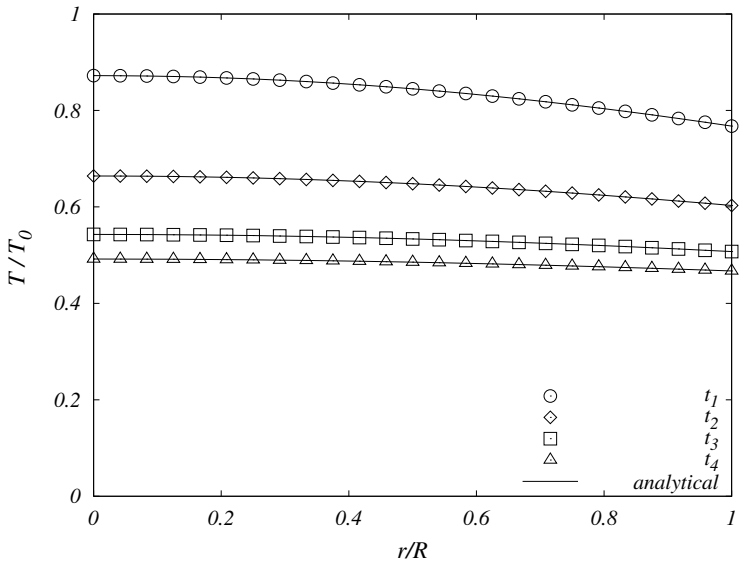

Figure 3.16: Numerical (symbols) and analytical results (lines) for the temperature distribution in a sphere cooled by convection at t_1 = 2 s, t_2 = 5 s, t_3 = 8 s, and t_4 = 10 s.

3.8 Bibliography

[1] T. Forgber, B. Mohan, C. Kloss, and S. Radl. Heat transfer rates in sheared beds of inertial particles at high biot numbers. *Granular Matter*, 19(1):14, 2017.

[2] Y. L. Ding, R. N. Forster, J. P K Seville, and D. J. Parker. Some aspects of heat transfer in rolling mode rotating drums operated at low to medium temperatures. *Powder Technology*, 121(2-3):168–181, 2001.

[3] S. Rickelt, F. Sudbrock, S. Wirtz, and V. Scherer. Coupled DEM/CFD simulation of heat transfer in a generic grate system agitated by bars. *Powder Technology*, 249:360–372, 2013.

[4] B. Peters. *Thermal Conversion of Solid Fuels (Developments in Heat Transfer)*. WIT Press, 2002.

[5] A. Smart and J. M. Ottino. Granular matter and networks: three related examples. *Soft Matter*, 4(11):2125, 2008.

[6] D. Shi, W. L. Vargas, and J.J. McCarthy. Heat transfer in rotary kilns with interstitial gases. *Chemical Engineering Science*, 63(18):4506–4516, 2008.

[7] W. L. Vargas and J. J. McCarthy. Heat conduction in granular materials. *AIChE Journal*, 47(5):1052–1059, 2001.

[8] J. R. Rice. Heating and weakening of faults during earthquake slip. *Journal of Geophysical Research: Solid Earth*, 111(5):1–29, 2006.

[9] J. Sulem, P. Lazar, and I. Vardoulakis. Thermo-poro-mechanical properties of clayey gouge and application to rapid fault shearing. *International Journal for Numerical and Analytical Methods in Geomechanics*, 31(3):523–540, 2007.

[10] K. Otsuki. Fluidization and melting of fault gouge during seismic slip: Identification in the Nojima fault zone and implications for focal earthquake mechanisms. *Journal of Geophysical Research*, 108(B4), 2003.

[11] F. Alonso-Marroquín, I. Vardoulakis, H. J. Herrmann, D. Weatherley, and P. Mora. Effect of rolling on dissipation in fault gouges. *Physical Review E - Statistical, Nonlinear, and Soft Matter Physics*, 74:031306, 2006.

[12] S. Chialvo, J. Sun, and S. Sundaresan. Bridging the rheology of granular flows in three regimes. *Physical Review E - Statistical, Nonlinear, and Soft Matter Physics*, 85:021305, 2012.

[13] S. Luding. Introduction to Discrete Element Methods Basics of Contact Force Models and how to perform the Micro-Macro Transition to Continuum Theory. *European Journal of Environmental and Civil Engineering*, (12):785–826, 2008.

[14] B. Mohan, C. Kloss, J. Khinast, and S. Radl. Regimes of Liquid Transport through Sheared Beds of Inertial Smooth Particles. *Powder Technology*, 264:377–395, 2014.

[15] A. B. Morris and S. Americas. Development of Soft-Sphere Contact Models for Thermal Heat Conduction in Granular Flows. *AIChE Journal*, 02(00):1–10, 2016.

[16] T. Tsory, N. Ben-Jacob, T. Brosh, and A. Levy. Thermal DEM-CFD modeling and simulation of heat transfer through packed bed. *Powder Technology*, 244:52–60, 2013.

[17] P. Rognon, I. Einav, J. Bonivin, and T. Miller. A scaling law for heat conductivity in sheared granular materials. *EPL (Europhysics Letters)*, 89(5):1–6, mar 2010.

[18] P. Rognon and I. Einav. Thermal transients and convective particle motion in dense granular materials. *Phys. Rev. Lett.*, 105:218301, 2010.

[19] G. K. Batchelor and R. W. O'Brien. Thermal or electrical conduction through a granular material. *Proceedings of the Royal Society of London A: Mathematical, Physical and Engineering Sciences*, 355(1682):313–333, 1977.

[20] Yoshiyuki Shimizu. Three-dimensional simulation using fixed coarse-grid thermal-fluid scheme and conduction heat transfer scheme in distinct element method. *Powder Technology*, 165(3):140–152, 2006.

[21] G. J. Cheng, A. B. Yu, and P. Zulli. Evaluation of effective thermal conductivity from the structure of a packed bed. *Chemical Engineering Science*, 54:4199–4209, 1999.

[22] Y. T. Feng, K. Han, and D. R J Owen. Discrete thermal element modelling of heat conduction in particle systems: Pipe-network model and transient analysis. *Powder Technology*, 193(3):248–256, 2009.

[23] Y. T. Feng, K. Han, C. F. Li, and D. R J Owen. Discrete thermal element modelling of heat conduction in particle systems: Basic formulations. *Journal of Computational Physics*, 227(10):5072–5089, 2008.

[24] T. Oschmann, M. Schiemann, and H. Kruggel-Emden. Development and verification of a resolved 3D inner particle heat transfer model for the discrete element method (DEM). *Powder Technology*, 291:392–407, 2015.

[25] J. A. M. Kuipers, W. Prins, and W. P. M. Van Swaaij. Numerical calculation of wall-to-bed heat-transfer coefficients in gas-fluidized beds. *AIChE Journal*, 38(7):1079–1091, 1992.

[26] X. Yin and S. Sundaresan. Drag law for bidisperse gassolid suspensions containing equally sized spheres. *nd. Eng. Chem. Res.*, 48:227–241, 2009.

[27] S. Radl, T. Forgber, A. Aigner, and C. Kloss. ParScale - An Open-Source Library for the Simulation of Intra-Particle Heat and Mass Transport Processes in Coupled Simulations. *IV International Conference on Particle-based Methods – Fundamentals and Applications (PARTICLES 2015)*, pages 46–55, 2015.

[28] T. Forgber, J. R. Tolchard, A. Zaabout, P. I. Dahl, and S. Radl. Optimal Particle Parameters for CLC and CLR Processes - Predictions by Intra-Particle Transport Models and Experimental Validation. *IV International Conference on Particle-based Methods – Fundamentals and Applications (PARTICLES 2015)*, pages 101–111, 2015.

[29] W.; Ranz and Wl Marshal. Evaporation from drops. *Chem. Eng. Prog.*, (48):141–146, 1952.

[30] D.J. Gunn. Transfer of heat or mass to particles in fixed and fluidised beds. *International Journal of Heat and Mass Transfer*, 21(4):467–476, 1978.

[31] C. Kloss, C. Goniva, A. Hager, S. Amberger, and S. Pirker. Models , algorithms and validation for opensource DEM and CFD-DEM. *Progress in Computational Fluid Dynamics*, 12:140–152, 2012.

[32] https://github.com/CFDEMproject/ParScale-PUBLIC, accessed May 2017.

[33] K. N. Nordstrom, E. Verneuil, P. E. Arratia, Z. Zhang, G. Yodh, J. P. Gollub, and D. J. Durian. Microfluidic rheology of soft colloids above and below jamming. *Physical Review Letters*, 105:175701, 2010.

[34] T. Hatano. Scaling properties of granular rheology near the jamming transition. *Journal of the Physical Society of Japan*, 77(12):18–21, 2008.

[35] M. Otsuki and H. Hayakawa. Critical behaviors of sheared frictionless granular materials near the jamming transition. *Physical Review E - Statistical, Nonlinear, and Soft Matter Physics*, 80:011308, 2009.

[36] R. Schmidt and P. Nikrityuk. Numerical simulation of the transient temperature distribution inside moving particles. *The Canadian Journal of Chemical Engineering*, 90:246–262, 2012.

[37] P. Nikrityuk and B. Meyer. *Gasification Processes: Modeling and Simulation*. 1 edition, 2014.

[38] R. Mehrabian, S. Zahirovic, R. Scharler, I. Obernberger, S. Kleditzsch, S. Wirtz, V. Scherer, H. Lu, and L. L. Baxter. A CFD model for thermal conversion of thermally thick biomass particles. *Fuel Processing Technology*, 95:96–108, 2012.

[39] F. Municchi and S. Radl. Consistent closures for Euler-Lagrange models of bi-disperse gas-particle suspensions derived from particle-resolved direct numerical simulations. *submitted to: International Journal of Heat and Mass Transfer*, 2016.

[40] J. Crank. *The Mathematics of Diffusion*. Clarendon Press, Oxford, 2nd edition, 1975.

4 Heat Transfer Rates in Wall Bounded Shear Flows near the Jamming Point accompanied by Fluid-Particle Heat Exchange[1]

4.1 Introduction

Sheared particle beds occur in a large variety of industrial and geological applications. Many researchers investigated related phenomena like critical jamming behaviour, rheological models, crystallization and stress relaxation over the past years. Early work was focused on dilute flows with fluid-like behaviour (*inertial* flows) where kinetic theory can be applied (Garzo et al. [2], Lun et al. [3], Jenkins et al. [4], Johnson et al. [5]). On the contrary it was found that dense flows (*quasi-static*) can be described using plasticity models (Chialvo et al. [6]). More recent publications aim on rheology models around the transition regime in flows that involve frictionless spheres (Hatano [7], Nordstrom et al. [8], Seth et al. [9], Otsuki et al. [10]). Scaling of the normal and shear stress tensor has been used with success for a wide range of volume fractions and dimensionless shear rates to collapse the rheological data.

Drawing back to industrial applications, granular matter is typically described as an ensemble of frictional, stiff spheres, and past work was mostly focused on the critical jamming and rheology behaviour of these materials (Otsuki et al. [11], Zhang et al. [12], Song et al. [13], Majmudar et al. [14], Tighe et al. [15], Vescovi et al. [16]). Referring to the original jamming diagram by Liu et al. [17], the influence of the friction coefficient was not taken into account. However, more advanced theories consider frictional, jammed granular materials, were developed based on the interest to more application-oriented problems (Luding

[1] This Chapter is based on [1]. T.F. has set up and post-processed the simulations and has written the manuscript.

[18]). The initial work of Liu et al. [17] also triggered the development of advanced jamming diagrams (Ciamarra et al. [19], Brown et al. [20]). Clearly, most models from literature (i.e. Chialvo et al. [6], Rognon et al. [21] and Mohan et al. [22]) rely on the contact pressure or related quantities to determine the state of the system (e.g., unjammed, jammed or in the ordering process). In fact, the contact pressure is very sensitive to the applied modelling technique and system, and hence is certainly suitable from a rheological point of view to characterize jamming.

The majority of the above-mentioned work (i.e. Chialvo et al. [6], Rognon et al. [21], Mohan et al. [22]) relied on the Molecular Dynamics (MD) or Discrete Element Method (DEM), and mostly focussed on the rheological behaviour of granular matter in a fully periodic domain. Typically, a rather rudimentary approach for the local particle temperature distribution was adopted, or the system was treated as isothermal. With the focus on predicting local temperatures in chemical reactors for, e.g., CO_2 absorption, or biomass combustion, a reliable model is still missing in literature. Only a few researchers made the attempt to model thermal fluxes in sheared beds. For example, Mohan et al. [22] showed the existence of different regimes of conductive and convective liquid transport in a sheared particle bed, and similarities between the transport of thermal energy and liquid adhering to the surface of the particles have been discussed. Thereby, a dimensionless shear rate and a Peclet number were identified as the key dimensionless parameters. Unfortunately, the work of Mohan et al. [22] relied on the assumption of zero heat flux to the ambient fluid, critically limiting the applicability of their conclusions. Rognon et al. [21], [23] did not even attempt to model the transferred heat from the particle to the ambient fluid (e.g., air), but was successful in formulating scaling laws for conductive heat fluxes in the system. As previous work was mostly performed using the Lees-Edwards boundary conditions [24], it is also unknown how an application-oriented boundary (e.g., flat walls) influences the thermal fluxes. This is, however, of great significance since the heat exchange with walls often dominates the temperature distribution within a reactor, and hence its performance. Even the effect of walls on the scaling of, e.g., the convective flux due to the random movement of the particles [23], is still unknown.Also, there is currently no hope to reliably predict thermal fluxes to, or near walls in the context of continuum models, even if we assume isothermal particles.

In summary, there is still very little quantitative knowledge about the thermal behaviour of a wall-bounded particle bed. This is especially true for granular material that consists of particles with a non-uniform temperature profile, and which exchanges heat with the ambient fluid. Clearly, a thorough understanding

of the relative rates of (i) the transferred heat to the ambient fluid, (ii) the convective heat transport in the granular material, as well as (iii) the heat that is transported via conduction is still missing in literature. For the ambient fluid we limit our study to systems of high particle Stokes numbers ($St = 2/9\,\rho_p \mathbf{u} d_p / \mu_f$). This includes systems that comprised gases or liquids with a low viscosity and particles with a sufficiently high density. Also, a critical assessment of the influence of friction coefficient and diameter distribution on the effect of crystallization and jamming is needed. Most importantly, combining recent results on the jamming behaviour, as well as on crystallization effects with recently developed methods to study thermal transport in these system seems necessary.

It is our goal to improve the current state of the art related to thermal behaviour in sheared materials by coupling DEM-based simulations to a tool that is capable of resolving intra-particle temperature profiles. The tool *ParScale* (Radl et al. [25], Forgber et al. [26], [27]) allows us to efficiently solve an one-dimensional heat conduction equation within each particle. By means of such coupled DEM-based simulations, a generally applicable continuum model for predicting thermal fluxes in granular materials can be established. Such a model is of utmost importance for the correct selection of an appropriate simulation model for a specific fluid-particle heat transport problem, e.g., to model a non-isothermal heterogeneous reactor. In our present contribution we analyse temperature gradients by probing an adequate space of dimensionless parameters, most importantly the Biot and Peclet numbers, in a wall-bounded shear flow. This allows us to draw conclusions that are applicable to a wide range of real-world applications, and would help to lay the foundation for an advanced continuum model of non-isothermal granular flows in the future.

Our manuscript is structured as follows: first (in Section 4.2) the simulation method is explained and an overview of all equations solved is presented, including the known and unknown simulation parameters. In Section 4.3 we identify and define the most influential dimensionless parameters which enable us to scale our results, and apply the outcome of the study to a wide range of relevant industrial applications. In Section 4.4, simulation results including schematic drawings of our wall bounded shear box set-up with studied parameter ranges are presented. Section 4.5 summarizes the study and outlines ideas for follow-up work. Note that we included a Nomenclature (Section 4.6) at the end of our manuscript where all symbols are defined.

4.2 Simulation Method

As in earlier work (Forgber et al. [27]), we do not solve any equation for the fluid phase (e.g. ambient fluid) and assume a fixed heat transfer coefficient α, as well as a fixed ambient fluid temperature t_f. In the final application of our models, these quantities are provided by an external Finite Volume Method (FVM) solver, and hence are known. All equations solved are summarized in Tab. (4.1), as well as all unknown particle parameters in Tab. (4.2).

4.2.1 Particle Flow Model

In order to correctly account for particle movement and particle-particle interactions we rely on the open-source software package *LIGGGHTS* [28], [22] which is a state of the art tool to perform Discrete Element Method-based simulations. This tool, together with a spring-dashpot model is used to predict particle-particle and particle-wall contact forces [28]. Specifically, the following contact force models in the tangential (i.e., $\mathbf{f}_{i,j}^{t}$) and normal direction (i.e., $\mathbf{f}_{i,j}^{n}$) were used:

$$\mathbf{f}_{i,j}^{n} = k^n \, \delta_{ij} \mathbf{n}_{ij} - \eta^n \, \mathbf{v}_{ij}^{n} \tag{4.1}$$

$$\mathbf{f}_{i,j}^{t} = -k^t \, \mathbf{u}_{ij}^{t} - \eta^t \mathbf{v}_{ij}^{t} \tag{4.2}$$

with:

$$\delta_{ij} = r_i + r_j - \mid \mathbf{x}_i - \mathbf{x}_j \mid . \tag{4.3}$$

In the case of overlapping particles the normal overlap δ_{ij} is positive.

In what follows we give an overview about the most important quantities needed to interpret our work. For the meaning of the remaining symbols (which are not discussed in the text), we refer the interested reader to the Nomenclature presented at the end of the manuscript (see Section 4.6).

The characteristic contact time t_{co} of the above linear spring-dashpot model is defined as:

$$t_{co} = \pi \, / \, \omega \tag{4.4}$$

with

$$\omega = \sqrt{(k/m_{eff} - \eta^2)/(4\,m_{eff}^2)}. \tag{4.5}$$

Thereby, the contact time t_{c0} limits the time step $\triangle t$ for the integration of Newtons equations of motion. The coefficient of restitution e^n is defined as

$$e^n = \exp\left(\frac{-\pi\eta^n}{m_{eff}\sqrt{4\,k^n/m_{eff} - \eta^{n^2}/m_{eff}^2}}\right) \tag{4.6}$$

and was adjusted to 0.9. For relevant parameter ranges and constants studied in our present work we refer to Tab. (4.3). The spring stiffness and damping coefficient in the normal and tangential direction are chosen to be identical. Specifically, η and k are adjusted to obtain a certain restitution coefficient and to realize a predefined dimensionless shear rate $\dot{\gamma}$. For more information on the used parameter ranges and routines to calculate, e.g., the corresponding effective Young's modulus, the reader is referred to Section 4.4 and Appendix A.

4.2.2 Transport within a Particle

For modelling the thermal transport inside the particle we use the simulation tool *ParScale* [29]. Even through *ParScale* is capable of resolving individual property profiles (e.g., a dissolved chemical species) within a variety of chemical and drying models, we only account for individual temperature profiles of each particle in the present simulations. In earlier work (Forgber et al. [26]), we showed the application of *ParScale* to an optimization problem in chemical looping combustion (CLC) and chemical looping reforming (CLR) processes regarding (i) optimal solid loadings, (ii) optimal pore sizes and (iii) Knudsen diffusion limitations. As a key result it was found, that the optimal loading level of active solid is close to the porosity of the support particle and the pores of the support particle should be filled by approx. 95% with the active solid. In reactions with a high reactivity of the solid, only 45% of the pore volume should be filled. Note, that all models used in Forgber et al. [26] are documented and available to public within the online documentation [29]. By using the Method of Lines (MoL), integrated in the *CVODE* integrator (for details see [30], Forgber et al. [27]), we are enabled to perform flexible and stable simulations, even in the presence of fast changing environmental conditions (Cohen et al. [31]). For a more detailed insight into the solution procedure, and for an overview of the

parallel coupling strategy, we refer to Forgber et al. [27] and the comprehensive online documentation [29].

The basic assumption is an assembly of solid and non-porous particles. The remaining thermal energy balance equation is (i) discretized in space and (ii) integrated in time using *ParScale*. We use a spatial discretization of each particle with a fixed radial space resolution. The differential heat balance in spherical coordinates is solved (see Eqn. (4.8)), assuming spherical symmetry (i.e., discretization is done using concentric spherical shells). Since only solid, non-porous particles are tracked, we can assume for the particle heat conductivity $\lambda_p = const$. After introducing the thermal diffusivity a, the differential heat balances read:

$$a = \frac{\lambda_p}{\rho\, c_p} \tag{4.7}$$

$$\frac{\partial\, T}{\partial\, t} = -\nabla \cdot \left(-a \frac{\partial T}{\partial r}\right) + \frac{q}{\rho\, c_p}. \tag{4.8}$$

In case of particle-particle and particle-wall contact, the resulting conductive flux (calculated based on the overlap area) is considered in Eqn. (4.8) by appropriately setting the source term q in the outermost shell of the (discretized) particle. and taken into consideration when solving the internal thermal balance. The heat transfer coefficient α defines the boundary condition for T at the particle surface. For discretization in physical space a second order central differencing scheme is used. For details of the differencing scheme, as well as results of the verification studies, the reader is again referred to Forgber et al. [27] and the official documentation which is available online [29]. The next Section outlines definitions of all thermal fluxes taken into account in our simulations, including their physical interpretation. These fluxes are computed with the simulated particle and contact information (e.g., particle positions, speed, as well as particle-particle and particle-wall overlaps), and hence present the main outcome of the simulations.

4.2.3 Thermal Fluxes

The definition of thermal fluxes in the present work matches that presented by Forgber et al. [27], Rognon et al. [23] and Mohan et al. [22]. When performing thermal DEM simulations, Rognon et al. [23] showed that the convective flux

(defined in Eqn. (4.9)) can easily exceed the conductive flux. This is especially true for high shear rates. The convective thermal flux occurs due to the movement of the particles in the simulation domain, and takes the effective mass m_{eff}, the thermal capacity c_p, the volume averaged temperature $T_{vol,avg}$ and the velocity $\mathbf{v}_i$ of each particle into account. In other words - the convective thermal transport represents the redistribution of thermal energy as a result of the particle movement caused by the applied shear in the simulation domain. Note that our simulation set-up is bounded by walls, and that the normal vector of these walls matches the direction of an applied temperature gradient. In the other directions (i.e., the shear and spanwise direction) periodic boundary conditions are applied. In earlier work (Forgber et al. [27]) the temperature gradient was enforced by different thermal regions in the simulation set-up: layers of particles were set to a specific temperature which narrowed the region available for post-processing and introduced a so-called "drift-convective" flux. Since the temperature gradient is realized through a fixed wall temperature and the full simulation domain size is used for post-processing, the convective flux can be calculated as follows:

$$\mathbf{q}^{conv} = \frac{1}{V} \sum_i m_{eff,i}\, c_{p,i}\, T_{vol,avg,i}\, \mathbf{v}_i. \tag{4.9}$$

The conductive thermal transport (Eqn. (4.10)) takes particle-particle interactions into account, as it relies on the summation over all collisions. Thereby the main influence parameters are the temperature differences between the particles and the overlapping area in which heat conduction occurs:

$$\mathbf{q}^{cond} = \frac{1}{V} \sum_C 2\, \lambda_p\, A_{co}^{1/2}\, (T_i - T_j)\, \mathbf{r}_{ij}. \tag{4.10}$$

Since non-vacuum conditions are assumed, we take the transmitted heat to the surrounding fluid into account. Note that the fluid has no influence on the particle movement since we assume the particles to have a high Stokes number (St) as discussed by Yin et al. [32]. It is therefore suitable to rely on a pure DEM method for the particle-particle interaction and FVM for the inner particle properties. As it is well known, the transferred thermal flux is calculated as a function of the heat transfer coefficient α and the temperature difference between particle temperature T_i and environment temperature $T_{f,i}$ seen by every particle:

$$q^{trans,i} = \alpha\, (T_i - T_{f,i}). \tag{4.11}$$

Since the study is aimed towards a general model, $T_{f,i}$ is chosen to be a constant value. A more detailed insight on the simulation domain and adjusted parameters is given in Sec. 4.4. An overview about equations solved and unknown particle quantities are given in Tab. (4.1) and Tab. (4.2), respectively. For the reference flux we choose the maximum conductive flux of a box fully filled with the solid material that constitutes the particles, which is hence calculated as:

$$q^{ref} = -\lambda_p \frac{\partial T}{\partial y}. \tag{4.12}$$

Thereby $\partial T/\partial y$ is the temperature gradient in the gradient direction (i.e., y-direction) and can be calculated as:

$$\frac{\partial T}{\partial y} = \frac{T_{top} - T_{bot}}{H} \tag{4.13}$$

with H representing the wall distance (i.e., the simulation domain size) and T_{top} and T_{bot} denote the temperatures of the top and bottom wall, respectively.

Reference System	Equation
Particle flow	$\frac{d\,\mathbf{x}_i}{d\,t} = \mathbf{v}_i$ $m\frac{d\,\mathbf{v}_i}{d\,t} = \sum_j (\mathbf{f}^t_{ij} + \mathbf{f}^n_{ij})$ $I_i\frac{d\,\boldsymbol{\omega}_i}{d\,t} = \sum_j \mathbf{f}^t_{ij} \times \mathbf{r}_{ij}$
Internal thermal transport	$\frac{\partial T}{\partial t} = a \cdot \left(\frac{\partial^2 T}{\partial r^2} + \frac{2}{r}\frac{\partial T}{\partial r}\right)$

Table 4.1: Covering equations for particle flow (Newtons equation of motion) and equations regarding internal thermal transport in spherical coordinates in one-dimensional form.

4.3 Dimensional Analysis

Granular rheology is an active research field, and hence the main influencing parameters on the flow have been well documented by, e.g., Mohan et al. [22],

Reference System	Unknown quantities
Particle flow	Angular velocity $\boldsymbol{\omega}_i$
	Particle velocities $\mathbf{v}_i$
	Particle positions $\mathbf{x}_i$
Internal thermal transport	Particle temperature T

Table 4.2: List of unknown simulation quantities.

Chialvo et al. [6] and our earlier work (Forgber et al. [27]). In agreement with the mentioned work, we use the following definition for a dimensionless shear rate:

$$\dot{\gamma} = \gamma \, d_p^{3/2} / \sqrt{k^n / \rho_p}. \tag{4.14}$$

A major outcome of recent simulations (Hatano et al. [7], Otsuki et al. [10], Alonso-Marroquín et al. [33]) and experiments (Nordstrom et al. [8]) are simple expressions for the contact pressure. Specifically, it is possible to collapse the scaled stress-shear rate data into curves by appropriately adjusting the critical volume fraction. Since the following scaling expressions are widely excepted in the granular rheology community, we use them as an inspiration to scale the conductive thermal flux over the dimensionless contact pressure later in the manuscript (see Section 4.4):

$$p_{QS} \sim |\phi - \phi_c|^{2/3} \tag{4.15}$$

$$p_{int} \sim |\phi - \phi_c|^{0} \tag{4.16}$$

$$p_{inert} \sim |\phi - \phi_c|^{-2}. \tag{4.17}$$

Mohan et al. [22] found the Peclet number to be the most influential parameter for heat transport in granular materials and defined:

$$Pe = \frac{(d_p/2)^2}{\lambda_p / (\rho_p \, c_p)} \, \gamma. \tag{4.18}$$

Thereby, the Peclet number relates convective and conductive heat transport within the particles in the *absence* of heat transfer to the ambient fluid. However,

in the present work an ambient fluid with thermal exchange via a fixed fluid temperature T_f and heat transfer coefficient α is assumed. Clearly, for that application, the Biot number is an additional dimensionless parameter, which is defined as:

$$Bi = \frac{\alpha\, d_p}{\lambda_p}. \tag{4.19}$$

The Biot number relates the internal to the external resistance to thermal transport. Summarizing, we expect intra-particle temperature profiles for significantly large Biot numbers. The next Section outlines the wall bounded sheared box set-up, and documents our results on how the Peclet and Biot number affects the heat fluxes through a granular material.

4.4 Wall Bounded Shear Flow

In the following Section we investigate the thermal behaviour of a wall bounded shear flow under well controlled conditions. By applying moving wall boundary condition to a semi-periodic box driven by a homogeneous shear, a combination of *LIGGGHTS* and *ParScale* (Forgber et al. [27]) can be used to study various influence parameters. Both walls are moved into opposite direction with a time-invariant velocity in the x-direction. The dimensions of the box are chosen to be $H/d_p = 15$ with a range of particle volume fractions ($\phi_p = 0.50 - 0.64$) studied. The z-direction serves as the span-wise direction, whereas in x-direction the homogeneous shear flow is driven. In y-direction we apply a temperature gradient by fixing the wall temperature at the top wall and keeping the corresponding bottom wall cold. Wide ranges of various parameters and their influence on the thermal fluxes are studied with an overview given in Tab. (4.3). To illustrate the simulation domain, Fig. 4.1 depicts the wall bounded box with periodic boundary conditions in the x- and z-direction. The y-direction is bounded by walls with the arrows indicating the counter-wise applied shear.

For all unjamming shear flow situations, the flow converges into a statistical quasi-steady state, so convective and conductive fluxes through the sheared flow can be averaged and compared. Thereby, all particles are initialized with an uniform temperature, cooled down and sheared according to the studied set of dimensionless parameters. Most important, the transition between unjammed and jammed particle beds has to be distinguished from any kind of crystallization. In order to ensure this, we investigate crystallization systematically and provide a way to determine whether the system is crystallized or not.

Table 4.3: Ranges of dimensionless parameters for wall bounded shear flow simulation.

Parameter	Min. Value	Max. Value
ϕ_p	0.5	0.64
$\dot{\gamma}$	10^{-4}	10^{-1}
Pe	10^{-2}	10^{2}
Bi	0	50
μ	0.5	fixed
e	0.9	fixed
T_f	$(T_{top} + T_{bot})/2$	fixed

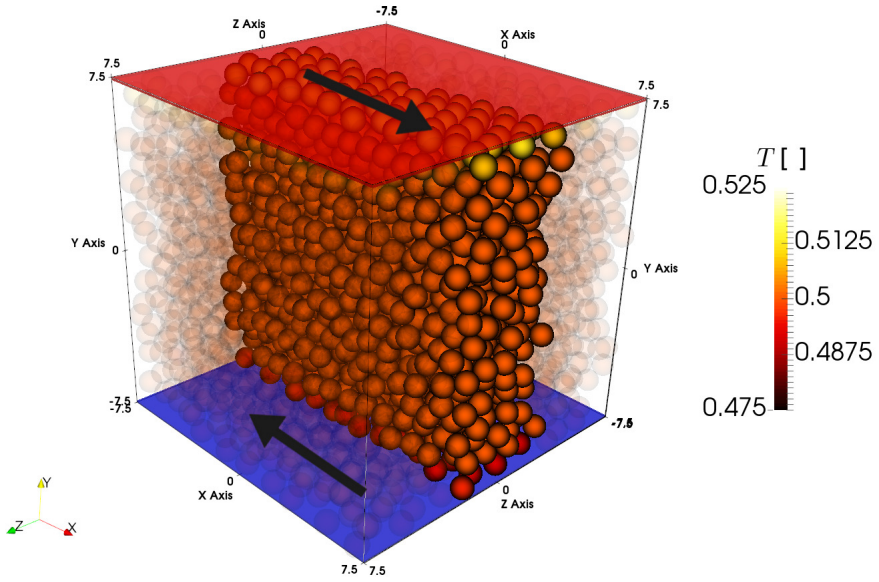

Figure 4.1: Simulation set-up for wall bounded, semi-periodic sheared box simulation. The temperature gradient points into the positive y-direction, the mean flow is in x-direction. Black arrows indicate the direction of wall movement. The transparent particles illustrate the periodic boundaries applied in the x- and z-direction. Particles are colored according to their normalized particle temperature.

4.4.1 Crystallization as a Function of the Friction Coefficient and Dimensionless Shear Rate

The goal of this Section is to adjust our simulation set-up in order to ensure physical behaviour of the sheared granular material. In contrast to our previous study (Forgber et al. [27]) which were mostly performed within a fully-periodic box, our set-up is bounded by walls. We chose this because of (i) the ampli-

fication of jamming and crystallization by walls and (ii) the gap in literature by shifting the focus to more application-near simulations that include walls. As reported frequently in the literature (Tsai et al. [34], Liu et al. [17], Luding [18]) mono-disperse particles tend to form an ordered state, which might cause crystallization. On the contrary, poly-dispersity can prevent these ordering processes. It is well known that crystallization in poly-disperse materials with a wide range of size distribution is impossible (Herminghaus [35], [36]). It is now clear that ordering within the simulation set-up should be prevented. Furthermore, walls tend to amplify crystallization, since particles cannot pass the boundary in the span-wise direction. According to recently published regime maps, a suitable way to check for this phenomena is to screen the effect of the friction coefficient and the dimensionless shear rate. Taking these regime maps into account, a higher dimensionless shear rate always result in enhanced heat transfer through conduction (Rognon et al. [23], [21], Mohan et al. [22], Forgber et al. [27]). We show that this trends are not reproducible in the case of crystallization by plotting the dimensionless conductive heat flux over the dimensionless shear rate for high particle volume fractions. Note that the dimensionless parameters chosen indicate a quasi-static regime where the contact pressure is nearly independent of the particle stiffness, resulting in a constant overlapping area and conductive heat flux.

We look at a dense granular flow to picture the transition where crystallization and jamming have been frequently reported (e.g., by Tsai et al. [34]). From Fig. 4.2 we observe a nearly constant conductive heat flux for all dimensionless shear rates in combination with high friction coefficients ($\mu > 0.5$). Taking the parameter ranges into account, we conclude that a quasi-static flow regime prevails, in which the conductive thermal transport rate, as well as the scaled contact pressure, becomes independent of the particle stiffness. Shifting focus to lower coefficient of friction (i.e., from 0.5 to 0) the dimensionless conductive heat flux drops by around seven orders of magnitude. Also, for some coefficients of friction (i.e. $\mu = 0.1$ and $\mu = 0.3$) a transition can be observed, where the dimensionless heat fluxes are dropping by two to six orders of magnitude. In that region a partially crystallized granular flow with ordering of particles originating from both walls simultaneously is observed. This has been documented based on simulations and experiments by Tsai et al. [34].

The physical reason for the observed drop in the effective heat conductivity of the particle bed is a sudden change of the average particle-particle overlap area upon crystallization: as pointed out by Luding [18], an ongoing ordering process in a granular shear flow results in a decrease of the critical particle volume fraction and a reduction of the particle-phase stress (i.e., pressure) at

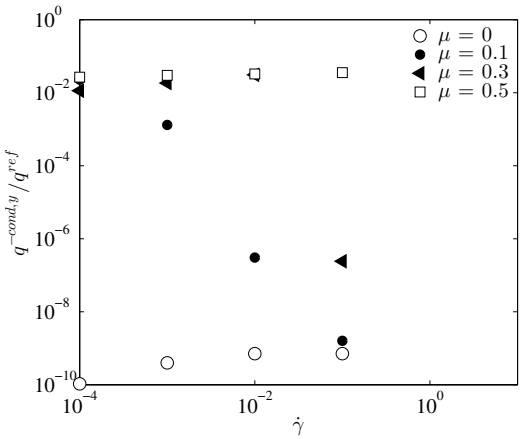

Figure 4.2: Normalized conductive heat fluxes for crystallized and non-crystallized granular materials for Pe = 0.01, $Bi = 0.1$ and $\phi_p = 0.62$.

fixed particle concentration (note, we perform fixed volume flow simulations). Consequently, the average particle-particle contact force, and hence the average overlap area are also reduced.

The time for a fully ordered system to establish is highly depending on shear rate and box size. We did not investigate this transient behaviour at this point, since we aim for the fluxes and pressures at a statistical steady state. Also, due to reproducibility of the results, we rely on a mono-sized simulation domain. Taking existing regime maps into account (see, e.g., Rognon et al. [21] , Forgber et al. [27]) a higher dimensionless shear rate result in greatly reduced heat transfer rates due to conduction. We conclude that this decrease is due to crystallization and therefore unwanted in numerical simulations. To support our conclusion of crystallization, Fig. 4.3 (a) shows the particle velocity distribution in the main flow direction for the middle layers of spheres for the two extreme cases. Note that both snapshots were produced using the same dimensionless parameters, except the coefficient of friction.

The first panel is a disordered dense particle bed where particles move and collide randomly within the shear flow. The velocity magnitudes in the main flow direction indicate a fluid-like behaviour where motion applied to the wall results in a deformation of the material. In the second panel each sphere is locked with its six neighbours and densely packed into a hexagonal array without possible movement of a single sphere. Fig. 4.3 (b) illustrates this, where most of the spheres in the domain are stagnated.

Clearly, the crystallization of granular material is an active research field and can give rise to complex side phenomena and transport effects (Herminghaus

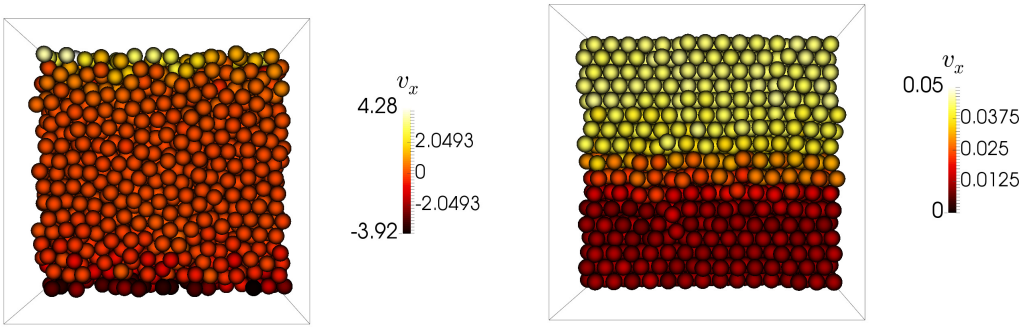

(a) (b)

Figure 4.3: Non-crystallized and crystallized granular shear flow for $Pe = 0.01, Bi = 0.1, \phi_p = 0.62, \dot{\gamma} = 0.01$ and (a) $\mu = 0.5$, as well as (b) $\mu = 0.0$. Particles are colored according to their speed in the x-direction, normalized with the reference speed $\gamma\, d_p$.

[35]). Since this is not the main focus of the manuscript, we adjust the coefficient of friction to 0.5 which ensures a non-crystallized granular shear flow. In the next Section, we study the influence of various flow situations on the conductive thermal transport.

4.4.2 Conductive Transport in Wall Bounded Shear Flow

First we look at the influence for a variety of dimensionless parameters on the conductive transport in the wall bounded flow. Fig. 4.4 shows the dimensionless conductive heat flux over the volume fraction for $Pe = 0.01$ and different dimensionless shear rates (i.e., the inverse of the particle stiffness).

Most importantly, it indicates a significant change in the conductive thermal transport through the sheared bed upon an increase of the particle concentration, for which jamming occurs. It has been frequently described in literature that the applied set of dimensionless parameters to a sheared box simulation can change the critical particle volume fraction at which jamming appears (e.g., see Ciamarra et al. [19], as well as the original jamming diagram proposed by Liu et al. [17]). We show that this transition to a jammed state is not only accompanied by strong pressure and coordination number fluctuations (Chialvo et al. [6]), but also by an enhancement in the conductive flux by up to five orders of magnitude. Thereby the amplification of the thermal flux is mainly depending on the particle stiffness. From Fig. 4.4 we want to point out that the particle stiffness has a significant influence on the jamming point. For very soft particles (compare Fig. 4.4 (a), $\dot{\gamma} = 10^{-1}$) no jump in the conductive thermal

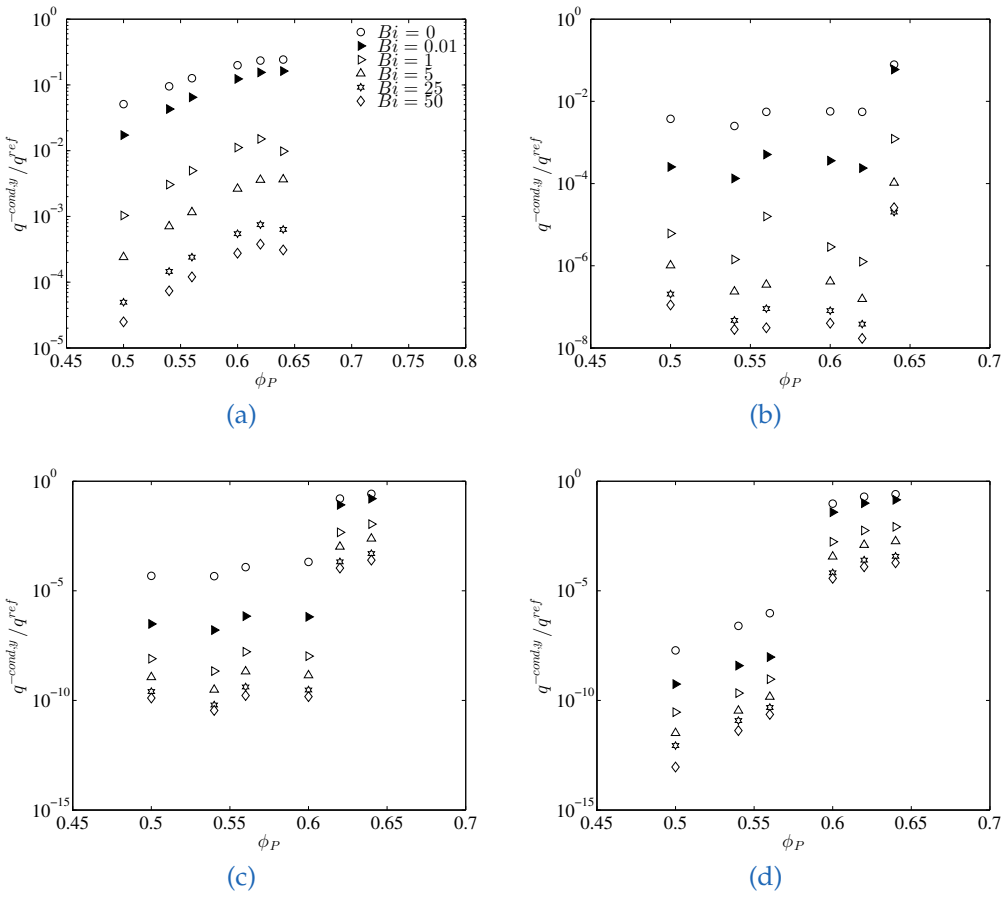

Figure 4.4: Scaled conductive flux for $Pe = 0.01$, $\mu = 0.5$, (a) $\dot{\gamma} = 10^{-1}$, (b) $\dot{\gamma} = 10^{-2}$, (c) $\dot{\gamma} = 10^{-3}$, (d) $\dot{\gamma} = 10^{-4}$.

flux can be seen and therefore our data indicates a gradual transition from an unjammed to a jammed state. As the particle stiffness is increasing (i.e., the dimensionless shear-rate is lowered) a reduction of the critical volume fraction can be seen. Fig. 4.4 (b) indicates a jammed state at $\phi_p = 0.64$, whereas in Fig. 4.4 (c) the critical particle volume fraction drops to 0.62. For the smallest studied dimensionless shear rate (Fig. 4.4 (d), $\dot{\gamma} = 10^{-4}$) the jamming volume fraction is found to be smaller than 0.6. Even though the magnitude of the scaled conductive flux varies by orders of magnitude, it can be seen from the data in Appendix B and C (Fig. 4.9 and Fig. 4.10), that the critical jamming volume fraction remains constant for different shearing speeds presented through the Peclet number. From Fig. 4.4 (b) and (c) we observe small fluctuation in the scaled conductive heat flux with rising volume fraction. According to theory, a higher volume fraction should lead to enhanced conductive transport since

more particles result in a larger contact area. To a certain extend (i.e., at high Bi numbers) these fluctuations are also present in the presence of fast shearing (see the data in Appendix B and C). Since we adjusted the coefficient of friction to 0.5, these fluctuations could be explained by the transition between shear thickening/thinning (Brown et al. [20]), or the so called "Flow and Jam" and "Slip and Jam" regimes (Ciamarra et al. [19]). Both works indicate regime changes and large pressure fluctuations around the considered volume fraction, which is directly related to the contact area between the particles, and therefore to the conductive thermal flux (compare Eqn. (4.10)). Taking these findings and previous work on collapsing pressure, stress and shear rate curves into account, we now try to find a relation between dimensionless conductive flux and scaled contact pressure.

4.4.3 Collapsed Conductive Flux over Contact Pressure

By following the previous work of Rognon et al. [21], Chialvo et al. [6] and Olsson et al. [37] we show a way to predict the conductive flux in sheared beds in which heat is also transmitted to the environment. In detail, it is shown that the conductive flux can be collapsed into a single curve, independent of any specific flow configuration or jamming, by plotting it against the dimensionless contact pressure.

In fact, Fig. 4.5 shows a diagram similar to Rognon et al. [21] for the scaling of eigenconductivities as a function of the solid fraction, coordination number and eigenstresses. We found the exponent m to be 0.82 which results in a reasonable fit of all data. Note that this plot collapses all data ranges mentioned in Tab. (4.3). The jump in the conductive flux due to jamming is not seen here since the dimensionless contact pressure is enhanced by the same order of magnitude. Our data also indicates an nearly independent behaviour of the Peclet number (compare Fig. 4.4, 4.9, 4.10) and the dimensionless shear rate. The scattering of the data is within the fluctuations of the conductive heat flux which allows us to find the following fitting functions:

$$Bi^m \frac{q^{-cond,y}}{q^{ref}} \sim 0.010\, p_{co} \frac{d_p}{k^n}, \quad \text{unjammed regimes} \tag{4.20}$$

$$Bi^m \frac{q^{-cond,y}}{q^{ref}} \sim 0.314\, p_{co} \frac{d_p}{k^n}, \quad \text{jammed regimes} \tag{4.21}$$

Due to the large variety in data (10 orders of magnitude) a single fitting function does not cover all data with sufficient accuracy. We split the data in two regimes

regarding unjammed (compare Fig. 4.6 (a), including the transition regime mentioned in Sec. 4.4.2), and jammed (compare Fig. 4.6 (b)) states. For both regimes, linear relationships are found which describe the increase of the conductive thermal flux, accounting for the transmitted heat to the ambient fluid (since we scale with Bi) over the dimensionless contact pressure.

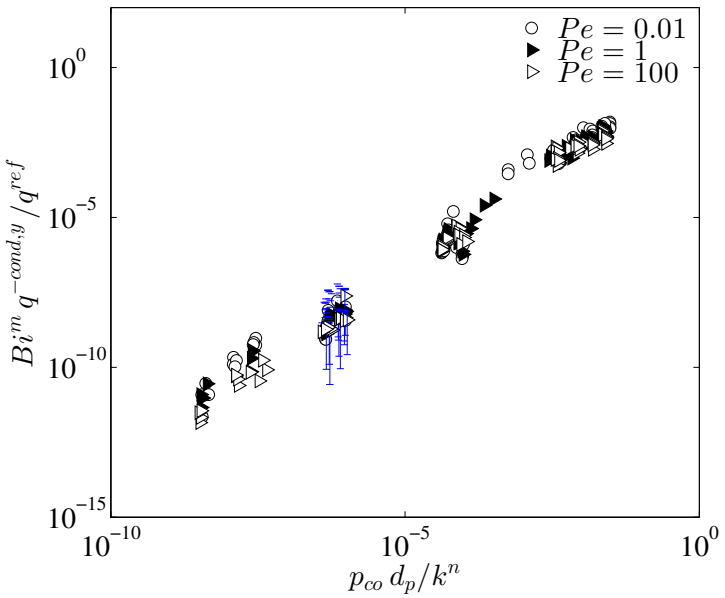

Figure 4.5: Collapsed dimensionless conductive flux over dimensionless contact pressure (with $m = 0.82$), as well as error bars that illustrate fluctuations of the data in the transition regime.

This is motivated by the fact that Rognon et al. [21] previously established a scaling of the (effective) eigenconductivities as a function of the solid fraction, coordination number and eigenstresses for dense quasi-static flows. We note in passing that Rognon et al.'s eigenconductivities have the same meaning as the dimensionless heat fluxes, since the latter are made dimensionless with a reference heat flux that accounts for the temperature gradient (see Eqn. (4.12)). Most important, Rognon et al.'s work revealed that the effective conductivities are proportional to the cube root of the compressive stress for a Hertzian contact force model. As anticipated by Rognon et al. [21], this scaling cannot be expected to hold for other contact models (i.e., the linear spring-dashpot model used by us). In addition, we consider a particle system that is cooled by an ambient fluid, and hence the stress-heat conduction scaling is different from the previously proposed cube-root scaling as shown in Fig. 5. Our data suggests that a linear scaling of a Biot-number scaled normalized heat flux with a dimensionless stress (i.e., the contact pressure) is more appropriate. Specifically, we find the

exponent m of the Biot number to be 0.82 which results in a reasonable fit of all data (see Fig. 4.5). Note that this plot collapse all data ranges mentioned in Tab. (4.3), and spans a much wider range of stresses than that considered in Rognon et al. Besides the fitting function, Fig. 4.6 includes bounds which represent the typical fluctuations of the conductive flux during shearing. The standard deviation is found to be $\sim 25\%$, averaged over all shown data. This is mainly caused by high variability in the regime transition, similar to the pressure fluctuations, identified by Chialvo et al. [6]. For these situations, we also show typical fluctuations in the heat flux in Fig. 4.5. Furthermore, especially in fast sheared granular materials (see Fig. 4.6 for $Pe = 100$) in combination with low packing fractions and high Biot numbers, the data differs from the fitting function (Fig. 4.6 (a)).

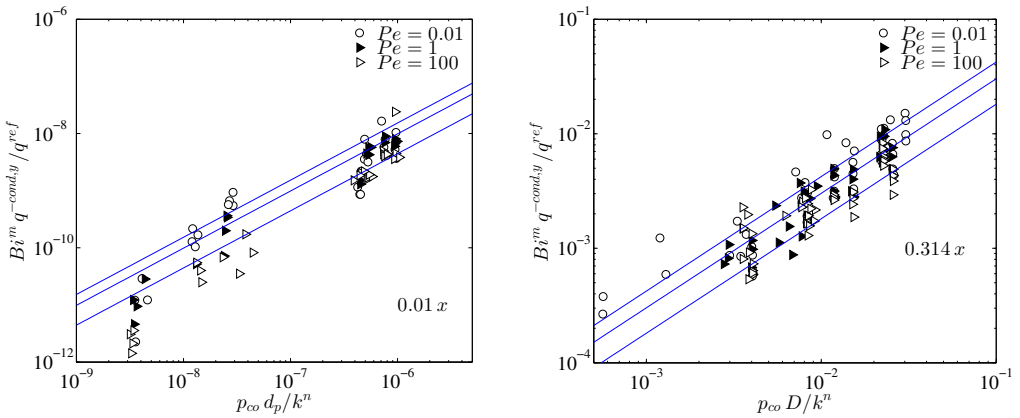

Figure 4.6: Collapsed dimensionless conductive flux over dimensionless contact pressure for $m = 0.82$ and (a) unjammed (b) jammed granular material. Blue lines indicate upper and lower limits for the averaged fluctuations calculated for the shown data ranges.

For regimes where the dimensionless conductive transport is high, the correlation shows good agreement with the simulation data. Occurring differences are well inside typical fluctuations for most of the data. Nevertheless, the model should only be taken as a coarse approach to determine the conductive heat flux. Due to the large range of relevant dimensionless parameters studied, we anticipate that it can be widely applied to sheared beds, even in jammed states. After analyzing the conductive heat transport through the granular bed, we now study the convective transport.

4.4.4 Convective Flux over Peclet Number

The convective heat transport mechanism is not directly related to material properties as it is mainly a function of the grain temperature and the particle velocity (see Eqn. (4.9)). The latter is represented by the Peclet number (i.e., a metric for the speed of shearing). Therefore, we investigate the influence of the Peclet number on the convective flux and present the results in Fig. 4.7.

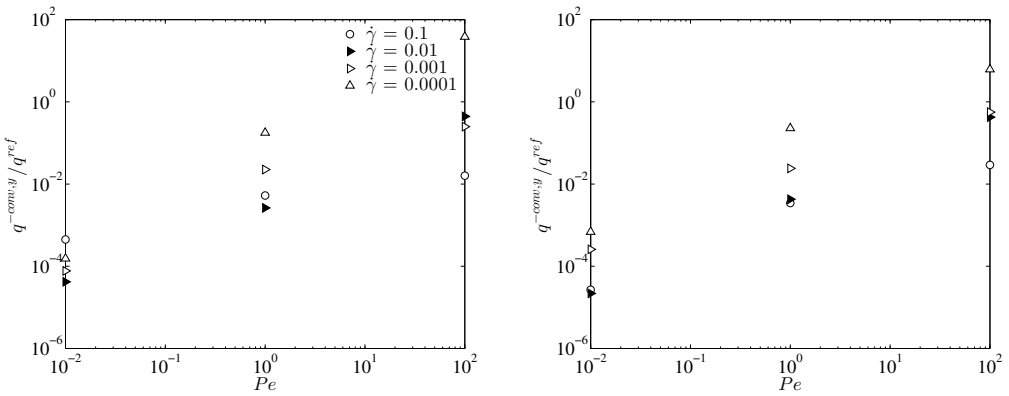

Figure 4.7: Scaled convective flux for several dimensionless shear rates and Biot numbers for $\phi_p = 0.64$, (a) $Bi = 0$, (b) $Bi = 1$.

For both Biot numbers we observe a similar behaviour as seen by Rognon et al. [23]: the convective heat flux easily exceeds the conductive heat transport rate for fast sheared beds. This is possible since the reference heat flux is defined as the heat transferred by conduction if the simulation box would be completely filled with solid (stagnant) material. In general, we agree with the findings of Rognon et al. [23] in terms of the influence of the particle stiffness. Is is shown, that stiffer particles cause an enhanced convective transport, especially for high Peclet numbers. When shifting the focus to low Pelcet numbers, the convective transport of soft particles might exceed that of the stiffer ones, which is also in good agreement with Rognon et al. [23]. This previous study found the correlation $q^{conv,y} = 10^{-2}\, q\, \tau$, which holds for sufficiently large thermal numbers τ. Furthermore, no drastic change of the convective flux is observed, as illustrated in Fig. 4.7. This is in contrast to the observed jump in the conductive thermal transport rate when transitioning from the unjammed to the jammed state. Our findings from Section 4.4.2 indicate that the jump is independent of the Peclet number, and the main dependency is with respect to the critical volume fraction and dimensionless shear rate. To prove the theory that the

convective flux is not affected by jamming of granular material a trend for different volume fractions is needed.

4.4.5 Convective Flux over Particle Concentration

In order to provide a meaningful comparison to the conductive flux enhancement in case of particle jamming (compare Fig. 4.4), we considered the convective thermal transport for different packing fractions. Note that for the conductive heat flux, a jump by up to five orders of magnitude was observed, nearly independent of the Peclet and Biot number.

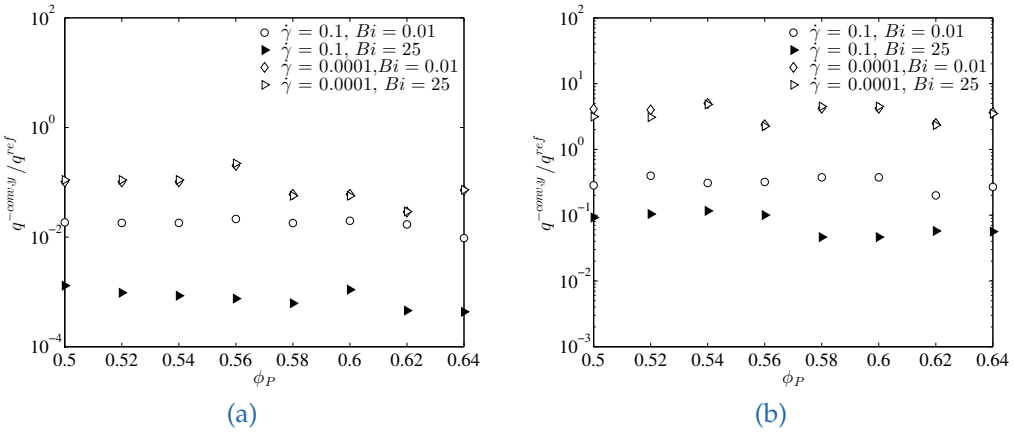

Figure 4.8: Scaled convective flux versus volume fraction for four extreme cases regarding dimensionless shear rate and Biot number (a) $Pe = 1$, (b) $Pe = 100$.

Fig. 4.8 illustrates a weak dependency of the convective flux on the particle concentration, and jamming does not lead ot a substantial change in this trend. This is true for all Peclet numbers and dimensionless shear rates studied. Even though, Fig. 4.8 only shows extreme cases regarding Biot number and dimensionless shear rate, we observe that the convective thermal transport remains nearly constant over the volume fraction. For stiff particles (e.g. $\dot{\gamma} = 10^{-4}$) the convective transport becomes independent of the Biot number as data points for $Bi = 0.01$ and $Bi = 25$ collapse. The independence is also true for $Pe = 100$ (Fig. 4.8 (b)). In other words - the transferred heat has a negligible influence on the amount of redistributed thermal heat due to the movement of the particles. When shifting our focus to softer materials ($\dot{\gamma} = 0.1$) the independence is not present anymore,since for both Peclet numbers a consequently higher convective transport is achieved for lower Biot numbers.

The difference is quite small for fast shearing ($Pe = 100$), but increases up to two orders of magnitude for slow shearing ($Pe = 1$). We conclude that for stiff particles the convective thermal transport becomes mainly a function of the particle velocity since a minor dependency on the Biot number is observed. It is clear, that higher particle velocities are seen for stiffer particle suspensions since a higher contact pressure is achieved if particles are colliding.

4.5 Conclusions

In the present work we investigated different thermal transport mechanisms in a wall bounded sheared bed filled with mono-sized spheres. Thereby, we couple the library *ParScale* to an existing DEM solver (*LIGGGHTS*) in order to resolve particle-internal temperature profiles. In our Discrete Element Method approach, we take (i) conductive (ii) convective and (iii) transferred heat to an ambient fluid into account. Again, we want to point out, that we have not solved any equation for the fluid phase since the coupling is realized through a fixed fluid temperature and a predefined heat transfer coefficient to realize defined cooling conditions. We then ensure that our system is not affected by any kind of ordering mechanism (i.e., crystallization), which is enhanced by the presence of walls. We present a new way of determining whether an ordering occurs or not by considering the behaviour of the conductive heat transfer rate as a function of the shear rate. We come to the conclusion that systems of mono-sized spheres reach the ordering state later in case of higher friction coefficients, consequently adjust the coefficient of friction to 0.5 in our set-up to prevent crystallization. In the following we show a conductive flux enhancement up to five orders of magnitude in case of jamming, which is due to the strong increase of the contact pressure upon an increase of the particle concentration.

Furthermore, our result show that the critical volume fraction is independent of the Peclet number (i.e., the speed of shearing). We assume the increase of heat flux to be originating from the increase of the contact pressure. While the identified linear scaling of normalized heat flux and dimensionless contact pressure holds over an extremely wide range of stresses, if the linear spring-dashpot model is used, Rognon et al. [23] mentioned the crucial role of the contact force model when computing the particle-particle (and particle-wall) contact area. Thus, the results of the present study should be treated with care in case other contact force models are considered. The same applies, in case a weak cooling by the ambient fluid is assumed. Inspired by the work of Rognon et al. [23] and Chialvo et al. [6], we identify scaling laws for the conductive heat flux and a possible collapse over the dimensionless contact pressure. We distinguish between jammed and unjammed regions, and present simple correlations for both cases. Also, the scaling law accounts for the transferred heat to the ambient fluid. When shifting our focus to the convective thermal transport, no direct relationship between thermal flux and critical volume fraction can be observed. The convective thermal transport rate remains mostly constant for different packing fractions. By varying the Biot number we point out that the transferred heat to the fluid has no influence on the convective flux in case of stiff particles.

We conclude that in this case the convective flux is mainly a function of the speed of shearing as the data collapse into one point. In case of softer materials a clear dependence is seen, and the transferred heat to the ambient fluid cannot be neglected anymore. This is indicated by a clear dependence of the convective heat flux, i.e., a variation up to two orders of magnitude, on the Biot number. Evaluated over the Peclet number, the convective thermal transport can easily exceed the conductive thermal transport rate, independently of the particle volume fraction and the Biot number. We find, in agreement with Rognon et al. [23], that the convective flux benefits from the presence of stiff particles since it is significantly higher. Also, the data agrees with the scaling law proposed by Rognon et al. [23], which showed that $q^{conv,y} \sim 10^{-2}\, q\, \tau$, where τ represents a thermal number similar to our Peclet number.

Future studies should focus on more detailed investigations of the effect of the transferred heat flux on the convective flux. The latter appears to be the leading heat transfer mechanism in fast sheared granular beds, and hence should be modelled in greater detail. Also, the present study was not concerned with heat transfer from the walls to the ambient fluid.

4.6 Nomenclature

4.6.1 Latin Characters

Variable	Unit	Meaning
a	$\mathrm{m^2\,s^{-1}}$	Thermal diffusivity
A	$\mathrm{m^2}$	Cross sectional area
Bi		Biot number
c	$\mathrm{J\,kg^{-1}\,K^{-1}}$	Heat capacity
C		Number of contacts
d	m	Diameter
e		Coefficient of restitution
$\mathbf{f}$	N	Force on particle
H	m	Height of simulation domain
I	N s	Moment of inertia
k	$\mathrm{N\,m^{-1}}$	Spring stiffness
m	kg	Mass
p	Pa	Pressure
Pe		Peclet number
q	$\mathrm{W\,m^{-2}}$	Heat flux
r	m	Particle radius
$\mathbf{r}$	m	Relative distance vector
St		Stokes number
t	s	Time
T	K	Temperature
$\mathbf{v}$	$\mathrm{m\,s^{-1}}$	Particle velocity
V	$\mathrm{m^3}$	Volume
Y	$\mathrm{N\,m^{-2}}$	Young's modulus
$\mathbf{x}$	m	Particle position

4.6.2 Greek Characters

Variable	Unit	Meaning
α	$\mathrm{W\,m^{-2}\,K^{-1}}$	Heat transfer coefficient
δ	m	Overlap distance during a particle–particle contact
$\dot{\gamma}$		Dimensionless shear rate
γ	$\mathrm{s^{-1}}$	Shear rate
μ		Friction coefficient
η	$\mathrm{N\,s\,m^{-1}}$	Viscous damping coefficient
$\boldsymbol{\omega}$	$\mathrm{s^{-1}}$	Eigenfrequency of damped harmonic oscillator
θ	K	Temperature difference, Scalar Quantity
τ		Thermal number
ϕ		Particle volume fraction
λ	$\mathrm{W\,m^{-1}\,K^{-1}}$	Thermal conductivity
ρ	$\mathrm{kg\,m^{-3}}$	Density

4.6.3 Superscripts

Variable	Meaning
$conv$	Convection
$cond$	Conductive
n	Normal direction
m	Exponent for correlation
ref	Reference value
t	Tangential direction
$trans$	Transferred
x, y, z	Direction

4.6.4 Subscripts

Variable	Meaning
avg	Average Value
bot	Bottom
c	Critical Value
$char$	Characteristic value
co	Contact
eff	Effective value
f	Fluid
i, j	Particle index
int	Intermediate
$inert$	Inertial
p	Particle
QS	Quasi-static
top	Top
vol	Volumetric Value
x, y, z	Directions

4.7 Appendices

Appendix A: DEM Parameters and Calculation Routines

Table 4.4: Adjusted DEM parameters.

$\dot{\gamma}$	Y_{eff}	$\triangle t$
10^{-1}	$1.32 \cdot 10^{3}$	$2.5\,10^{-3}$
10^{-2}	$4.18 \cdot 10^{5}$	$2.5\,10^{-4}$
10^{-3}	$1.32 \cdot 10^{8}$	$2.5\,10^{-5}$
10^{-4}	$4.18 \cdot 10^{10}$	$2.5\,10^{-6}$

The normal spring stiffness and the coefficient of restitution were set by adjusting the effective Young's modulus Y_{eff} and the damping coefficient η. Thus, the following equations were applied:

$$k = \frac{16}{15}\sqrt{r_{eff}}\,Y_{eff}\left(\frac{15\,m_{eff}\,v_{char}^{2}}{16\,\sqrt{r_{eff}}\,Y_{eff}}\right)^{1/5}, \tag{4.22}$$

$$Y_{eff} = \left[\frac{(\gamma/\dot{\gamma})^{2} d_p^{3} \rho_p}{(16/15)^{4/5}(r_{eff})^{2/5}(m_{eff})^{1/5}(v_{char})^{2/5}}\right]^{5/4}, and \tag{4.23}$$

$$\eta = \sqrt{\frac{4\,m_{eff}\,k}{1+\left(\frac{\pi}{\ln(e)}\right)}} \tag{4.24}$$

Note that the characteristic impact velocity v_{char} drops out of Eqn. (4.22) after inserting Eqn. (4.23) and therefore is irrelevant for the subsequent dimensional analysis. Tab. (4.4) outlines the adjusted parameter in order to obtain the dimensionless shear rate $\dot{\gamma}$.

Appendix B: Conductive Thermal Flux for other Peclet numbers

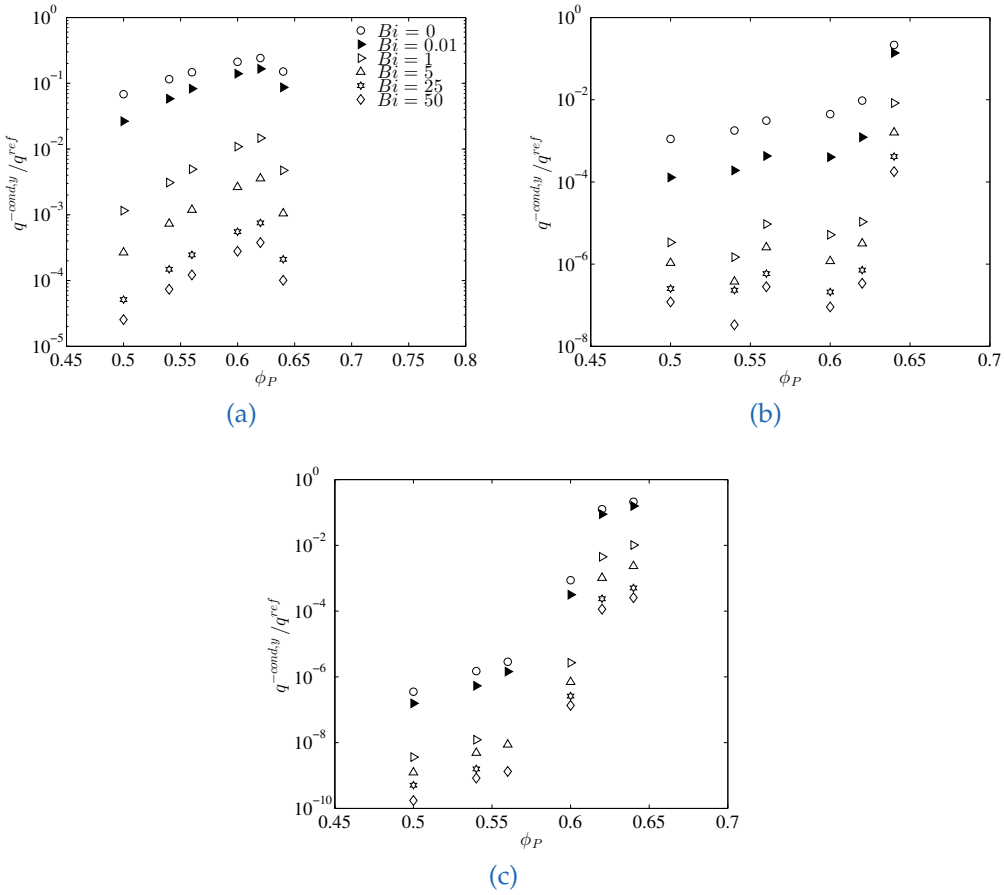

Figure 4.9: Scaled conductive flux for Pe = 1, $\mu = 0.5$, (a) $\dot{\gamma} = 10^{-1}$, (b) $\dot{\gamma} = 10^{-2}$, (c) $\dot{\gamma} = 10^{-3}$.

Fig. 4.9 and 4.10 show a wide range of flow situations and indicate a significant change in the conductive thermal transport through the sheared bed.

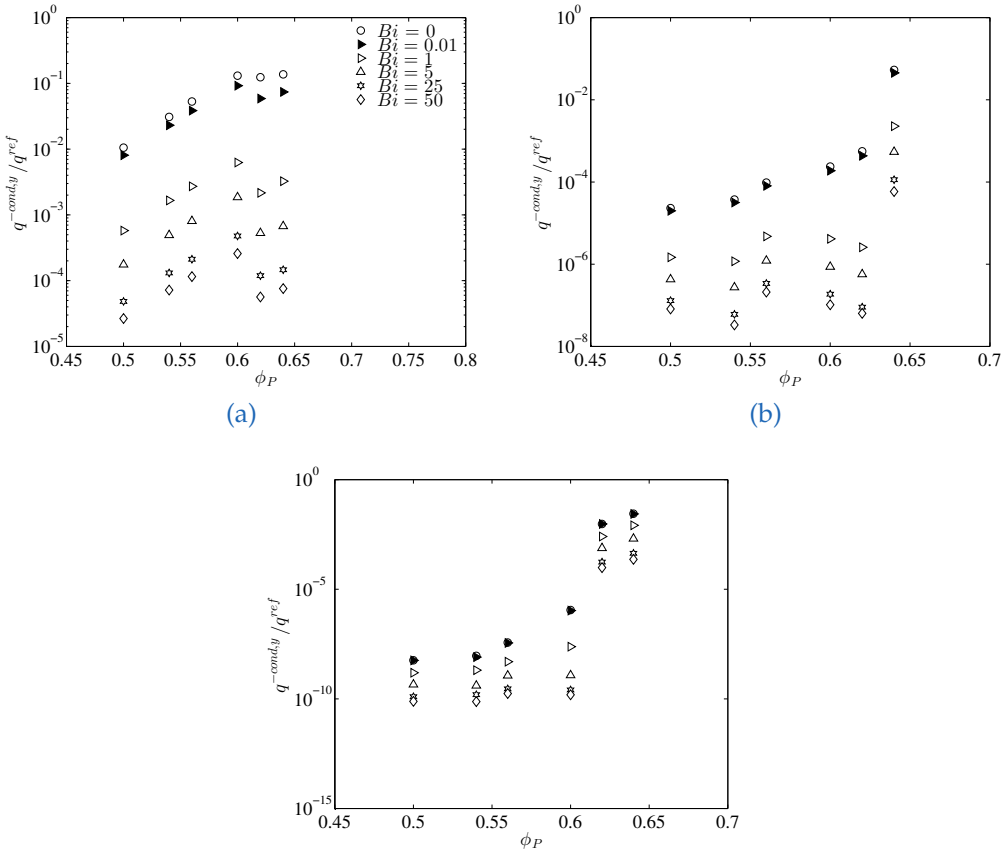

Figure 4.10: Scaled conductive flux for Pe = 100, $\mu = 0.5$, (a) $\dot{\gamma} = 10^{-1}$, (b) $\dot{\gamma} = 10^{-2}$, (c) $\dot{\gamma} = 10^{-3}$.

4.8 Bibliography

[1] T. Forgber and S. Radl. Heat transfer rates in wall bounded shear flows near the jamming point accompanied by fluid-particle heat exchange. *Powder Technology*, 315:182 – 193, 2017.

[2] V. Garzó and J. W. Dufty. Dense fluid transport for inelastic hard spheres. *Phys. Rev. E*, 59:5895–5911, 1999.

[3] C. Lun, S. Savage, D. J. Jeffrey, and N. Chepurniy. Kinetic theories for granular flow: inelastic particles in couette flow and slightly inelastic particles in a general flowfield. *J. Fluid Mech*, 140:223–256, 1984.

[4] J. T. Jenkins and M. W. Richman. Kinetic theory for plane flows of a dense gas of identical, rough, inelastic, circular disks. *Physics of Fluids*, 28(12):3485–3494, 1985.

[5] P. C. Johnson and R. Jackson. Frictional-collisional constitutive relations for granular materials, with application to plane shearing. *Journal of Fluid Mechanics*, 176:67–93, 1987.

[6] S. Chialvo, J. Sun, and S. Sundaresan. Bridging the rheology of granular flows in three regimes. *Physical Review E - Statistical, Nonlinear, and Soft Matter Physics*, 85:021305, 2012.

[7] T. Hatano. Scaling properties of granular rheology near the jamming transition. *Journal of the Physical Society of Japan*, 77(12):18–21, 2008.

[8] K. N. Nordstrom, E. Verneuil, P. E. Arratia, Z. Zhang, G. Yodh, J. P. Gollub, and D. J. Durian. Microfluidic rheology of soft colloids above and below jamming. *Physical Review Letters*, 105:175701, 2010.

[9] J. R. Seth, M. Cloitre, and R. T. Bonnecaze. Influence of short-range forces on wall-slip in microgel pastes. *Journal of Rheology (1978-present)*, 52(5):1241–1268, 2008.

[10] M. Otsuki and H. Hayakawa. Critical behaviors of sheared frictionless granular materials near the jamming transition. *Physical Review E - Statistical, Nonlinear, and Soft Matter Physics*, 80:011308, 2009.

[11] K. Otsuki. Fluidization and melting of fault gouge during seismic slip: Identification in the Nojima fault zone and implications for focal earthquake mechanisms. *Journal of Geophysical Research*, 108(B4), 2003.

[12] H. W. Zhang, Q. Zhou, H. L. Xing, and H. Muhlhaus. A DEM study on the effective thermal conductivity of granular assemblies. *Powder Technology*, 205(1-3):172–183, 2011.

[13] C. Song, P. Wang, and H. Makse. A phase diagram for jammed matter. *Nature*, 453(7195):629–632, 2008.

[14] T. S. Majmudar, M. Sperl, S. Luding, and R. P. Behringer. Jamming transition in granular systems. *Phys. Rev. Lett.*, 98:058001, 2007.

[15] B. P. Tighe, E. Woldhuis, J. J. C. Remmers, W. van Saarloos, and M. van Hecke. Model for the scaling of stresses and fluctuations in flows near jamming. *Phys. Rev. Lett.*, 105:088303, 2010.

[16] D. Vescovi and S. Luding. Merging fluid and solid granular behavior. *Soft Matter*, 12:8616–8628, 2016.

[17] A. J. Liu and S. R. Nagel. Nonlinear dynamics: Jamming is not just cool any more. *Nature*, 396(6706):21–22, 1998.

[18] S. Luding. Granular matter: So much for the jamming point. *Nat Phys*, 12(6):531–532, 2016.

[19] M. P. Ciamarra, R. Pastore, M. Nicodemi, and A. Coniglio. Jamming phase diagram for frictional particles. *Phys. Rev. E*, 84:041308, 2011.

[20] E. Brown and H. M. Jaeger. Dynamic jamming point for shear thickening suspensions. *Phys. Rev. Lett.*, 103:086001, 2009.

[21] P. Rognon, I. Einav, J. Bonivin, and T. Miller. A scaling law for heat conductivity in sheared granular materials. *EPL (Europhysics Letters)*, 89(5):1–6, 2010.

[22] B. Mohan, C. Kloss, J. Khinast, and S. Radl. Regimes of Liquid Transport through Sheared Beds of Inertial Smooth Particles. *Powder Technology*, 264:377–395, 2014.

[23] P. Rognon and I. Einav. Thermal transients and convective particle motion in dense granular materials. *Phys. Rev. Lett.*, 105:218301, 2010.

[24] A. W. Lees and S. F. Edwards. The computer study of transport processes under extreme conditions. *Journal of Physics C: Solid State Physics*, 5:1920–1921, 1972.

[25] S. Radl, T. Forgber, A. Aigner, and C. Kloss. ParScale - An Open-Source Library for the Simulation of Intra-Particle Heat and Mass Transport Processes in Coupled Simulations. *IV International Conference on Particle-based Methods – Fundamentals and Applications (PARTICLES 2015)*, pages 46–55, 2015.

[26] T. Forgber, J. R. Tolchard, A. Zaabout, P. I. Dahl, and S. Radl. Optimal Particle Parameters for CLC and CLR Processes - Predictions by Intra-Particle Transport Models and Experimental Validation. *IV International Conference on Particle-based Methods – Fundamentals and Applications (PARTICLES 2015)*, pages 101–111, 2015.

[27] T. Forgber, B. Mohan, C. Kloss, and S. Radl. Heat transfer rates in sheared beds of inertial particles at high biot numbers. *Granular Matter*, 19(1):14, 2017.

[28] C. Kloss, C. Goniva, A. Hager, S. Amberger, and S. Pirker. Models , algorithms and validation for opensource DEM and CFD-DEM. *Progress in Computational Fluid Dynamics*, 12:140–152, 2012.

[29] https://github.com/CFDEMproject/ParScale-PUBLIC, accessed May 2017.

[30] http://computation.llnl.gov/projects/sundials/cvode, accessed January 2017.

[31] S. D. Cohen, A. C. Hindmarsh, and P. F. Dubois. CVODE, A Stiff/Nonstiff ODE Solver in C. *Computers in Physics*, 10:138–148, 1996.

[32] X. Yin and S. Sundaresan. Drag law for bidisperse gassolid suspensions containing equally sized spheres. *nd. Eng. Chem. Res.*, 48:227–241, 2009.

[33] F. Alonso-Marroquín, I. Vardoulakis, H. J. Herrmann, D. Weatherley, and P. Mora. Effect of rolling on dissipation in fault gouges. *Physical Review E - Statistical, Nonlinear, and Soft Matter Physics*, 74:031306, 2006.

[34] J.-C. Tsai, G. A. Voth, and J. P. Gollub. Internal granular dynamics, shear-induced crystallization, and compaction steps. *Phys. Rev. Lett.*, 91:064301, 2003.

[35] S. Strauch and S. Herminghaus. Wet granular matter: a truly complex fluid. *Soft Matter*, 8(32):8271–8280, 2012.

[36] S. Herminghaus. *Wet Granular Matter: A Truly Complex Fluid*. Series in soft condensed matter. World Scientific, 2013.

[37] P. Olsson and S. Teitel. Critical scaling of shear viscosity at the jamming transition. *Physical Review Letters*, 99(17):1–4, 2007.

5 A novel Approach to Calculate Radiative Thermal Exchange in Coupled Particle Simulations[1]

5.1 Introduction

Radiative thermal heat exchange in particulate systems is of major importance in a variety of industrial applications, ranging from chemical reactors, thermal insulation, powder metallurgy, solar-thermal receivers, laser sintering, combustion processes and many other domains. Various experimental studies (see i.e. Chen et al. [2], Baillis et al. [3], Glicksman et al. [4], Goshayeshi et al. [5]) outline, that thermal transport through radiation becomes of outmost importance and the leading heat transfer mechanism at high temperatures, i.e., above 750°C. These temperatures are easily found in fluidized beds used for coal combustion and catalytic reactors (Tien [6]). In fact, Tien [6] provides a comprehensive review on radiation modelling in particle laden flows with focus on packed and fluidized beds. Another topic is the strong local heating: Dayal [7] pointed out that thermal radiation is of particular importance if the heat input is local, as, e.g., found in laser melting applications.

With interactions between particles and their influence on multiple length scales, radiation is an active research area. Approaches to model thermal transfer rates in particle beds are split into (i) discrete models, with focus on single particle properties, and (ii) continuum approaches, where effective properties of the bed are obtained from experiments and closed with an appropriate model (Kaviany [8]). Multiple research groups have focussed on continuum models, e.g. Chen et al. [9] who evaluated the influence of heat transfer mechanisms, including conduction and radiation, on effective packed bed properties. In analogy to that, Yagi et al. [10] calculated the effective thermal conductivity considering

[1] This Chapter is based on [1]. T.F. has fomred the model approach, implemented it into *LIGGGHTS*, used fvDOM in *OpenFOAM* for verification, set up and post-processed all simulations and has written the manuscript.

heat conduction and radiation. A number of other researchers used similar approaches (see Cheng et al. [11], Fillion et al. [12], Jagota el al. [13], Kunii et al. [14], Dixon [15]). Clearly, continuum approaches are not limited to the prior shown applications, but can also be applied to model radiation inside a single particle. More recent studies (e.g. Di Blasi [16]) outline possibilities to account for a large number of phenomena including the influence of radiation on combustion or wood conversion (Ragland et al. [17], Bryden et al. [18], Lockwood et al. [19]). In fact, continuum models are also frequently applied to study radiative transport in the fluid phase via Finite Volume Discrete Ordinate Methods (fvDOM). These methods solve the radiative transport equation (RTE) for a finite number of discrete angles. Discrete ordinate methods rely on a simultaneous evaluation of partial differential equations. Therefore, they are similar to the Navier-Stokes equation, and hence a coupling to existing finite volume codes seems natural. Continuum approaches accounting for the radiative thermal flux are also used in flame and combustion simulations including radiative turbulence influences (Bryden et al. [18], Hostikka et al. [20]).

Drawing back to particle laden flows, and according to Kaviany [8], the theory of independent scattering and adsorption of radiation (Cartigny et al. [21], Howell et al. [22]) is only valid if the gas phase volume fraction is greater than 0.95. Unfortunately, most of industrial applications, e.g., reacting particle beds, involve solid volume fractions much higher than this critical value. Furthermore, the assumption of independent scattering is weakened since the particle size is usually small. This clearly limits the application of simple stochastic models for particle-particle radiation. For high volume fractions and increasing particle diameter, emission coefficients tend to be as high as 0.7 and 1.0, as found in the experiments of Ozkaynak et al. [23]. With increasing computational resources, also DEM-based models can be applied to relatively large domain problems, simulating the trajectory of $O(10^7)$ particles simultaneously (Kloss et al. [24]). A number of methods, e.g., the Discrete Transfer Radiation Model (DTRM) as described by Toschkoff et al. [25] proved useful in connection with these DEM-based models. DTRMs track a representative number of rays from the point of origin (i.e., the emitting surface), and predict the rays' propagation through the simulation domain. With DTRM-based methods it is possible to account for all optical thicknesses, and take (isotropic) reflections into account. On the downside, with increasing number of rays, the computational time becomes ecsessively high. Clearly, ray tracing is computationally expensive if applied to a large number of moving particles. While Amberger et al. [26] already applied ray tracing in the DEM solver *LIGGGHTS*, he faced performance problems at a large number of particles.

Methods developed with the application to radiation are also used in related fields. In fact, Toschkoff et al. [25] showed the application of ray-tracing for wet tablet coating. Thereby every ray represents a fixed amount of liquid based on the injection rate and the number of rays. Zohdi [27] used ray tracing in order to rapidly simulate the effect of acoustical pulses on an agglomeration composed of a collection of discrete particles. In summary, along with Monte-Carlo approaches, discrete models have proven to be a powerful tool in combination with DEM-based simulations.

At this point we see a gap in modelling approaches that we want to close: efficient methods for predicting radiative heat transfer in DEM-based simulations of dense granular flows do not exist. In fact, we will present a discrete algorithm to account for surface radiative exchange in particle laden flows which we embed in the DEM solver *LIGGGHTS*. We generate verification cases for particle assemblies based on the continuum discrete ordinate method, compare them to analytic expressions and use that verification setup to evaluate our model implemented in *LIGGGHTS*. In fact, we take the idea to calculate view factors, as done in DTRM methods, and compute them in a fast and efficient way. We take an existing setup, i.e., a sheared particle bed that we considered already in our earlier work (Forgber et al. [28], [29]), and extend the analysis by radiative thermal transport. For further background information on sheared particle beds, the reader is referred to the work of Forgber et al. [28], [29], Rognon et al. [30], Chiavlo et al. [31] and Mohan et al. [32] who discussed various effects and regimes of sheared granular materials in great detail.

At the beginning of our manuscript (see Section 5.2) we explain our simulation method for the verification setup and present an overview of all relevant equations solved in the continuous model, including known and unknown simulation parameters. Furthermore, we introduce a novel approach to determine view factors and calculate the radiative flux between mono-disperse particles. Also, we outline the calculations of thermal fluxes in this Section. Section 5.3 summarizes our verification studies, limiting cases and shows an application to a fixed bed at different volume fractions. In Section 5.5 we apply our novel approach to a fully periodic, sheared particle bed and evaluate the radiative flux over a wide range of dimensionless parameters. Section 5.6 summarizes the presented work and outlines ideas for further studies. Note that we included a Nomenclature (Section 5.7) at the end of our manuscript where all symbols are defined.

5.2 Radiation Modelling

To predict the radiative thermal fluxes in particle laden flows, the energy exchange rate between all relevant surface elements of the involved particles has to be determined. Thereby, the energy exchange of two surface elements is, next to the temperatures, a function of their surface distance, their relative orientation, and individual size. All these geometrical factors can be described with a single variable, which is called the view factor in our present contribution. In literature, this factor is also referred to as diffuse view factor, configuration factor, angle factor or shape factor. The surface radiation transport approach relies on the assumption of a non-participating media in between exchanging elements. This is valid for vacuum conditions, as well as most of di- and mono-atomic gases (including air) at moderate temperatures. The principally occurring radiation processes are shown in Fig. 5.1. While transmitted radiation can typically be neglected for most industrial applications, absorption and reflection need to be accounted for. Especially reflection remains a delicate phenomena to balance for the entire enclosure. Fig. 5.2 shows a general enclosure where all visible parts contribute energy towards the enclosed surface (i.e., the particle). This makes radiative thermal transfer in a fluid-particle suspension a long distance interaction, especially if the ambient fluid is treated as a "gray media". Thus, photons are allowed to travel freely through the fluid without having interactions with the molecules that constitute the fluid. Consequently, the entire enclosure of the system of interest needs to be accounted for. This is in contrast to other thermal transport phenomena such as conduction or thermal transfer to an ambient fluid which can be described on a particle or contact level.

In order to limit the complexity of our surface radiation model to a manageable extent, some assumptions on relevant surface properties are made. A key simplification arises if all surfaces are treated as black, i.e., reflected thermal radiation is not accounted for. We will adopt this simplification for the bulk of our simulations. Furthermore, radiation leaving the point of origin is assumed to be diffusive, i.e., the intensity of radiation is independent of the wave length. Finally, accounting for an enclosure constituted of complex surfaces is often done by introducing a sufficiently large number of isothermal flat surfaces (e.g., triangles) as illustrated in Fig. 5.2.

Coming back to the view factor between two surface elements dA_i and dA_j, we

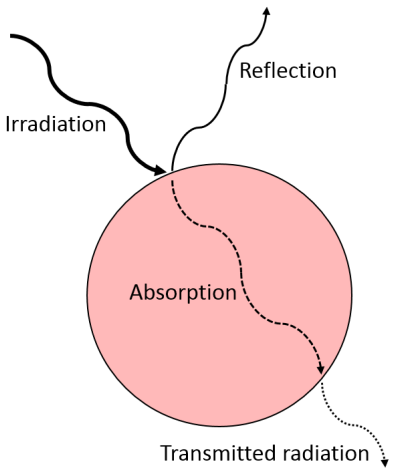

Figure 5.1: Thermal radiation mechanisms acting on a particle.

can write the formal definition as

$$d\,\varepsilon_{dA_i - dA_j} = \frac{\text{diffuse energy leaving } dA_i \text{ directed to and intercepted by } dA_j}{\text{total diffuse enery leaving } dA_i} \tag{5.1}$$

where directed refers to a direct path without any interference or reflections. If the independence of the radiative intensity due to emission and reflection with respect to the spatial direction is assumed, the view factor between two areas of infinitesimally small size can be calculated as

$$d\varepsilon_{dA_i - dA_j} = \frac{\cos\omega_i \cos\omega_j}{\pi\, S^2} dA_j \tag{5.2}$$

with ω_i and ω_j being the angle between surface normals, and S being the shortest distance between the surface elements dA_i and dA_j. Due to the law of reciprocity (Modest [33]) it can be shown that

$$A_j d\varepsilon_{A_i - dA_j} = dA_i \varepsilon_{dA_i - A_j}. \tag{5.3}$$

Considering dense fluid-particle suspensions, accounting for the entire enclosure of the particle arrangement when calculating the view factor matrix for every surface element pair between two particles is extremely computationally demanding. Thus, only the usage of statistical methods allows computations in a feasible timeframe. In detail, Monte Carlo methods have been applied

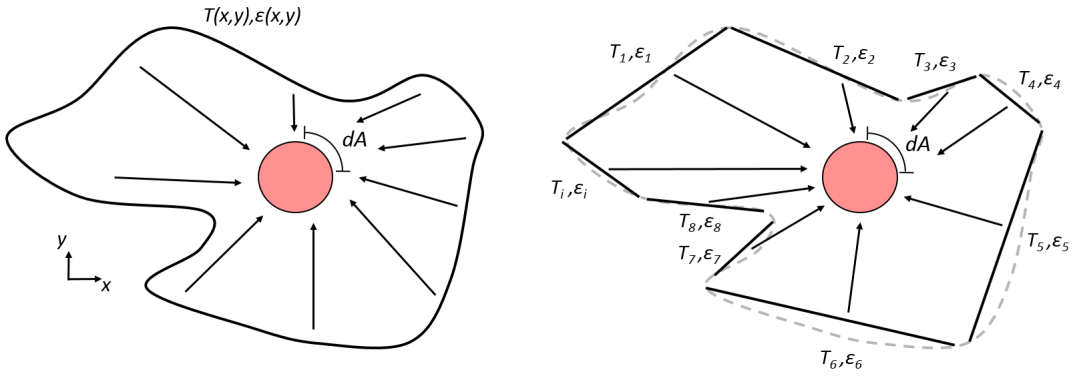

Figure 5.2: Enclosed volume around a single sphere represented by a finite number of simplified surfaces.

to thermal transport by Howell et al. [22]. Also, the application of simplified radiation models to fixed bed reactors has been demonstrated, in which the view factors were calculated once and stored. Since these previous studies refer to static particle systems, updates of the radiative exchange terms only have to be performed in cases of temperature changes. Due to their considerable large computational overhead, Monte Carlo methods (see Hammersley and Handscomb [34] or Hajji-Sheikh [35] for details) are thus not applicable to moving particle systems where view factors have to be updated frequently.

A second way to determine exchange rates due to thermal radiation is ray tracing. This is a discrete method where a representative number of rays, which represent the trajectories of photons, are emitted from the particle surface and tracked throughout the system. Thereby, it is possible to account for reflection, absorption and scattering in a natural way, though this is computationally expensive. Amberger et al. [26] demonstrated using a ray tracing algorithm which was implemented in the DEM solver *LIGGGHTS*. Also Dayal [7] showed an application of ray tracing algorithms and amplified the specific need in case the thermal input to a bed of particles is local, e.g., as this is the case in laser melting applications.

A third way to calculate the radiative flux in fixed particle assemblies is based on the finite volume Discrete Ordinate Method (fvDOM). This method relies a continuum-based approach to describe the propagation of photos and the associated radiative energy flux between particles. In particular, we make use of the implementation of the fvDOM in the tool *OpenFOAM* in our present work. Specifically, our idea is to use fvDOM to supply data that is used in a second step to build and verify a simple view factor model. An overview of the governing equations of the fvDOM is given in the next Section.

5.2.1 Method of Discrete Ordinates - S_N Approximations

The method of discrete ordinates (also refereed to as S_N-methods) has firstly been applied to problems in neutron transport theory by Lee [36], and later to planar thermal radiation problems by Love et al. [37] [38], Hottel et al. [39], Roux and Smith [40], as well as Mishra and Prasad [41]. In the last 30 years, it was mainly due to the work of Fiveland [42] and Truelove [43] who applied the discrete ordinates method to general heat transfer problems involving radiation. The method itself allows us to transform a transfer equation (i.e., the RTE-equation) into a set of partial differential equations that need to be solved simultaneously. The resulting discrete directions open a total solid angle of 4π in space. The integral over that angle is approximated by a numerical quadrature method to allow the evaluation of the radiative heat flux, or a radiative source term. Since the combination of FVM and DOM is a wide and active research area, a detailed discussion of the capabilities and shortcomings is far out of this manuscript's scope. The reader is referred to the comprehensive and most complete recent reviews of Coelho et al. [44] and Charest et al. [45]. The general equation of transfer for an an-isotropically scattering, emitting and absorbing medium is

$$\frac{\mathrm{d}t}{\mathrm{d}s} = \hat{\boldsymbol{s}} \cdot \boldsymbol{\nabla} \boldsymbol{I}(\boldsymbol{r}, \hat{\boldsymbol{s}}) = \kappa(\boldsymbol{r}) I_b(\boldsymbol{r}) - \beta(\boldsymbol{r}) I(\boldsymbol{r}, \hat{\boldsymbol{s}}) + \frac{\sigma_s(\boldsymbol{r})}{4\pi} \int_{4\pi} I(\boldsymbol{r}, \hat{\boldsymbol{s}}') \Phi(\boldsymbol{r}, \hat{\boldsymbol{s}}', \hat{\boldsymbol{s}}) \, \mathrm{d}\Omega'. \tag{5.4}$$

As outlined before, Eqn. (5.4) is solved for an discrete set of n directions $\hat{\boldsymbol{s}}_{\boldsymbol{i}}$ for $i = 1, 2, ..., n$ and corresponding directional weights ω_i using

$$\int_{4\pi} f(\hat{\boldsymbol{s}}) \, \mathrm{d}\Omega = \sum_{i=1}^{n} \omega_i f(\hat{\boldsymbol{s}}_{\boldsymbol{i}}). \tag{5.5}$$

Drawing back to the enclosed surface, two interactions must be accounted for where the beam is (i) emanated from the wall ($\hat{\boldsymbol{n}} \cdot \hat{\boldsymbol{s}}_{\boldsymbol{i}} > 0$) and (ii) reflected or absorbed by the wall ($\hat{\boldsymbol{n}} \cdot \hat{\boldsymbol{s}}_{\boldsymbol{i}} < 0$). The n first order differential equations are solved simultaneously by standard numerical methods for the unknown radiative intensity $I_i(\boldsymbol{r}, \hat{\boldsymbol{s}}_{\boldsymbol{i}})$. If the temperature field is unknown and scattering and surface reflections occur, the solution of the above equation necessarily involves iterations. In contrast, if the temperature field is known, combined with absence of scattering and wall reflections, the solution is straightforward. After the direction-integrated quantities are evaluated, the radiative thermal

flux inside a medium can be calculated using

$$\boldsymbol{q}(\boldsymbol{r}) = \int_{4\pi} I(\boldsymbol{r}, \widehat{\boldsymbol{s}}) \widehat{\boldsymbol{s}} \, \mathrm{d}\Omega = \sum_{i=1}^{n} \omega_i \, I_i(\boldsymbol{r}, \widehat{s}_i) \, \widehat{\boldsymbol{s}}_{\boldsymbol{i}} \tag{5.6}$$

and the corresponding incident radiation as the divergence of the radiative heat flux

$$q_{in}(r) = \int_{4\pi} I(\boldsymbol{r}, \widehat{\boldsymbol{s}}) \, \mathrm{d}\Omega = \sum_{i=1}^{n} \omega_i \, I_i(\boldsymbol{r}, \widehat{s}_i). \tag{5.7}$$

The evaluation of radiative fluxes at each surface is straightforward, and the reader is referred to Modest [33] for details. We now postulate a simple algorithm to compute view factors in a DEM-based simulation that aims on estimating the fluxes that would be calculated with a fvDOM. Our new DEM-based algorithm focusses on computational efficiency, which enables us to study moving particle systems which is not possible using fvDOM since meshing and computation times would be excessively large.

5.2.2 Discrete Inter-Particle Radiation Modelling

The basis of the algorithm presented next is the calculation of a particle-particle solid angle. In three-dimensional space, the solid angle represents the fraction of the target particle that is seen by an observer sitting at the neighbouring particle's center. Thus, the solid and can be illustrated as a cone. In other words - it is a measurement of the relative size which the target particle has, seen from the observer particle. Along with the solid angle φ, we define the two center points P_i and P_j with the corresponding radii r_i and r_j of both particles (see Fig. 5.8). Thereby, S_{i-j} is the normalized magnitude of the vector between both particle surfaces. For S_{i-j} we define

$$S_{i-j} = \frac{\overline{P_i \, P_j} - (r_i + r_j)}{r_j}. \tag{5.8}$$

Since we limit our current approach to mono-disperse spheres, we always assume

$$R = \frac{r_j}{r_i} = 1. \tag{5.9}$$

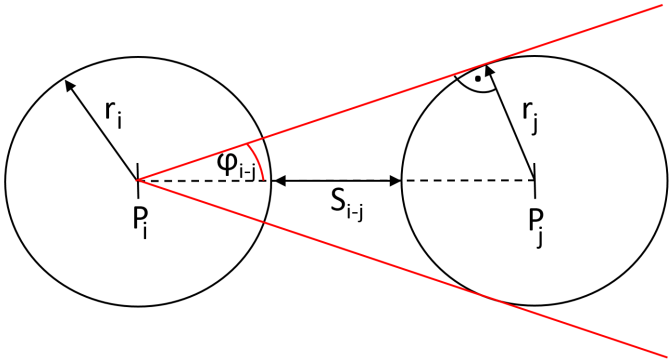

Figure 5.3: Definition of quantities for particle-particle interactions.

Next, we consider that for every particle a discrete number of points is distributed on the surface in an area-equally manner. The number of points (N_p) is defined by the user, and the area covered per point is obviously:

$$A_{equal} = \frac{4\,\pi\,r_i^2}{N_p}. \tag{5.10}$$

To determine the location of the points on the sphere, we first calculate the equidistant distance between the points:

$$d_{equal} = \sqrt{A_{equal}}. \tag{5.11}$$

With this value it is possible to obtain the rounded number of angular discretizations points:

$$M_\theta = round\left(\frac{r_i\,\pi}{d_{equal}}\right) \tag{5.12}$$

and the related distance:

$$d_\theta = \frac{r_i\,\pi}{M_\theta}. \tag{5.13}$$

The same is done for the polar coordinate:

$$d_\phi = \frac{A_{equal}}{d_{equal}}. \tag{5.14}$$

We then loop for all $m = 0...M_\theta$ and calculate θ using

$$\theta = \frac{\pi\,(m + 0.5)}{M_\theta}. \tag{5.15}$$

Similarly, for the polar discretization points we compute

$$M_\phi = round\left(\frac{2\,\pi\,r_i\,\sin\theta}{d_\phi}\right). \tag{5.16}$$

By looping over all polar discretization points $n = 0...M_\phi$, the discretization angle ϕ can be obtained by

$$\phi = \frac{2\pi n}{M_\phi}. \tag{5.17}$$

Now, for every ϕ, the position of a point on a particle can be easily calculated using

$$x_{i,p} = r_i \quad \sin\theta\cos\phi + P_{i,x} \tag{5.18}$$
$$y_{i,p} = r_i \quad \sin\theta\sin\phi + P_{i,y} \tag{5.19}$$
$$z_{i,p} = r_i \quad \cos\theta + P_{i,z} \tag{5.20}$$

with $P_{i,x}$,$P_{i,y}$ and $P_{i,z}$ being the actual particle position in the domain.

Note that the points are distributed at the beginning of a simulation, and only need to be updated within the current particle position. Thus, the above algorithm only has to be executed once. We now identify the close neighbours of each particle, making use of the built-in neighbour list algorithm of the DEM solver *LIGGGHTS*. For every neighbour, the per-particle corresponding solid angle φ is calculated by using the known particle center coordinates P_i and P_j:

$$\sin\varphi = \frac{r_j}{\overline{P_i\,P_j}}. \tag{5.21}$$

By using the solid angle between two particles we assume that every sphere is emitting radiative energy from its center of mass. In reality, however, and as done in other numerical methods (e.g., ray-tracing or Monte-Carlo methods) thermal radiation is emitted from multiple points located at the particle surface. Illustrating this in a schematic form (see Fig. 5.4) and calculating the view factor over half of the perimeter pointing to the target particle, we observe a higher

local view factor contribution inside the solid angle compared to a Monte Carlo approach. On the contrary, there is no contribution if the point is located outside the solid angle. Note that u_i is defined as:

$$u_i = \frac{u}{r_i \, \pi} \tag{5.22}$$

ranging from 0 (top of the particle) to 1 (bottom of the particle) in dimensionless units.

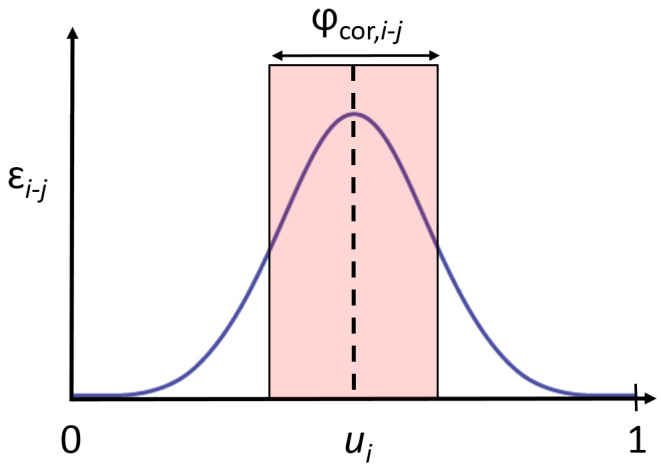

Figure 5.4: Comparison of the contribution to the view factor between a statistical method (e.g., Monte Carlo, blue line) and the proposed discrete radiation model (red rectangle).

This forces us to introduce a correction term to the calculated solid angle, which we parameterize with the dimensionless surface distance S_{i-j} of the particle pair. The correction is obtained by fitting our model to an analytical solution available in literature, e.g., that presented by Felske [46] and Jones [47]. Fig. 5.5 depicts the occurring difference in the view factor calculation, if the solid angle is not corrected. Note that Eqn. (5.26) discussed below was used to calculate ε_{i-j}. Also, we choose two different numbers of surface points (i.e., $N_p = 10,000$ and $N_p = 400$) to highlight the accuracy of the model with respect to N_p. As it can be seen, $N_p = 400$ is a sufficiently good approximation to the case with a larger number of points, except for small S_{i-j} values.

Also, Fig. 5.5 shows that especially in situations where particles are close (i.e., S_{i-j} is small), the solid angle needs to be corrected due to the mentioned reasons. Thereby, we observe errors up to 24% for $S_{i-j} = 0$ and $N_p = 400$ (the error is 12% for $N_p = 10000$). Fortunately, these errors decrease systematically with increasing distance between the particles. The resulting correction term (see

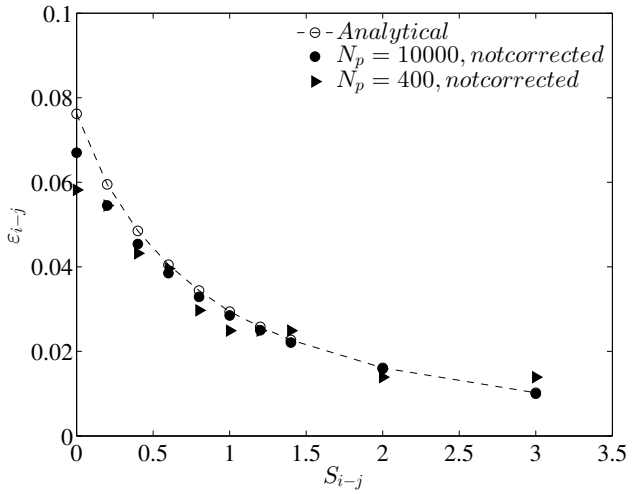

Figure 5.5: Calculated view factors in a two particle system versus the dimensionless surface distance: simplified model with non-corrected solid angle and analytical solution.

Eqn. (5.24)) is found to be well approximated by an exponential function with the parameters shown below. It is obvious that the correction must depend on the dimensionless distances of the particle surfaces (*i.e.*, S_{i-j}).

$$\begin{aligned} \varphi_{cor,i-j} &= a\, e^{b\, S_{i-j}} \quad \text{with} \\ a &= 0.03407 \\ b &= -1.965. \end{aligned} \tag{5.23}$$

The angle correction $\varphi_{cor,i-j}$ is simply added to the solid angle calculated for each particle pair, i.e., we use

$$\varphi^* = \varphi + \varphi_{cor,i-j}. \tag{5.24}$$

Using the corrected solid angle φ^*, a significant enhancement in accuracy for calculating the view factors is observed as depicted in Fig. 5.24. For a large number of points the difference is negligible, whereas for $N_p = 400$, a maximum error of 7% is observed.

We can now make use of the corrected solid angle to calculate the view factors in more complex situations where multiple particles interact with a center particle having index i. Specifically, we first need to decide which point on the surface of particle i should be considered as interacting with a neighbor particle j. Therefore, we consider the center-center vector $\overline{P_i P_j}$ and the corrected solid

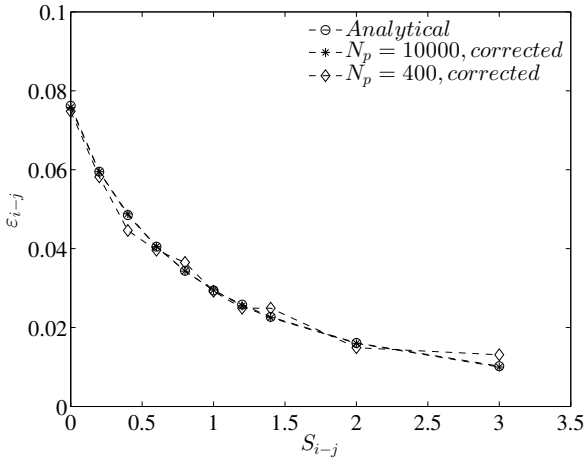

Figure 5.6: Calculated view factors in a two particle system versus the dimensionless surface distance: simplified model with corrected solid angle and analytical solution.

angle to compute a maximum permissible normal distance:

$$d_{\overline{P_iP_j}} = \sin\varphi^* \, r_i. \tag{5.25}$$

Similarly, the distance d_{center} of a point located on the particle surface to $\overline{P_iP_j}$ can be calculated in a straight-forward way. In case d_{center} is smaller than the maximum permissible normal distance $d_{\overline{P_iP_j}}$, we consider this point on particle i as interacting with particle j. In such a way we can mark all points on particle i that interact with the neighbour particle j. After all relevant points are marked on particle i, the algorithm moves to the next particle in the neighbour list which is schematically shown in Fig. 5.7. Subsequently, we apply the same algorithm to particle $j+1$ and mark points on particle i accordingly. Most important, this is allows us to identify regions that are shadowed by other particles: if a point on particle i is already marked, the distance of particle $j+1$ versus that of particle j can be used to decide whether shadowing occurs or not. Finally, the view factor considering shadowing for each particle-particle pair simply reads:

$$\varepsilon_{i-j} = \frac{N_j}{N_p}. \tag{5.26}$$

where N_j refers to the number of points on particle i that are marked with the index of particle j. Once the view factor is calculated, the heat transfer rate between two particles due to radiation can easily be calculated using (Cengel et

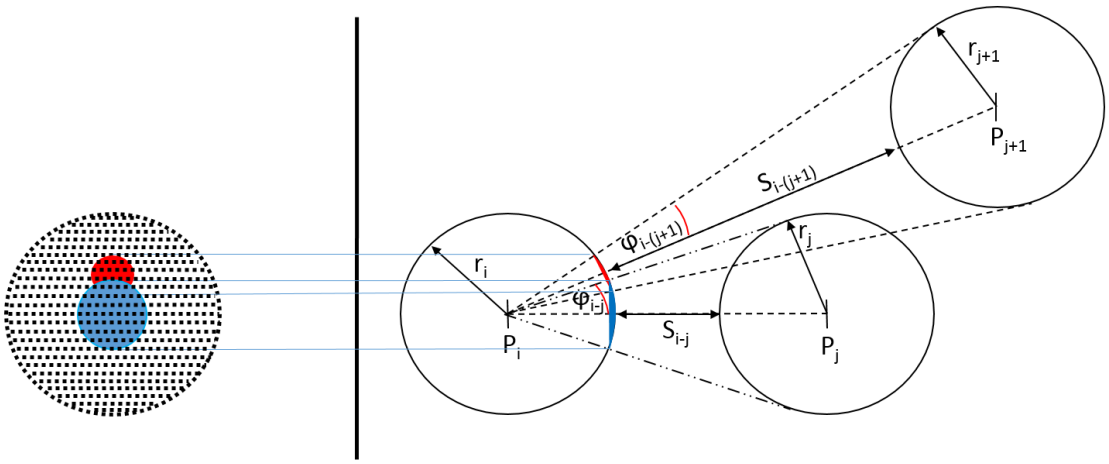

Figure 5.7: Schematic illustration of the view factor calculation algorithm in case of a three particle system in which partial shadowing occurs.

al. [48] and Chen et al. [2]):

$$Q_{i,j}^{rad} = \frac{\sigma_s (T_i^4 - T_j^4)}{\frac{1-\epsilon_i}{A_i \epsilon_i} + \frac{1-\epsilon_j}{A_j \epsilon_j} + \frac{1}{\varepsilon_{i-j} A_i}} \tag{5.27}$$

with σ_s being the Boltzmann constant ($\sim 5.67 \cdot 10^{-8}\,\mathrm{W\,m^{-2}\,K^{-4}}$), ϵ_i and ϵ_j being the emissivities of particle i and j, respectively. Note that Ozkaynak et al. [23] showed that the emissivity of most metallic surfaces operating at high temperature tends towards 0.7-1.0. From a computational point of view, recoding the view factors results in the need for allocating memory for $N_p \times N_{neigh}$ scalar values. We note in passing that it is necessary to store the information (e.g., position) of each of the N_p surface points only once globally, since transformation to each particle position is straight forward. While view factors could be calculated during each time step, recording of view factors is necessary to maximize the computational efficiency of our algorithm, especially in case reflected thermal radiation is considered. How we account for reflection is described in the following.

5.2.3 Reflected Radiation

Apart from black surfaces, the outgoing radiative intensity consists of contributions from emission and reflections as illustrated in Fig. 5.1. Hence, the reflected

part must be accounted for in our algorithm. We now show to constrain our analysis to situations where reflected thermal radiation is isotropic, i.e., reflection occurs with the same probability into all spatial directions. For every particle the incoming radiative flux can be divided into an absorbed ($\dot{q}_{j,absob}$) and a reflected fraction ($\dot{q}_{j,reflect}$) based on the emissivity of each particle (see Eqn. (5.27)). The reflected part is treated as a source term and its energy is distributed equally on the particle surface. Consequently, we lose the directional information of the reflected energy, which is a drawback compared to (computationally significantly more expensive) statistical methods (e.g. ray-tracing). Nevertheless, conservation of radiative thermal energy and consistency is retained, when performing coupled simulations, e.g., using our tool *ParScale* (see Forgber et al. [28], [49], Radl et al. [50]). Also, we assume that the speed of light (and therefore the propagation of the reflection) is much faster than the speed of the particles. This enables us to solve for emission, absorption and reflection in the same time step. Since we store the view factor matrix, solving for reflection does not introduce any significant amount of computational overhead. The radiative thermal flux from particle i to particle j is calculated using:

$$\dot{q}_{i-j} = \sigma_i \, \epsilon_i \, \varepsilon_{i-j} \, (T_i^4 - T_j^4) \tag{5.28}$$

with the absorbed energy by particle j

$$\dot{q}_{j,absob} = \epsilon_j \, \dot{q}_{i-j} \tag{5.29}$$

and the reflected fraction

$$\dot{q}_{j,reflect} = (1 - \epsilon_j) \, \dot{q}_{i-j}. \tag{5.30}$$

We want to point out, that Eqn. (5.28), (5.29) and (5.30) are valid along with Eqn. (5.27) and calculate the terms separately. For all particles j, we can now "collect" the reflected thermal energy and distribute it among all particles in the neighbour list. Specifically, we add the reflected flux

$$\dot{q}_{j-i,corr} = \dot{q}_{j-i} + \varepsilon_{j-i} \, \dot{q}_{j,reflect} \tag{5.31}$$

to each neighbor to compute a reflection-corrected flux. This procedure is repeated until the reflected thermal flux is smaller than an user-defined fraction (i.e., i_{break}) of the initially calculated thermal flux (i.e., that given by Eqn. (5.28)):

$$i_{break} \, \dot{q}_{i-j} > \dot{q}_{j,reflect}. \tag{5.32}$$

After the above outlined discrete radiation model was embed into the open-source software package *LIGGGHTS*, we study the thermal transport in a fully periodic, linear granular shear flow. The next Section outlines the equations that govern particle motion in such a flow.

5.2.4 Particle Flow Model

As in earlier work (Forgber et al. [28], [29]), we do not solve any equation for the fluid phase (i.e., the ambient fluid) and assume a fixed heat transfer coefficient α, as well as a fixed ambient fluid temperature T_f. This does not limit the applicability of the method, or the main conclusions as discussed in this previous work. All equations solved are summarized in Tab. (5.1), an all unknown particle parameters are listed in Tab. (5.2).

In order to correctly account for particle movement and particle-particle interactions, we rely on the open-source software package *LIGGGHTS* [24], [32]. Together with a spring-dashpot model, it is used to predict particle-particle contact forces [24]. Specifically, the following contact force models in the tangential (i.e., $\mathbf{f}_{i,j}^{t}$) and normal direction (i.e., $\mathbf{f}_{i,j}^{n}$) were used:

$$\mathbf{f}_{i,j}^{n} = k^{n}\,\delta_{ij}\mathbf{n}_{ij} - \eta^{n}\,\mathbf{v}_{ij}^{n} \tag{5.33}$$

$$\mathbf{f}_{i,j}^{t} = -k^{t}\,\mathbf{u}_{ij}^{t} - \eta^{t}\mathbf{v}_{ij}^{t} \tag{5.34}$$

with:

$$\delta_{ij} = r_i + r_j - \mid \mathbf{x}_i - \mathbf{x}_j \mid . \tag{5.35}$$

In what follows, we introduce the most important quantities needed to interpret our work. The characteristic contact time t_{co} of the above linear spring-dashpot model is defined as:

$$t_{co} = \pi \,/\, \omega \tag{5.36}$$

with

$$\omega = \sqrt{(k/m_{eff} - \eta^2)\,/\,(4\,m_{eff}^2)}. \tag{5.37}$$

Thereby, the contact time t_{co} limits the time step $\triangle t$ for the integration of

Newtons equations of motion. The coefficient of restitution e^n reads

$$e^n = \exp\left(\frac{-\pi\eta^n}{m_{eff}\sqrt{4\,k^n/m_{eff} - \eta^{n^2}/m_{eff}^2}}\right) \tag{5.38}$$

and was adjusted to 0.9. For relevant parameter ranges in our present work, we refer to Tab. (5.3). The spring stiffness and damping coefficient in the normal and tangential direction are chosen to be equal. Specifically, η and k are adjusted to obtain a certain restitution coefficient and to realize a predefined dimensionless shear rate $\dot{\gamma}$. Note that the dimensionless shear rate is used as an indication for the particle stiffness. For more information on the routines to calculate, e.g., the corresponding effective Young's modulus, and parameter ranges, the reader is referred to Section 5.5 and Appendix A.

Reference System	Equation
Particle flow	$\frac{d\,\mathbf{x}_i}{d\,t} = \mathbf{v}_i$ $m\,\frac{d\,\mathbf{v}_i}{d\,t} = \sum_j (\mathbf{f}^t_{ij} + \mathbf{f}^n_{ij})$ $I_i\,\frac{d\,\boldsymbol{\omega}_i}{d\,t} = \sum_j \mathbf{f}^t_{ij} \times \mathbf{r}_{ij}$
Internal thermal transport	$\frac{\partial T}{\partial t} = a \cdot \left(\frac{\partial^2 T}{\partial r^2} + \frac{2}{r}\frac{\partial T}{\partial r}\right)$

Table 5.1: Covering equations for particle flow (Newtons equation of motion) and equations regarding internal thermal transport in spherical coordinates in one-dimensional form.

5.2.5 Governing Equations for Intra-Particle Heat Transport

For modelling the thermal transport inside the particle, the simulation tool *ParScale* [49] is used. *ParScale* features a broad range of applications, including resolving individual property profiles (e.g., a chemical species) and a variety of chemical and drying models (Forgber et al. [51]). In the present work, only individual temperature profiles of each particle are accounted for. By using the Method of Lines (MoL), exploiting routines present in the *CVODE* package (for

Reference System	Unknown quantities
Particle flow	Angular velocity $\boldsymbol{\omega}_i$
	Particle velocities $\mathbf{v}_i$
	Particle positions $\mathbf{x}_i$
Internal thermal transport	Particle temperature T

Table 5.2: List of unknown simulation quantities.

details see [52], Forgber et al. [28]), we are able to perform stable simulations, even under fast changing environmental conditions (Cohen et al. [53]). For a more detailed insight into the solution procedure, and for an overview of the parallel coupling strategy, we refer to Forgber et al. [28] and the comprehensive online documentation of *ParScale* [49].

The assumption adopted in our present work is that the particle bed can be described by an ensemble of solid non-porous spheres. The thermal energy balance equation is first discretized in the radial coordinate only, and integrated in time using a fixed spatial discretization (i.e., radial space resolution). In other words, the differential heat balance in spherical coordinates is solved (see Eqn. (5.40)) assuming spherical symmetry. Heat conduction in solid non-porous particles can be modelled assuming a constant thermal diffusivity a:

$$a = \frac{\lambda_p}{\rho\, c_p} \tag{5.39}$$

$$\frac{\partial\, T}{\partial\, t} = -\nabla \cdot \left(-a \frac{\partial T}{\partial r}\right) + \frac{q}{\rho\, c_p}. \tag{5.40}$$

In case of particle-particle collisions, the resulting conductive flux (calculated based on the particle-particle overlap area) is considered in Eqn. (5.40) by applying the source term q in the outermost shell of the particle. The heat transfer coefficient α sets the boundary condition for T at the outmost particle shell temperature, completing our intra-particle heat conduction model. For discretization in physical space a second order central differencing scheme is used we details outlined in Forgber et al. [28] and the online documentation

[49]. The next Section defines all relevant thermal fluxes that are accessible via the calculated particle and contact information (i.e., particle positions, speed, particle-particle overlap areas, as well as temperatures). These fluxes represent the main outcome of our simulations can can be used to close continuum models of granular matter.

5.2.6 Thermal Fluxes

The convective flux (Eqn. (5.41)) is defined as the redistribution of thermal energy due to the particles' movement inside the simulation domain. In contrast, the conductive thermal flux (Eqn. (5.42)) accounts for the heat exchanged between two particles in case of collisions. The transferred heat flux (Eqn. (5.43)) describes the exchange of thermal energy between particle and an ambient fluid. It is a function of the temperature difference between particles and the ambient fluid, and the heat transfer coefficient α. Note that $\mathbf{q}^{cond}$ is calculated for the sum of all contacts in the domain with the volume V and only defined for particles with equal thermal conductivity.

$$\mathbf{q}^{conv} = \frac{1}{V} \sum_i m_i \, c_{p,i} \, T_{vol,avg,i} \, \mathbf{v}_i \tag{5.41}$$

$$\mathbf{q}^{cond} = \frac{1}{V} \sum_{co} 2 \, \lambda_p \, A_{co}^{1/2} \, (T_i - T_j) \, \mathbf{r}_{ij} \tag{5.42}$$

$$q_i^{trans} = \alpha \, (T_i - T_{f,i}). \tag{5.43}$$

A sheared bed of particles, driven by Lees-Edwards boundary conditions, demands the domain-averaged particle velocity to equal zero. As in our earlier work (Forgber et al. [28]), we split our domain in three thermal regions (see Fig. 5.17 in Sec. 5.5). Thermal fluxes are evaluated only in the middle region (i.e., region B). Only within this region the temperature gradient can evolve freely, which is why we have to enclude the boundary regions A and C. However, considering only region B causes a temporal fluctuation of the number (as well as the average speed) of the particles. Thus, a "drift" convective flux due to the non-zero average speed of the particles in the center region occurs, which overlays the convective flux due to individual particle motion we are interested in. Note, that convective thermal transport caused by the average (i.e., bulk) particle speed is easy to model in continuum models, and hence does not require a deeper analysis. The unwanted "drift" convective flux is characterized

by the velocity $\mathbf{v}_{drift}$, and affects the convective flux as follows:

$$\mathbf{q}^{conv} = \frac{1}{V} \sum_i m_i \, c_{p,i} \, T_{vol,avg,i} \, (\mathbf{v}_i + \mathbf{v}_{drift,i}). \tag{5.44}$$

Explicitly calculated, the drift flux is

$$\mathbf{q}_{drift} = \frac{1}{V} \mathbf{v}_{drift} \sum_i m_i \, c_p \, T_{vol,avg,i}. \tag{5.45}$$

Hence, it is easy to subtract the drift flux, and we have done so to report only corrected convective heat fluxes in what follows.

As mentioned above, the number of particles in region B fluctuates over time. Consequently, we need to weight the corrected convective flux (available at each time instant k) with the number of particles to calculate a meaningful time-average flux:

$$\mathbf{q}^{conv,av} = \frac{\sum\limits_k \mathbf{q}^{conv,k} \, N_{p,k}}{\sum\limits_k N_{p,k}}. \tag{5.46}$$

In what follows we drop the superscript "av" for all flux quantities, and employ the same time-averaging strategy for all other fluxes as well.

The radiative flux can be calculted from the particle-particle radiative fluxes as follows:

$$\mathbf{q}^{rad} = \frac{1}{V} \sum_i \frac{\sigma_s (T_i^4 - T_j^4)}{\dfrac{1-\epsilon_i}{A_i \, \epsilon_i} + \dfrac{1-\epsilon_j}{A_j \, \epsilon_j} + \dfrac{1}{\varepsilon_{i-j} \, A_i}} \mathbf{r}_{ij}. \tag{5.47}$$

Finally, we need to choose a reference flux to present our results in dimensionless quantities. Therefore, we choose the conductive flux in case our computational domain is completely filled with (a non-moving) solid material. Thus, the reference heat flux is simply:

$$q^{ref} = -\lambda_p \frac{\partial T}{\partial y}. \tag{5.48}$$

Here $\partial T / \partial y$ is the applied temperature gradient which is aligned with the gradient direction of the shear flow. Important for the thermal behaviour is

the total flux, observed in the sheared box. This total flux is defined via the summation:

$$\mathbf{q}^{tot} = \mathbf{q}^{conv} + \mathbf{q}^{cond} + \mathbf{q}^{rad}. \tag{5.49}$$

5.3 Verification and Model Benchmarking

In this Section we present a number of verification cases that demonstrate the correctness of the new discrete thermal radiation model. Also, we present a comparison with fvDOM-based simulations to benchmark the fidelity of the model. In every *OpenFOAM* simulation, we choose to have four angles in polar and angular direction each, which results in a total of 64 discretization angles for the S_N approximation.

5.3.1 FvDOM Infinite Long Plates

It is of key importance for our model to correctly predict the view factor between two surfaces including shadowing, simply because in dense granual flows shadowing plays a central role. Since an analytical solution cannot easily be derived for different shadowing states, we need to rely on results predicted by the fvDOM model available in the simulator *OpenFOAM*. To verify the correctness of the results generated by *OpenFOAM*, we first compare predictions for two infinite long plates at a fixed temperature difference, and considering different optical thicknesses (see the results in Fig. 5.8). Note that we do not solve for the flow field and all simulation parameters are shown in Tab. (5.4) in the Appendix. The analytical solution used to generate Fig. 5.8 is available in Howell et al. [22] and Crosbie et al. [54].

As show in the Figure above, the dimensionless radiative thermal flux Ψ_b is predicted correctly by *OpenFOAM*, and occurring differences are below $\sim 3\%$ for all thermal thicknesses studied. Note that Amouzandeh et al. [55] have already shown that only the fvDOM approach is able to predict the radiative thermal flux with sufficient accuracy (in contrast to the simpler P_1-model). Also, *OpenFOAM* offers the post-processing tool *patchAverage* for evaluating the average radiative thermal input on a surface, which is also used in what follows. Specifically, the next verification case is a comparison between *OpenFOAM*, Monte-Carlo data and our new discrete model regarding the view factor calculation in case of a two particle system.

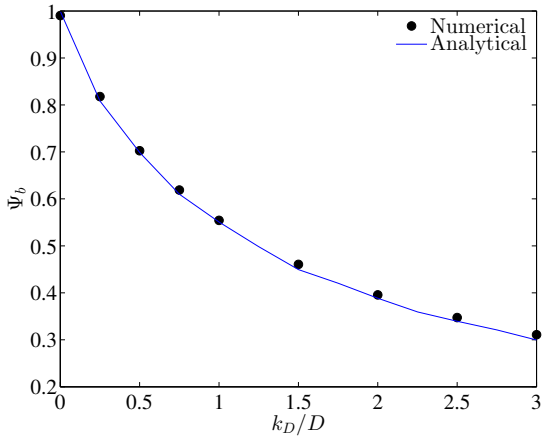

Figure 5.8: Verification of the dimensionless radiative flux in case of two infinite long parallel plates over a broad range of optical thicknesses.

5.3.2 Two Particle Setup

Even though a successful view factor evaluation in a two particle system has been demonstrated before (see Fig. 5.6), our further investigations rely on a correct calculation of thermal fluxes between spherical particles using the *OpenFOAM* simulator. Therefore, we compare the predicted view factors of our model to data obtained from Monte-Carlo simulations, and data predicted by *OpenFOAM* using the fvDOM method and an appropriate computational mesh. A typical simulation setup is shown in Fig. 5.9, and all simulation parameter ranges are listed in Tab. (5.4). Note that in this setup the surface temperatures of both particles are kept at different but constant values in order to achieve a steady-state solution. The view factor can be easily calculated by relating the average flux against the maximum possible radiative flux that occurs if the view factor. Thus, we use:

$$\varepsilon_{i-j} = \frac{\dot{q}_{avg,in}}{\dot{q}_{max,i-j}} = \frac{\dot{q}_{avg,j}}{\sigma_s \left(T_i^4 - T_j^4\right)}. \tag{5.50}$$

For further benchmarking we use the dimensionless particle surface distance S_{i-j} (see Sec. 5.2.2), and compare the so calculated analytical view factors with our results shown in Fig. 5.10.

Due to our angle correction approach the differences between the discrete model and the data obtained with a Monte-Carlo method is negligibly small, as expected. In contrast, *OpenFOAM* shows a good agreement until $S_{i-j} \sim 1$, with increasing errors for increasing particle-particle distances. The maximum

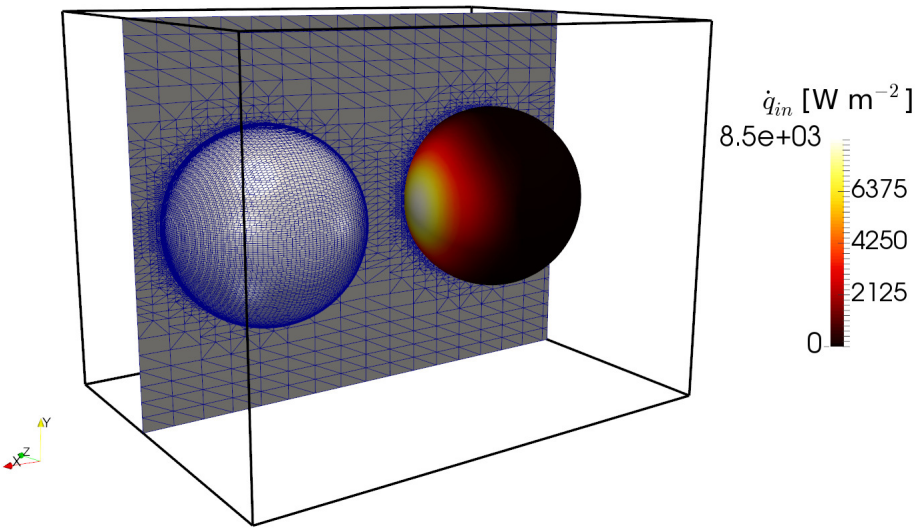

Figure 5.9: Computational domain including illustration of the body-fitted mesh in a two particle setup. The white particle i on the left is emitting a radiative heat flux towards the second particle j. The latter is colored according the incoming radiative flux.

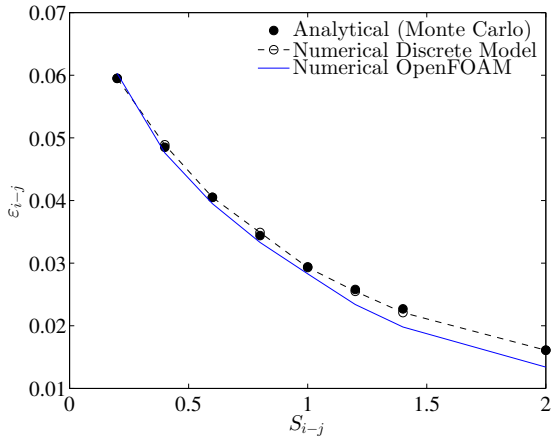

Figure 5.10: Calculated view factors in a two particle system over the dimensionless surface distance based on (i) an analytical calculation (Felske [46], Jones [47]), (ii) our discrete model, and (iii) the fvDOM approach implemented in *OpenFOAM*.

difference observed is $\sim 5\%$ at $S_{i-j} = 2$. The reason for this is as follows: every simulation using the fvDOM is a trade off between using a larger number of discretization angles (more accurate at smaller distances) and the well known "false scattering" and "ray effects" if the surfaces move further apart (see Modest [33]). Fortunately, in the dense granular flows considered in our present

contribution, particle-particle surface distances larger than 2 are rare. Thus, in the following, we use the fvDOM method to generate reference data to quantify shadowing in a three particle system. This data is then used to benchmark how well our simplified model can represent such shadowing phenomena.

5.3.3 Shadowing Effects in a Three Particle System

In case two particles are shadowing each other, no analytical solution for the radiative flux is available any more. The only way to predict view factors in such a case are numerical methods. To verify our simplified model for situations in which shadowing occurs, we create the geometrical setup shown in Fig. 5.11. We fix the positions of particle i and j and adopt the position of particle $j+1$

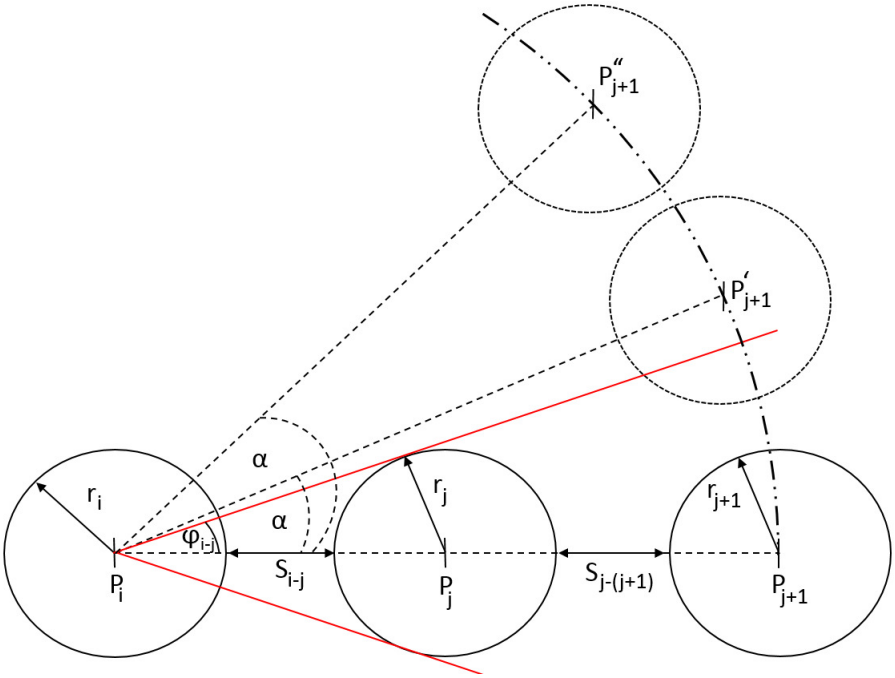

Figure 5.11: Setup for studying shadowing in a three particle system.

in such a way that $S_{i-(j+1)}$ (i.e., the dimensionless surface distance) remains constant. Based on a pre-defined angle α (see Fig. 5.12) we update the position of particle $j+1$ to study different configurations. A sample result of such a variation for $\alpha = 30°$ is shown below.

As it can be seen from Fig. 5.12, particle $j+1$ is partially shadowed by particle j and consequently the radiative thermal transport is reduced. The same

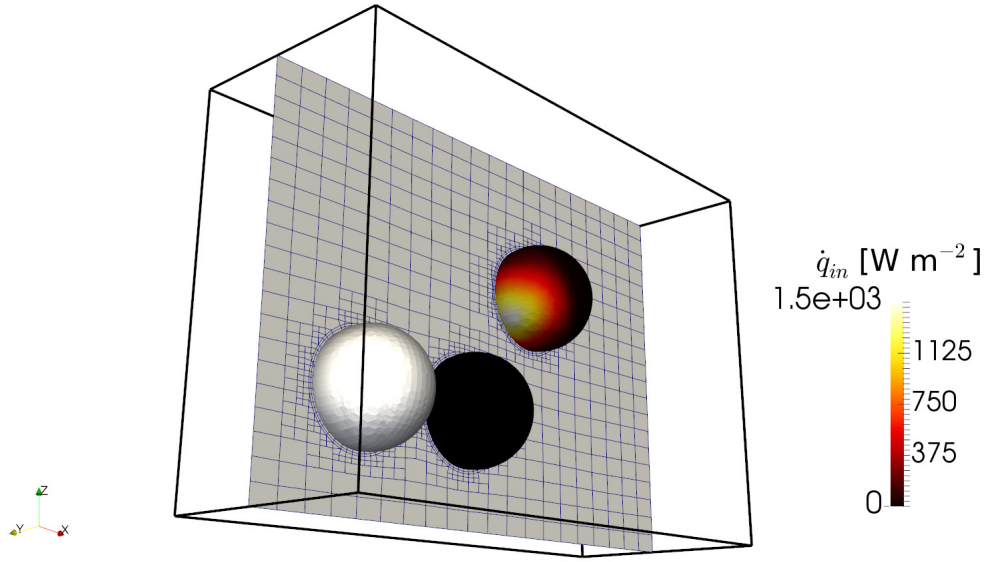

Figure 5.12: *OpenFOAM* example solution for three particle setup with $\alpha = 30°$ and a partially shadowed particle $j+1$. The emitting particle is white, the shadowing particle is black, and particle $j+1$ is coloured according to the intrinsic radiative flux.

geometrical setup is considered with our simplified model, and the obtained distribution of surface points (used to calculate the view factors) is illustrated in Fig. 5.13. Using Eqn. (5.26) the view factors can be calculated for each particle. The comparison between the discrete model, and the results obtained via the fvDOM is shown in Fig. 5.14.

Clearly, the view factors calculated for a variety of angles α agree reasonably well. However, examining the results for an angle of $\alpha < 10°$ in greater detail, we see that no view factor is calculated for particle $j+1$ in the discrete model. In contrast, the more accurate fvDOM predicts a view factor of ca. 0.001 for that angle. The reason is identical to that of the solid angle correction discussed in Sec. 5.2.2: the assumption that all thermal radiation is emitted from the center of each particle is not precise. In case of particle assemblies this introduces a "blind angle" for which particle $j+1$ has to be shifted in order to be "seen" by particle i. For all angles below a certain threshold the points will be registered as shadowed points by particle j. Clearly this angle is also depending on the particular particle positions and the dimensionless particle distance. With increasing α, the error is decreasing significantly and remains below $\sim 5\%$ for $\alpha > 25°$. At $\alpha \sim 40\%$ particle $j+1$ is not shadowed by particle j anymore, resulting in an excellent match of results obtained with both approaches. We conclude that our model works well above a certain threshold of a shifting angle α. It should be pointed out that the presented geometrical setup represents a "worst" case scenario,

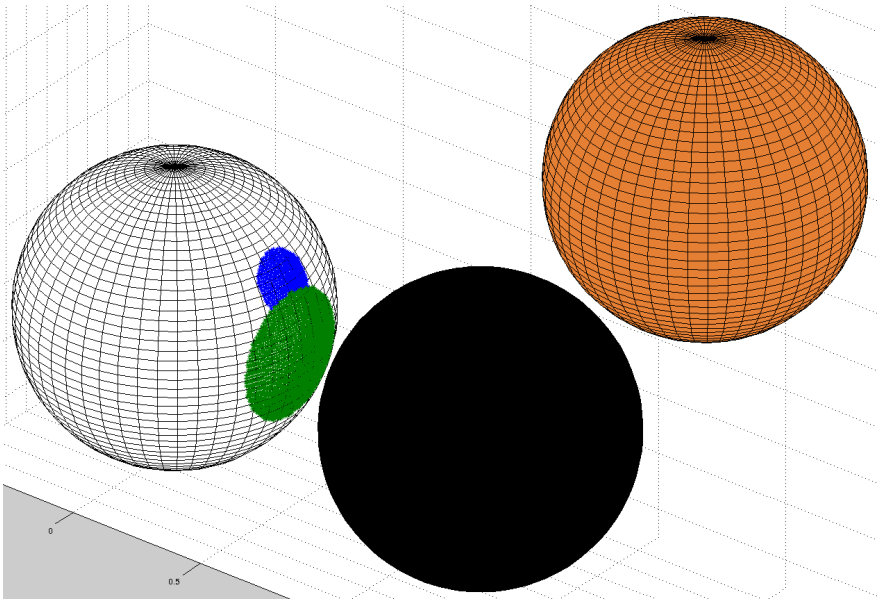

Figure 5.13: Discrete model solution for three particle setup with $\alpha = 30°$ and a partially shadowed particle $j+1$ colored in orange. The emitting particle is white, and the shadowing particle is black.

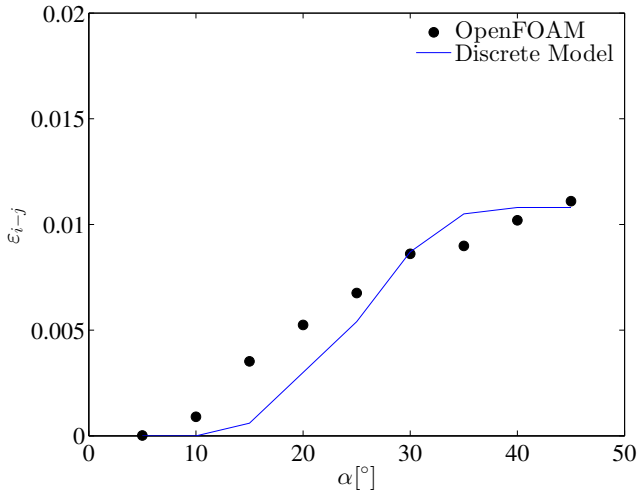

Figure 5.14: Comparision of predictions using the fvDOM available in *OpenFOAM* and that of the newly developed discrete model.

as all particles are placed in line. Therefore, the next Section considers a more relevant verification case, i.e., a fixed dense arrangement of spheres.

5.3.4 Dense Particle Ensemble

We present a comparison of fvDOM-based predictions an that made by our discrete model considering a dense particle bed characterized by different particle concentrations. Therefore, we use simulated particle positions (from a typical shear flow simulation) and use both approaches to compute radiative fluxes. Again, our goal is to verify the discrete model also under more realistic situations that may occur in moderately dense to dense granular flows. Specifically, we realize five different initialisations of each system, i.e., five systems with the same number of particles but different positions are considered, and results were averaged. This was achieved through the sampling of particle position data at different time steps during a shear flow simulation (see Section 5.5). The particle closest to the center of the simulation domain is chosen to emit thermal radiation. This ensures that a maximum amount of reference data, including shadowing effects, is collected per setup. After the fvDOM-base simulation is finished, we compute the intrinsic radiative fluxes (averaged for every particle surface), and consequently the view factors. A sample result of a steady state solution including the generated mesh can be seen in Fig. 5.15. Again, for all simulation parameters, we refer to Tab. (5.4). By using the same particle

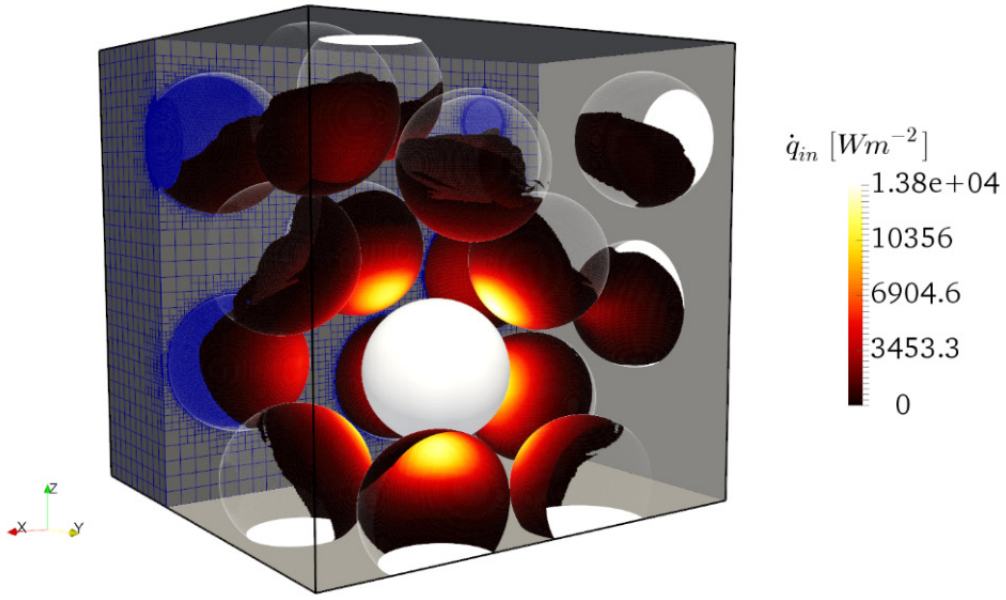

Figure 5.15: Sample result predicted by the fvDOM solver available in *OpenFOAM* for a packed bed with an average particle volume fraction of $\phi_p \sim 0.5$.

positions, we probe view factors with the discrete model and compare the result (for each particle) with that predicted by fvDOM. The resulting average

errors, as well as the standard deviations of the error and the maximum errors are summarized in Fig. 5.16. Note that the errors are normalized with the maximum view factor in case of two mono-sized spherically shaped particles, i.e., $\varepsilon_{max} = 0.0762$. Again, we want to point out, that every point represents an average of five initialisations of the same volume fraction. We observe a nearly

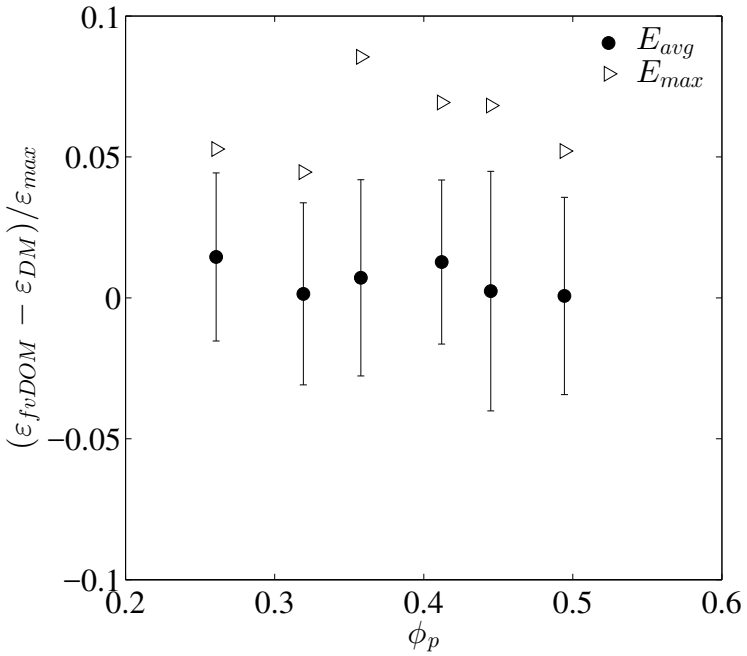

Figure 5.16: Normalized error of the calculated view factors using the discrete model from that calculated using the $fvDOM$.

constant error for all studied volume fractions with a maximum average error of $\sim 1.5\%$ at $\phi_p = 0.26$. Also the standard deviation of the error remains constant over the studied volume fraction with a maximum value of about $\sim 3.5\%$ at $\phi_p = 0.44$. With a maximum particle based error of 8.5% for $\phi_p = 0.36$ we conclude that our model performs well over a variety of volume fractions and initializations. The occurring errors can be explained with the "blind angle" (see Sec. 5.3.3), and are well below a relevant threshold for most engineering applications. After a strict verification, we can now apply the discrete model in order to evaluate the influence of thermal radiation under well controlled conditions using a fully periodic, sheared box. To ensure the applicability of our results summarized below, we next discuss dimensionless quantities for thermal transport in granular shear flows for which radiation is significant.

5.4 Dimensional Analysis

The key dimensionless parameters that characterize a sheared particle bed have been extensively discussed by Chialvo et al. [31], Mohan et al. [32] and Forgber et al. [28], [28]. In agreement with Chialvo et al. [31] we define a dimensionless shear rate as

$$\dot{\gamma} = \gamma \, d_p^{3/2} / \sqrt{k_n / \rho_p}. \tag{5.51}$$

Since the dimensionless shear rate scales with the inverse of the spring stiffness k_n, it can be seen as a metric that quantifies the relative "softness" of the particles. Recent simulations (Hatano et al. [56], Otsuki et al. [57], Alonso-Marroquín et al. [58], Chialvo et al. [31]) and experiments by Nordstrom et al. [59] provide simple expressions that correlate the dimensionless shear and particle concentration with the stress. Namely, the scaled stress-shear rate data can be collapsed into curves as shown below. Earlier work showed that such a collapse and scaling can also be achieved with the conductive thermal flux (Forgber et al. [28]). Furthermore, it is possible to determine the state of a sheared granular material (unjammed, jammed, crystallized) by evaluating the thermal fluxes (Forgber et al. [29]).

$$p_{int} \sim |\phi - \phi_c|^0 \tag{5.52}$$

$$p_{QS} \sim |\phi - \phi_c|^{2/3} \tag{5.53}$$

$$p_{inert} \sim |\phi - \phi_c|^{-2}. \tag{5.54}$$

Mohan et al. [32] pointed out that the Peclet number is the most influential parameter for heat transport in granular materials, which reads:

$$Pe = \frac{d_p^2 \, \rho_c \, c_p}{4 \, \lambda_p} \, \gamma. \tag{5.55}$$

Pe characterizes the relative rates of convective and conductive heat transport within the particles bed in the absence of heat transfer to the ambient fluid. If we consider this heat transfer mechanism as well, the Biot number is the most influential dimensionless parameter, which is defined as

$$Bi = \frac{\alpha \, d_p}{\lambda_p}. \tag{5.56}$$

The Biot number relates (i) the intra-particle and (ii) the external resistance to heat transport. In earlier work (Forgber et al. [28]) we showed that intra-particle temperature profiles should be accounted for in certain situations, and proposed an alternative dimensionless number which is defined as

$$\Pi_1 = \frac{Pe}{Bi} = \frac{\rho_p \, c_p \, d_p \, \gamma}{\alpha}. \tag{5.57}$$

Π_1 can be interpreted as a scaled length over which convective transport is able to balance the cooling (or heating) caused by the ambient fluid. For fixed values of Π_1 one can illustrate the effect of heat conduction within the particles by varying the Biot number. Note, that for fixed Pe a variation of Bi does not lead to such a transparent illustration, since also Pe is a function of the particles' heat conductivity, and both dimensionless numbers are zero in the limit of infinitely fast heat conduction within the particles. When accounting for radiative thermal transport, the most obvious additional (dimensionless) parameters to consider are the emissivities ϵ of the particles. However, an additional dimensionless manner is needed for radiative transport since the absolute temperature level plays a crucial role. Therefore, we introduce Π_2 - defined in analogy to the Boltzmann number that is often used to express radiative heating of a gas - as follows:

$$\Pi_2 = \frac{\epsilon \, \sigma_s \, T_{ref}^4}{\lambda_p \, \partial_y \, T}. \tag{5.58}$$

Π_2 relates a typical radiative heat flux to a characteristic thermal transport rate by conduction in a granular material. These dimensionless quantities enable us to study a system, which can be scaled to any real life application. We now apply the developed discrete radiation model to a fully periodic shear flow to identify situations in which radiation is important.

5.5 Radiative Thermal Exchange in Granular Shear Flow

We now investigate the thermal behaviour of a sheared particle bed under different flow and thermal conditions including the influence of radiation. By applying Lees-Edwards boundary conditions to an otherwise fully periodic box we drive a homogeneous linear shear flow. Such studies of thermal transport allow to gain fundamental insight into which flow and thermal parameters

affect thermal fluxes through a granular material. This insight may help to establish a continuum-based description of thermal fluxes in future.

A combination of *LIGGGHTS* and *ParScale* is used to simulate the temperature distribution on top of the flow. The dimensions of the simulation box are chosen to be $H/d_p = 15$, and a wide range of particle volume fractions (ϕ_p = 0.30-0.64) is studied. The z-direction serves as the spanwise direction, whereas in x-direction the homogeneous shear flow is driven. In y-direction we apply a temperature gradient by fixing the temperatures in the top and bottom layer (i.e., regions A and C in Fig. 5.17). The variation of T_{top} enables us to reach a broad range of Π_2-values (compare Eqn. (5.58)). Fig. 5.17 summarizes this setup in the $y-x$ plane, in which region A and C are the hot and cold region, respectively. In region B the temperature of the particles is allowed to evolve freely. Consequently, we must not take the top and bottom layer into account during our post processing procedures, and just analyse thermal transport in the center region, i.e., region B. In order to study the transferred heat to the ambient fluid, the fluid temperature is set equal to the average of the top and bottom temperature. We chose Region B to be $11.5\,d_p$ which ensures a representative number of particles to represent the desired volume fraction.

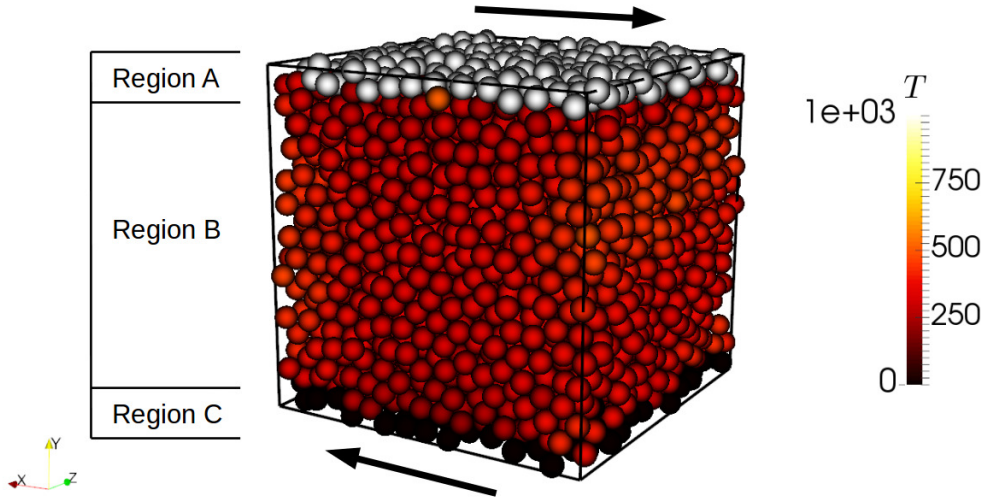

Figure 5.17: Setup used for the shear flow simulations, illustrating the thermal regions A, B and C.

Due to the wide range of dimensionless influence parameters (see also Rognon et al. [30], Chialvo et al. [31]), we restrict our study to the ranges presented in Tab. (5.3). The chosen range enables us study a broad range of systems with focus on (i) stiff particles ($\dot{\gamma} = 10^{-4}$), (ii) moderately dense to dense flows,

and most important (iii) greatly differing temperature levels characterized by a variation of Π_2 by more than 10 orders of magnitude. According to Ozkaynak et al. [23], the assumption of $\epsilon \sim 1$ is valid for stiff particles made of metal at high temperatures. Since we must choose a large radiation interaction radius (i.e., $r = 3\,d_p$) to consider all relevant particle-particle pairs for radiation, particles might emit thermal radiation across the periodic boundaries. This is especially problematic if this occurs through the top and bottom thermal regions in which the particle temperatures are fixed. Consequently, we enforce zero thermal radiative exchange across all boundaries. Note that for an emission coefficient of $\epsilon = 1$ this is unproblematic since the radiation is quickly absorbed by the particles in the flow and spanwise direction - only decreasing ϵ would be problematic since reflected radiation may lead to extremely long-range thermal fluxes.

Table 5.3: Parameter ranges considered for granular shear flow simulations.

Parameter	Min. Value	Max. Value
ϕ_p	0.3	0.64
$\dot{\gamma}$	10^{-4}	10^{-2}
Pe	10^{-2}	10^{2}
Bi	0	10
T_{top}	1	1000
Π_2	$2.6 \cdot 10^{-8}$	$2.6 \cdot 10^{5}$
μ	0.1	fixed
e	0.9	fixed
T_f	$(T_{top} + T_{bot})/2$	fixed
ϵ	1	fixed
Radiation volume radius	$3\,d_p$	fixed

For all shear flow simulations the flow converges into a statistical quasi-steady state after a few box deformations. Thereafter, convective, conductive and radiative fluxes through the sheared particle bed can be averaged and compared. We define this steady state by means of a constant (or constantly fluctuating) contact pressure, conductive and convective flux. In the next Section we study the dependency of the radiative thermal flux on different temperature levels, i.e., we consider a variation of the Π_2 value, in combination with Biot numbers.

5.5.1 Biot Number Effect on Radiative Fluxes

It is of major importance to picture the influence of transferred heat to the environment, accomplished by a constant heat transfer coefficient α and a constant environment temperature $T_f = (T_{top} + T_{bot})/2$, on the radiative thermal flux. By studying both quantities in our sheared box setup, we are able to depict the influence of the Biot number on the dimensionless radiative transport for a broad range of flow situations. Fig. 5.18 summarizes the influence of the Biot

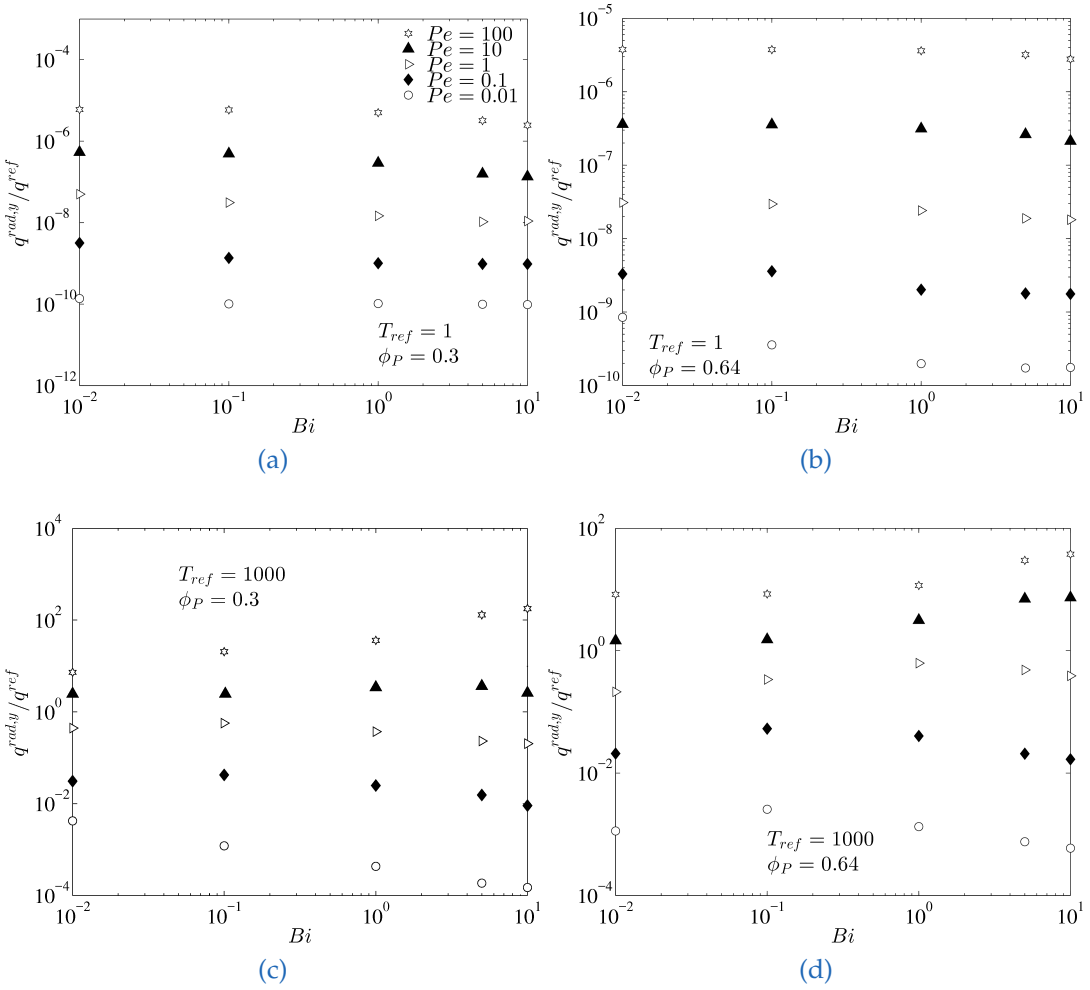

Figure 5.18: Radiative flux versus Biot number for different Peclet numbers, reference temperatures and volume fractions. (a) $T_{ref} = 1, \phi_p = 0.3$, (b) $T_{ref} = 1, \phi_p = 0.64$, (c) $T_{ref} = 1000, \phi_p = 0.3$, (a) $T_{ref} = 1000, \phi_p = 0.64$.

and Peclet number at low reference temperatures (panel (a) and (b)) and high

reference temperatures (panel (c) and (d)). Clearly, higher Peclet numbers lead to a drastic increase in the radiative flux for all Biot numbers, volume fractions and reference temperatures. In contrast, the difference found for dilute and dense cases is much smaller - this will be taken in closer consideration in one of the next Sections. For low reference temperatures (panel (a) and (b)) we see a constant radiative thermal flux for moderate Biot numbers (i.e., $Bi < 1$). When considering increasing Biot numbers (i.e., $Bi > 1$), a small decrease in the dimensionless radiative flux is observed. This decrease is seen among all Peclet numbers and volume fractions. We speculate that the reference temperature is too small and the transferred thermal energy transported to the ambient fluid too high, even in fast sheared beds. Both factors lead to small absolute temperature differences between the particles, resulting in a decrease of the radiative transport rate for increasing Biot numbers.

When considering higher reference temperatures (i.e., panel (c) and (d) in Fig. 5.18), this trend is not observed. At both volume fractions (panel (c) $\phi_p = 0.3$, panel (d) $\phi_p = 0.64$)) there is a clear difference in the trend depending on the Peclet number. Whereas at low Biot numbers ($Bi < 0.1$), the radiative flux remains nearly constant, at high Biot numbers along with high Peclet numbers, we observe an increasing amount of heat transfer through radiation. Since we fix T_{top} and T_{bot} in our simulation setup, a higher reference temperature implies a higher absolute temperature gradient. In cases of fast sheared beds (or thermally thick particles, see Eqn. (5.55)) the temperature differences between particles increase, since particles of higher temperature penetrate "cold" regions more easily without a decrease in temperature. High Biot numbers amplify the effect and an enhancement is seen in the radiative flux. In contrast, for slow shearing we agree with the reduction, also seen from low reference temperatures. Most interesting, we find radiative fluxes to be up to 150 q^{ref} (see Eqn. (5.48)). This is true especially for high Peclet numbers along with high reference temperatures. After evaluating the influence of the Biot number under different thermal levels, we now make predictions on how the volume fraction affects the radiative flux in a sheared particle bed.

5.5.2 Radiative Fluxes are weakly affected by the Packing Density

Until now, only a few quantitative studies on the influence of the particle volume fraction on thermal radiation exist. With the current Section, we aim towards a more rigorous assessment on the importance of the particle packing fraction. Our results in this respect are shown in Fig. 5.19. We show the evolution of

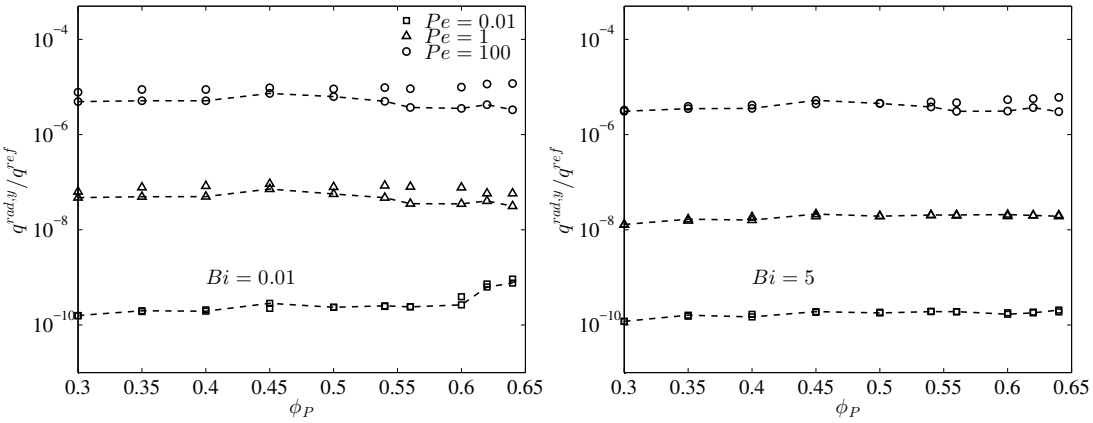

Figure 5.19: Radiative flux versus the particle volume fraction ϕ_p for two different Biot numbers ($Bi = 0.01$ in panel (a), $Bi = 5$ in panel (b)), particle stiffness and Peclet numbers with a low reference temperature ($T_{ref} = 1$). Dotted lines represent a dimensionless shear rate equal to $\dot{\gamma} = 10^{-4}$, symbols represent $\dot{\gamma} = 10^{-3}$.

the dimensionless thermal radiative flux as a function of the particle volume fraction ranging from a relatively dilute flow ($\phi_p = 0.3$) to the densest possible packing ($\phi_p = 0.64$). We study the behaviour for a low and high Biot number including the influence of the Peclet number and particle stiffness. At the lowest temperature level taken into account (i.e., $\Pi_2 = 2.6 \cdot 10^{-8}$ for $Pe = 0.01$, $\Pi_2 = 2.6 \cdot 10^{-6}$ for $Pe = 1$, $\Pi_2 = 2.6 \cdot 10^{-4}$ for $Pe = 100$), we find the dimensionless flux to remain constant over the particle volume fraction. This conclusion also holds for a wide range of Peclet numbers (i.e., speed of shearing). Thereby, it is clear that a higher Peclet number at a constant particle fraction results in an enhanced thermal transport through radiation as shown before (compare Fig. 5.18). The second observation from Fig. 5.19 is a clear independence of the dimensionless thermal radiative flux on the particle stiffness. We speculate two reasons for the seen trends: First, the range of parameters might not be sufficient to draw a more rigorous general conclusion. Since we limit the study to mono-disperse spheres, the maximum packing fraction is limited to $\phi_p = 0.64$. It appears that for the moderately dense flows characterized by $\phi_p = 0.30$ no significant change in the regime of radiative transport occurs. A second reason is that the considered particle stiffness lead to granular flow that is always in the inertial or quasi-static flow regime. Since the particle-particle overlap in these flows is at most a few percent of the particle diameter, the view factors are not affected by the stiffness. Therefore, the particle stiffness has essentially no effect on radiative fluxes.

Fig. 5.20 shows our data for higher reference temperatures to support more general conclusion. Specifically, we consider Π_2 ranging from 26.83 to $2.6 \cdot 10^5$ in

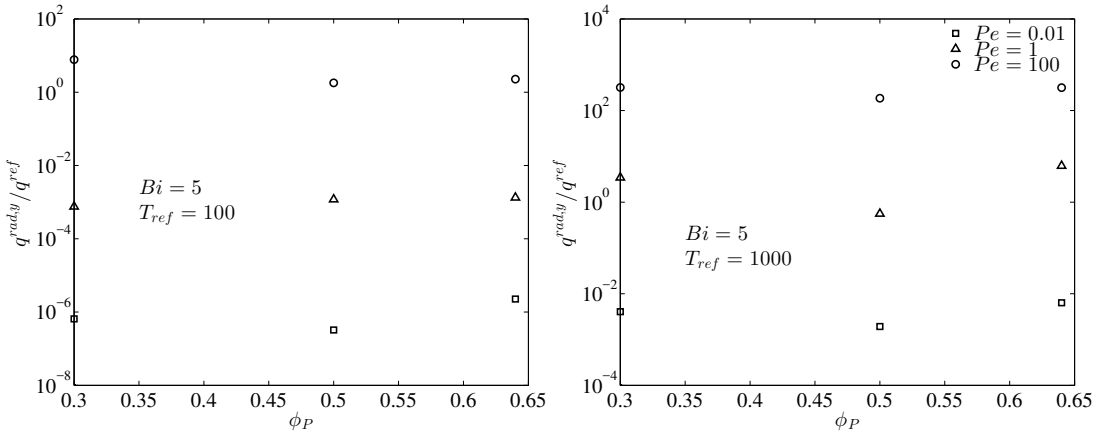

Figure 5.20: Radiative flux versus the particle volume fraction ϕ_p for $Bi = 5$ and (a) $T_{ref} = 100$, as well as (b) $T_{ref} = 1,000$.

panel (a), and from 0.026 to 260.83 in panel (b) of Fig. 5.20. These dimensionless parameters represent more realistic conditions as found in typical chemical engineering applications. However, the results support our finding from Fig. 5.19, that the particle volume fraction has no major influence on the thermal transport rate via radiation. We conclude that the influence of the Peclet number is of much greater importance as studied in the next Section.

5.5.3 Radiative Flux versus the Peclet Number

From our earlier results (see Fig. 5.18 and Fig. 5.20) we have already shown that the Peclet number has, along with the reference temperature, the greatest influence on the radiative thermal transport in the particle bed. Therefore, we now illustrate the dependency on the Peclet number in Fig. 5.21. Specifically, we look at (a) a dilute flow with low transferred heat to the environment, (b) dilute flow and high Biot number, (c) dense flow with low Biot number and (d) dense flow with large amount of transferred heat to the environment fluid. By plotting the dimensionless radiative heat flux against the Peclet number, we observe a linear increase for all investigated reference temperatures. Thereby, the radiative flux can reach significant levels (i.e., $\sim$ 10% of q^{ref} or higher) at (i) moderate Peclet numbers (i.e., $Pe > 1$) in combination with high reference temperatures

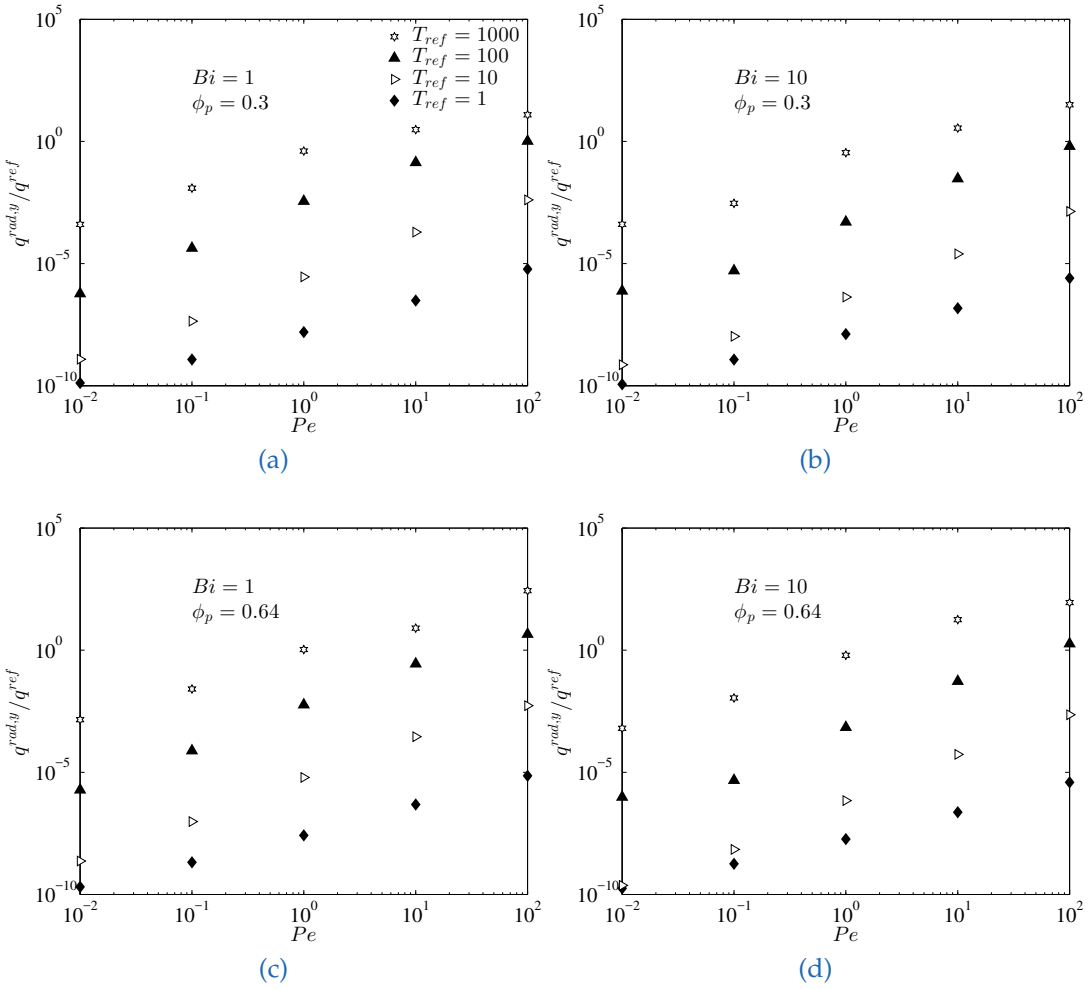

Figure 5.21: Radiative flux versus the Peclet number for different Biot numbers, reference temperatures and volume fractions. (a) $Bi = 1, \phi_p = 0.3$, (b) $Bi = 10, \phi_p = 0.3$, (c) $Bi = 1, \phi_p = 0.64$, (a) $Bi = 10, \phi_p = 0.64$.

(i.e., $T_{ref} > 1000$) or (ii) high Peclet numbers (i.e., $Pe > 100$) accompanied with moderate reference temperatures (i.e., $T_{ref} > 100$). From Fig. 5.21 we conclude, that thermal transport via radiation is not only an important heat transfer mechanism at very high temperatures, but reaches significance in fast sheared systems or in applications with particles made of thermally resistant materials. The latter is explained by the decreasing reference heat flux in these systems, for which we have chosen the conductive flux as explained in Section 5.2.6. We now aim on collapsing our data for the radiative flux, combining both dimensionless quantities Π_1 and Π_2. Such a collapse would enable a fast estimation of whether radiative thermal transport plays a role in a certain granular flow or not.

5.5.4 Relating Radiative Fluxes to $\Pi_1\,\Pi_2$

In Sec. 5.4 we defined two dimensionless quantities which we find sufficient to describe the thermal behaviour in the sheared box with respect to the radiative fluxes. As mentioned before, Π_1 relates convective transport to the transferred heat to the environment. By a variation of Bi, Π_1 can illustrate the importance of heat conduction inside the particle. Π_2 on the other hand, relates the thermal energy input via radiation to the transport through conduction. Interestingly, we find a collapse of our data for the dimensionless radiative flux when plotted versus the product of Π_1 and Π_2 (see Fig. 5.22).

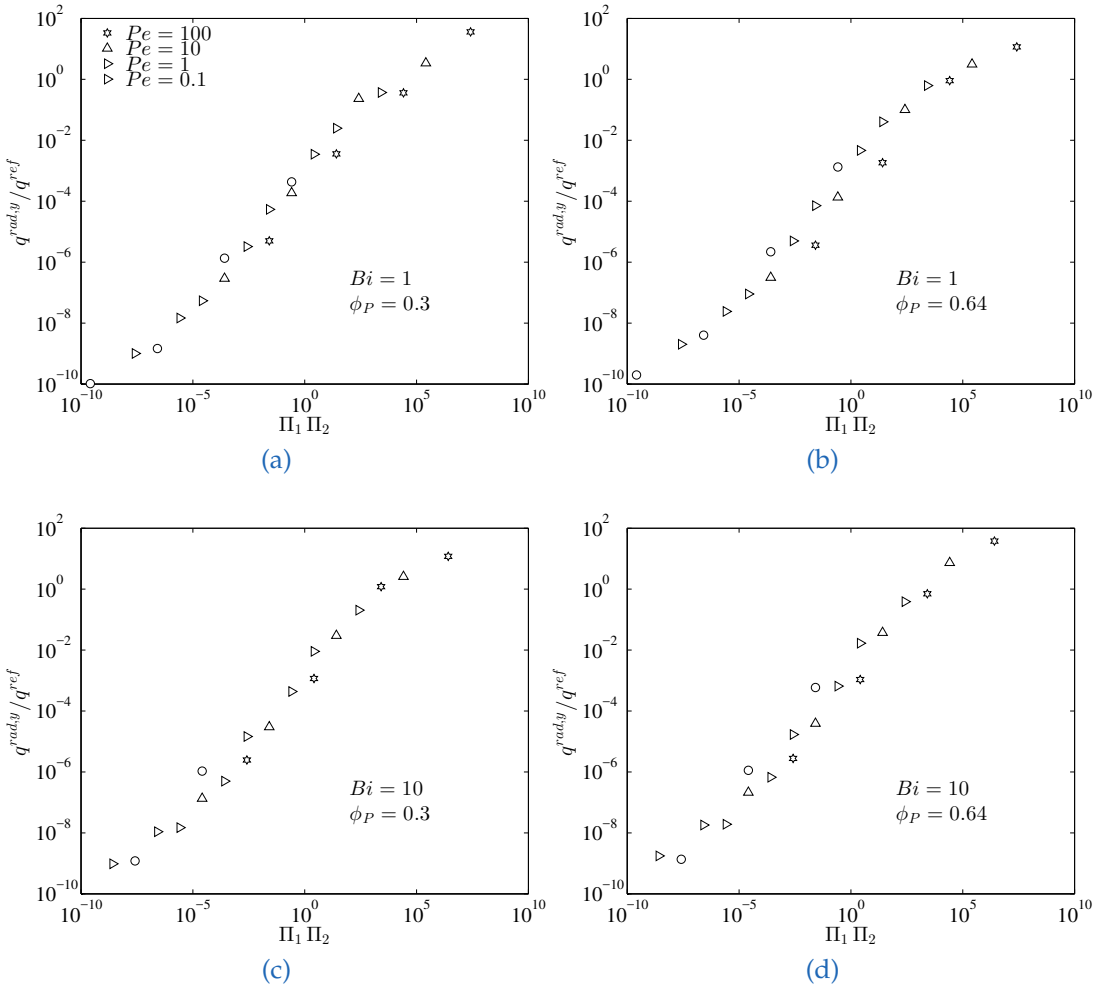

Figure 5.22: Dimensionless radiative heat flux versus the product of Π_1 and Π_2.

Even more surprising, an almost linear increase of the radiative flux for a wide

range of Biot numbers and volume fractions is found, when plotting over $\Pi_1\,\Pi_2$ and scaled logarithmically. Specifically, the slope of a curve approximating our data in Fig. 5.22 suggests that the radiative flux is proportional to $(\Pi_1\,\Pi_2)^{(2/3)}$

Thereby, high values for $\Pi_1\,\Pi_2$ indicate a fast sheared box at a high reference temperature, accompanied by low transferred heat fluxes to the ambient fluid. In other words, large radiative heat fluxes necessitate insignificant cooling by the ambient fluid. This is since in rapidly cooled granular flows cold particles would shield radiative transfer from hot particles deeper into the particle bed. In contrast, low values of the dimensionless number $\Pi_1\,\Pi_2$ indicate a system with little convective transport and energy input in terms of thermal energy. These systems are rapidly cooled by the ambient fluid to the fluid temperature, eliminating any temperature gradients. In this regime of thermal transport we observe the radiative flux to be of no relevance, since radiative transport is proportional to the temperature to the power of four. Another interesting finding follows from the observation that Π_1 strongly decreases with decreasing particle size (see Section 5.4). This is since the heat transfer coefficient α is (to a first approximation) proportional to the inverse of the particle size. Thus, radiative transport in fine powders will be hardly of any significance. This is simply because particles are rapidly cooled to the ambient fluid (i.e., Π_1 is small), and hence particle shielding suppresses radiative transport.

Finally, we would like to again stress that radiative fluxes can be up to 100 times larger than the conductive heat flux through a box completely filled with solid material (see our data in panel (d) of Fig. 5.22).

After presenting a collapse of data for the radiative thermal flux, we next aim on an assessment of the relative importance of the individual thermal transport modes.

5.5.5 Relative Importance of Thermal Transport Modes

It is clear that the relative contribution of the radiative flux to the total thermal flux is important for the overall thermal behaviour of a granular system. Since we take three thermal fluxes into account (conductive, convective and radiative), the relative contribution of the individual fluxes to the total flux has to be determined. With a stacked diagram, provided in Fig. 5.23, we work towards such a comparison. Thereby, the total flux is calculated as a simple summation of all contributions (compare Eqn. (5.49)). Even though we find that the radiative flux is not influenced by the particle packing fraction (see results from Sec. 5.5.2), conductive and convective show a strong dependency on the volume fraction

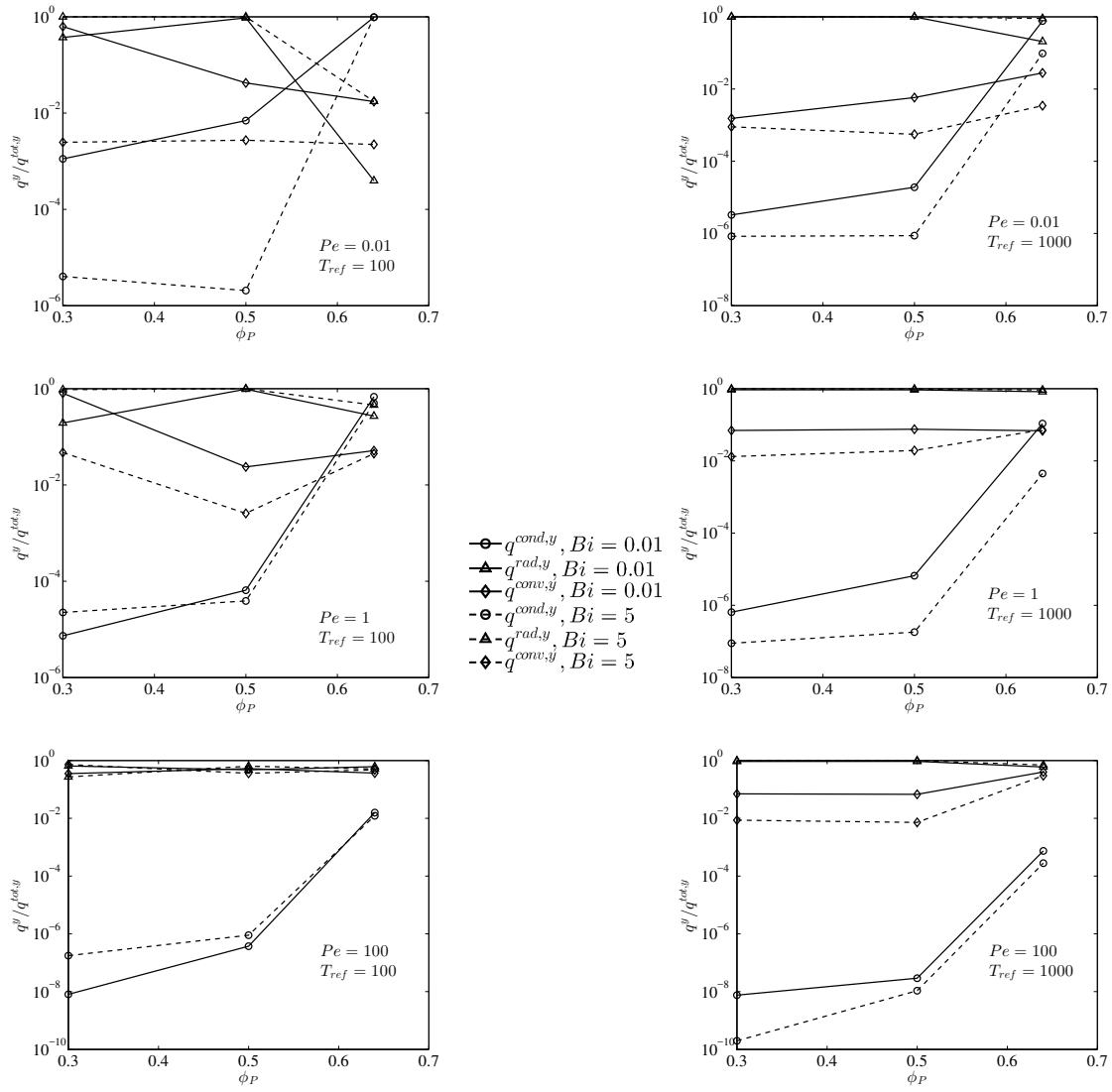

Figure 5.23: Relative contribution of each mode of thermal transport to the total flux for different dimensionless flow and thermal parameters.

(see also Forgber et al. [28]). This is of particular interest at low Peclet numbers in combination with low reference temperatures (i.e., $Pe = 0.01$, $T_{ref} = 100$). Here the relative importance of the conductive flux is strongly dependant on the particle concentration: conduction becomes the most dominant thermal transport mode for very dense systems, i.e., quasi-static flows. Only a small contribution of convective ($\sim 0.05\, q^{tot,y}$) and radiative transport modes ($\sim 0.001\, q^{tot,y}$) is observed for low Biot numbers in this case. Even in case of $Bi = 5$, the dominance is found, but decreases with rising reference temperatures

($T_{ref} = 1000$).

At higher reference temperatures, we observe the radiative flux always to add the main contribution to the total flux. Typically, the radiative transport mode is followed by the convective transport in this regime. As pointed out by Rognon et al. [30] and Forgber et al. [28], the latter becomes most important for fast shearing conditions. We agree with previous finding, also showing that the convective transport contributes a considerable amount to the total thermal transport rate for $Pe >= 1$. Nevertheless, radiation still remains dominant in all cases shown for $Pe >= 1$ and $T_{ref} >= 100$. Especially in case of fast sheared beds at high temperatures, the effect of conduction can be neglected completely. This is since the contribution drops below $\sim 1\%$.

Even though we presented certain trends, the stacked diagram shown above does not allow a rigorous calculation of the thermal fluxes. As shown in Fig. 5.23, the importance of thermal fluxes is sensitive to a large number of dimensionless parameters. A more rigorous description of these trends remains a challenge.

5.6 Conclusions

We presented a novel method to account for particle-particle radiative thermal transport in dense beds with little computational overhead based on an efficient calculation of view factors. The algorithm makes use of already available functions which are present in every discrete element methods code to detect neighbouring particles. On every particle, a fixed number of area-equidistant points is distributed and assigned to each particle-particle interaction, based on the solid angle between them. In the current developing state, the model features shadowing effects, however, assumes isotropic reflected radiation.

Next, we used a finite volume Discrete Ordinate Method (fvDOM) to generate verification data for our model. In fact, we apply the fvDOM framework, implemented in *OpenFOAM*, to generate a fixed particle bed of various volume fractions to calculate view factor. For all verification studies, we observe a small error when comparing our new model and the fvDOM results, as well as when benchmark our results against literature data. Therefore, we conclude that our newly proposed radiation algorithm can be applied in discrete element simulations of dense particle systems to predict thermal radiation fluxes.

Finally, we choose to study the radiative flux in a periodic sheared box under well controlled conditions. After a statistical steady state in terms of thermal fluxes and contact pressure is reached, we average conductive, convective and radiative fluxes in the thermal gradient (y) direction. We identify that the radiative flux is of key importance at high Peclet numbers (i.e., high speed of shearing or high thermal resistance of the particles). Here radiative transport rates can easily reach up to 100 times the reference conductive flux. In contrast to the linear scaling with the Peclet number, we find the radiative flux to be independent of the volume fraction within the studied range of solid volume fractions ($\phi_p = 0.3 - 0.64$). The newly introduced dimensionless number Π_2 allows us to scale our simulation setup from a wide range of reference temperature levels. As expected from literature data, the radiative flux reaches significant importance at high temperatures. This was also confirmed within the current study. Furthermore, we find an interesting collapse of radiative fluxes for greatly different systems parameters when plotting over a combination of the dimensionless numbers Π_1 and Π_2. This finding is significant, since it allows a rapid estimation of radiative fluxes in sheared granular materials.

It is clear that the thermal behaviour of the system should be seen as a combination of all thermal transport mechanisms. Therefore, the relative importance of the radiative flux, in comparision to conduction and convection, is finally

quantified. We find that - depending on the flow situation - all fluxes might significantly dominate the thermal behaviour of the sheared box. At high particle volume fractions, combined with slow shearing and moderately high reference temperature, the conductive thermal transfer plays a significant role. When increasing shear speed and reference temperature, the contribution through conduction decreases as radiative and convective transport gain significant importance. Generally speaking, in systems of high shear speed and high reference temperatures, radiation is the most dominant thermal transfer mechanism with negligible contribution by conduction. Nevertheless, all depicted trends should be treated with care and evaluated, since a conclusive model for predicting all relevant thermal transport rates could not be established in the present work.

Since our aim was to introduce a new modelling approach aiming towards a discrete radiation model, several open questions and future challenges can be identified. Firstly, future studies should focus on the development of wall boundary conditions for the radiative flux in continuum-based granular flow models. Secondly, a careful evaluation on the influence of the emission coefficient is needed, since our present work was confined to an emissivity of unity. Thirdly, the presented model has to be extended to poly-disperse granular media. Therefore, the correction term, applied to the solid angle, should be extended by a term taking the relative size ratio of the particles into account. Finally, we stress that the presented model can easily be integrated into any discrete element method source code since only standard routines are needed, and the additionally required memory appears to be manageable.

5.7 Nomenclature

5.7.1 Greek Characters

Variable	Unit	Meaning
α	$\mathrm{W\,m^{-2}\,K^{-1}}$	Heat transfer coefficient
α	$^\circ$	Shifting angle
β		Extinction coefficient
δ	m	Overlap distance during a particle–particle contact
$\dot{\gamma}$		Dimensionless shear rate
ϵ		Emission coefficient
ε		View factor
γ	$\mathrm{s^{-1}}$	Shear rate
μ		Friction coefficient
η	$\mathrm{N\,s\,m^{-1}}$	Viscous damping coefficient
θ	$^\circ$	Angular angle
κ		Absorption coefficient
σ_s		Scattering coefficient
ϕ		Particle volume fraction
ϕ	$^\circ$	Polar angle
Φ	$\mathrm{sr^{-1}}$	Scattering phase function
φ	$^\circ$	Solid angle
λ	$\mathrm{W\,m^{-1}\,K^{-1}}$	Thermal conductivity
ρ	$\mathrm{kg\,m^{-3}}$	Density
$\boldsymbol{\omega}$	$\mathrm{s^{-1}}$	Eigen-frequency of damped harmonic oscillator
ω_s	$\mathrm{W\,m^{-2}\,K^{-4}}$	Boltzmann constant
ω	$^\circ$	Angle, quadrature weights
Ω	sr	Solid angle in RTE equation

5.7.2 Latin Characters

Variable	Unit	Meaning
a	$\mathrm{m^2\,s^{-1}}$	Thermal diffusivity
a, b		Fitting constants
A	$\mathrm{m^2}$	Cross sectional area
c	$\mathrm{J\,kg^{-1}\,K^{-1}}$	Heat capacity
d	m	Diameter
D	m	Distance of parallel plates
e		Coefficient of restitution
E		Error
$\mathbf{f}$	N	Force on particle
H	m	Height of simulation domain
i_{break}		Fraction
I	N s	Moment of inertia
I	$\mathrm{W\,m^{-2}\,sr^{-1}\,Hz^{-1}}$	Radiative intensity
k	$\mathrm{N\,m^{-1}}$	Spring stiffness
k	$\mathrm{m^{-1}}$	Volume coefficient of absorption of the medium
N		Number of points/particles
n, m, M		Index variable
m	kg	Mass
p	Pa	Pressure
Q	W	Heat
q	$\mathrm{W\,m^{-2}}$	Heat flux
R		Particle radius ratio
r	m	Particle radius
$\mathbf{r}$	m	Relative distance vector
$\widehat{\boldsymbol{s}}$		unit vector into a given direction
s	m	Geometric path length
S		Dimensionless particle surface distance
t	s	Time
T	K	Temperature
u	m	Perimeter
$\mathbf{v}$	$\mathrm{m\,s^{-1}}$	Particle velocity
V	$\mathrm{m^3}$	Volume
Y	$\mathrm{N\,m^{-2}}$	Young's modulus
$\mathbf{x}, P$	m	Particle position

5.7.3 Superscripts

Variable	Meaning
$conv$	Convection
$cond$	Conductive
n	Normal direction
rad	Radiative value
ref	Reference value
t	Tangential direction
tot	Total value
$trans$	Transferred
x, y, z	Direction

5.7.4 Subscripts

Variable	Meaning
$absorb$	Absorb value
avg	Average Value
b	Black body value
bot	Bottom
c	Critical Value
$char$	Characteristic value
co	Contact
cor	Corrected value
$drift$	Drift value
DM	Discrete model
eff	Effective value
$equal$	Equal value
f	Fluid
$fvDOM$	Finite volume discrete ordinate method
i, j	Index
in	Intrinsic value
int	Intermediate
$inert$	Inertial
max	Maximum value
p	Particle
p	Points
QS	Quasi-static
$reflect$	Reflected value
ref	Reference value
top	Top
vol	Volumetric Value
x, y, z	Directions

Appendices

Table 5.4: Boundary conditions used for the fvDOM setup in *OpenFOAM*.

Field/Patch	Quantity	Type/Value
Lateral walls/ absorbing particles	Emissivity	0
	Temperature	Fixed value
Emitting sphere surface/ parallel walls	Emissivity	1
	Temperature	Fixed Value

Table 5.5: Adjusted DEM parameters.

$\dot{\gamma}$	Y_{eff}	$\triangle t$
10^{-3}	$1.32 \cdot 10^{8}$	$2.5\,10^{-5}$
10^{-4}	$4.18 \cdot 10^{10}$	$2.5\,10^{-6}$

Appendix A: DEM Parameters and Calculation Routines

The normal spring stiffness and the coefficient of restitution were set by adjusting the effective Young's modulus Y_{eff} and the damping coefficient η. Thus, the following equations were applied:

$$k = \frac{16}{15}\sqrt{r_{eff}}\,Y_{eff}\left(\frac{15\,m_{eff}\,v_{char}^2}{16\sqrt{r_{eff}}\,Y_{eff}}\right)^{1/5}, \tag{5.59}$$

$$Y_{eff} = \left[\frac{(\gamma/\dot{\gamma})^2 d_p^3 \rho_p}{(16/15)^{4/5}(r_{eff})^{2/5}(m_{eff})^{1/5}(v_{char})^{2/5}}\right]^{5/4}, and \tag{5.60}$$

$$\eta = \sqrt{\frac{4\, m_{eff}\, k}{1 + \left(\frac{\pi}{\ln(e)}\right)}} \tag{5.61}$$

Note that the characteristic impact velocity v_{char} drops out of Eqn. (5.59) after inserting Eqn. (5.60) and therefore is irrelevant for the subsequent dimensional analysis. Tab. (5.5) outlines the adjusted parameter in order to obtain the dimensionless shear rate $\dot{\gamma}$.

5.8 Bibliography

[1] T. Forgber and S. Radl. A novel approach to calculate radiative thermal exchange in coupled particle simulations. *submitted to Powder Technology*, 2017.

[2] J. C. Chen, J. R. Grace, and M. R. Golriz. Heat transfer in fluidized beds: design methods. *Powder Technology*, 150(2):123–132, 2005.

[3] D. Baillis and J.-F. Sacadura. Thermal radiation properties of dispersed media: theoretical prediction and experimental characterization. *Journal of Quantitative Spectroscopy and Radiative Transfer*, 67(5):327–363, 2000.

[4] N. Decker and L. R. Glicksman. Heat transfer in large particle fluidized beds. *International Journal of Heat and Mass Transfer*, 26(9):1307–1320, 1983.

[5] A. Goshayeshi, J. R. Welty, R. L. Adams, and N. Alavizadeh. Local Heat Transfer Coefficients for Horizontal Tube Arrays in High-Temperature Large-Particle Fluidized Beds: An Experimental Study. *Journal of Heat Transfer*, 108(4):907–912, 1986.

[6] C. L. Tien. Thermal Radiation in Packed and Fluidized Beds. *Journal of Heat Transfer*, 110(4b):1230–1242, 1988.

[7] R. Dayal. *Numerical Modelling of Processes Governing Selective Laser Sintering*. PhD thesis, Technische Universität, Darmstadt, 2014.

[8] M. Kaviany. *Principles of Heat Transfer in Porous Media*. Springer-Verlag New York, 1 edition, 1991.

[9] J. C. Chen and S. W. Churchill. Radiant heat transfer in packed beds. *AIChE Journal*, 9(1):35–41, 1963.

[10] S. Yagi and D. Kunii. Studies on effective thermal conductivities in packed beds. *AIChE Journal*, 3(3):373–381, 1957.

[11] G. J. Cheng, A.B. Yu, and P. Zulli. Evaluation of effective thermal conductivity from the structure of a packed bed. *Chemical Engineering Science*, 54(19):4199–4209, 1999.

[12] M.-H. Fillion, J. Côté, and J.-M. Konrad. Thermal radiation and conduction properties of materials ranging from sand to rock-fill. *Canadian Geotechnical Journal*, 48(4):532–542, 2011.

[13] A. Jagota and C. Y. Hui. The Effective Thermal Conductivity of a Packing of Spheres. *Journal of Applied Mechanics*, 57(3):789–791, 1990.

[14] D. Kunii and J. M. Smith. Heat transfer characteristics of porous rocks. *AIChE Journal*, 6(1):71–78, 1960.

[15] A. G. Dixon. Heat transfer in fixed beds at very low tube-to-particle diameter ratio. *Industrial and Engineering Chemistry Research*, 36(8):3053–3064, 1997.

[16] C. Di Blasi. Heat, momentum and mass transport through a shrinking biomass particle exposed to thermal radiation. *Chemical Engineering Science*, 51(7):1121–1132, 1996.

[17] K. W. Ragland, D. J. Aerts, and A. J. Baker. Properties of wood for combustion analysis. *Bioresource Technology*, 37(2):161–168, 1991.

[18] K. M. Bryden, K. W. Ragland, and C. J. Rutland. Modeling thermally thick pyrolysis of wood. *Biomass and Bioenergy*, 22(1):41–53, 2002.

[19] F. C. Lockwood and N. G. Shah. A new radiation solution method for incorporation in general combustion prediction procedures. *Symposium (International) on Combustion*, 18(1):1405–1414, 1981.

[20] S. Hostikka and K. B. McGrattan. Large Eddy Simulation of Wood Combustion. In *Interflam*, pages 755–762, 2001.

[21] J. D. Cartigny, Y. Yamada, and C. L. Tien. Radiative Transfer With Dependent Scattering by Particles: Part 1—Theoretical Investigation. *Journal of Heat Transfer*, 108(3):608–613, 1986.

[22] J. R. Howell, R. Siegel, S. Heights and M. P. Menguc. *Thermal Radiation Heat Transfer*. CRC Press, 5th edition, 2010.

[23] T. F. Ozkaynak, J. C. Chen, and T. R. Frankenfield. An experimental investigation of radiant heat transfer in high temperature fluidized bed. In *Proc. 4th International Conference on Fluidization*, pages 371–378, 1983.

[24] C. Kloss, C. Goniva, A. Hager, S. Amberger, and S. Pirker. Models , algorithms and validation for opensource DEM and CFD-DEM. *Progress in Computational Fluid Dynamics*, 12:140–152, 2012.

[25] G. Toschkoff, S. Just, K. Knop, P. Kleinebudde, A. Funke, D. Djuric, G. Scharrer, and J. G. Khinast. Modeling of an active tablet coating process. *Journal of Pharmaceutical Sciences*, 104(12):4082–4092, 2015.

[26] S. Amberger, S. Pirker, and C. Kloss. Thermal radiation modeling using ray tracing in liggghts. In *6th International Conference on Discrete Element Methods (DEM6)*, 2013.

[27] T. I. Zohdi. A discrete element and ray framework for rapid simulation of acoustical dispersion of microscale particulate agglomerations. *Computational Mechanics*, 57(3):465–482, 2016.

[28] T. Forgber, B. Mohan, C. Kloss, and S. Radl. Heat transfer rates in sheared beds of inertial particles at high biot numbers. *Granular Matter*, 19(1):14, 2017.

[29] T. Forgber and S. Radl. Heat transfer rates in wall bounded shear flows near the jamming point accompanied by fluid-particle heat exchange. *Powder Technology*, 315:182 – 193, 2017.

[30] P. Rognon and I. Einav. Thermal transients and convective particle motion in dense granular materials. *Phys. Rev. Lett.*, 105:218301, 2010.

[31] S. Chialvo, J. Sun, and S. Sundaresan. Bridging the rheology of granular flows in three regimes. *Physical Review E - Statistical, Nonlinear, and Soft Matter Physics*, 85:021305, 2012.

[32] B. Mohan, C. Kloss, J. Khinast, and S. Radl. Regimes of Liquid Transport through Sheared Beds of Inertial Smooth Particles. *Powder Technology*, 264:377–395, 2014.

[33] M. F. Modest. *Radiative Heat Transfer*. Academic Press, Boston, 3rd edition, 2013.

[34] J. M. Hammersley and D. C. Handscomb. *Monte Carlo Methods*. John Wiley and Sons, London, 1st edition, 1964.

[35] A. Haji-Sheikh. *Monte Carlo Methods*. John Wiley and Sons, New York, 1988.

[36] C. E. Lee. The discrete s-n approximation to transport theory. Technical report, Information Series Report LA2595, Lawrence Livermore Laboratory, 1962.

[37] T. J. Love and R. J. Grosh. Radiative heat transfer in absorbing, emitting, and scattering media. *ASME Journal of Heat Transfer*, 87:161–166, 1965.

[38] H. M. Hsia and T. J. Love. Radiative heat transfer between parallel plates separated by a nonisothermal medium with anisotropic scattering. *ASME Journal of Heat Transfer*, 89(3):204–204, 1967.

[39] H. C. Hottel, A. F. Sarofim, L. B. Evans, and I. A. Vasalos. Radiative transfer in anisotropically scattering media: Allowance for fresnel reflection at the boundaries. *ASME Journal of Heat Transfer*, 90:56–62, 1968.

[40] D. C. Todd Roux, J. A. and A. M. Smith. Radiative transport analysis for plane geometry with isotropic scattering and arbitrary temperature. *AIAA Journal*, 12(9):1273–1277, 1974.

[41] S. C. Mishra and M. Prasad. Radiative heat transfer in participating media - a review. *Sadhana*, 23(2):213, 1998.

[42] W. A. Fiveland. Discrete ordinates solutions of the radiative transport equation for rectangular enclosures. *ASME Journal of Heat Transfer*, 106:699–706, 1984.

[43] J. S. Truelove. Discrete-ordinate solutions of the radiation transport equation. *ASME Journal of Heat Transfer*, 109:1048–1051, 1987.

[44] P. J. Coelho. Advances in the discrete ordinates and finite volume methods for the solution of radiative heat transfer problems in participating media. *Journal of Quantitative Spectroscopy and Radiative Transfer*, 145:121–146, 2014.

[45] M. R. J. Charest, C. P. T. Groth, and O. L. Gülder. Solution of the equation of radiative transfer using a newton-krylov approach and adaptive mesh refinement. *Journal of Computational Physics*, 231(8):3023–3040, 2012.

[46] J. D. Felske. Approximate radiation shape factors between spheres. *Journal of Heat Transfer*, 100(3):547–548, 1978.

[47] L. R. Jones. Diffuse radiation view factors between two spheres,. *Journal of Heat Transfer*, 87(3):421–422, 1965.

[48] Y. A. Cengel and A. J. Ghajar. *Heat and Mass Transfer : Fundamentals and Applications*. McGraw-Hill Education, Singapore, 5th edition, 2015.

[49] https://github.com/CFDEMproject/ParScale-PUBLIC, accessed May 2017.

[50] S. Radl, T. Forgber, A. Aigner, and C. Kloss. ParScale - An Open-Source Library for the Simulation of Intra-Particle Heat and Mass Transport Processes in Coupled Simulations. *IV International Conference on Particle-based Methods – Fundamentals and Applications (PARTICLES 2015)*, pages 46–55, 2015.

[51] T. Forgber, J. R. Tolchard, A. Zaabout, P. I. Dahl, and S. Radl. Optimal Particle Parameters for CLC and CLR Processes - Predictions by Intra-Particle Transport Models and Experimental Validation. *IV International Conference on Particle-based Methods – Fundamentals and Applications (PARTICLES 2015)*, pages 101–111, 2015.

[52] http://computation.llnl.gov/projects/sundials/cvode, accessed January 2017.

[53] S. D. Cohen, A. C. Hindmarsh, and P. F. Dubois. CVODE, A Stiff/Nonstiff ODE Solver in C. *Computers in Physics*, 10:138–148, 1996.

[54] A. L. Crosbie and R. G. Schrenker. Radiative transfer in a two-dimensional rectangular medium exposed to diffuse radiation. *Journal of Quantitative Spectroscopy and Radiative Transfer*, 31:339–372, 1984.

[55] A. Amouzandeh, S. Shrestha, M. Zeiml, and R. Lackner. Development of a Computational Fluids-DynamicsTool to Predict the Thermal Load of Structures in Case of Fire. In *Proceedings of the Open Source CFD International Conference*, pages 1–14, 2009.

[56] T. Hatano. Scaling properties of granular rheology near the jamming transition. *Journal of the Physical Society of Japan*, 77(12):18–21, 2008.

[57] M. Otsuki and H. Hayakawa. Critical behaviors of sheared frictionless granular materials near the jamming transition. *Physical Review E - Statistical, Nonlinear, and Soft Matter Physics*, 80:011308, 2009.

[58] F. Alonso-Marroquín, I. Vardoulakis, H. J. Herrmann, D. Weatherley, and P. Mora. Effect of rolling on dissipation in fault gouges. *Physical Review E - Statistical, Nonlinear, and Soft Matter Physics*, 74:031306, 2006.

[59] K. N. Nordstrom, E. Verneuil, P. E. Arratia, Z. Zhang, G. Yodh, J. P. Gollub, and D. J. Durian. Microfluidic rheology of soft colloids above and below jamming. *Physical Review Letters*, 105:175701, 2010.

6 Conclusion and Outlook

6.1 Conclusion

Within this thesis, several major achievements could be accomplished. In Chapter 3 *ParScale* was introduced, including a summary of governing equations, verification cases and coupling routines. The approach to use spherical coordinates, i.e., to rely on a simplified one-dimensional discretization in the radial direction only, could be verified with results from direct numerical simulations. An analytical solution for the average particle temperature in a cooled particle bed is presented, and evaluated for certain limiting cases. In the following, *ParScale* is linked to *LIGGGHTS* and intra-particle temperature profiles are resolved in a quasi steady-state, fully periodic (unbounded) granular shear flow. Based on the collected result for the particle- and time-averaged thermal fluxes it was shown that (i) a global minimum of the convective flux at the critical volume fraction exists, and that (ii) the thermal behavior of sheared granular materials can be categorized in three different regimes, similar as for the contact pressure. While the inspiration for the collapse of the conductive transport into three regimes is taken from Chialvo et al. [1], it extends the work of Rognon et al. [2]. His study was limited to a fixed volume fraction (but included various particle stiffness and thermal numbers) which limits his findings of a nearly constant conductive flux. Thereby, the particle stiffness dictates to a significant extent the conductive flux in more dilute flows, and has only a minor effect on this flux at high particle volume fractions (and fixed particle concentration). The importance of resolving intra-particle temperature profiles in strongly cooled systems could be successfully proven and results are presented over a wide range of parameters. Until now only little work was done under the assumption resolved internal particle temperatures (e.g. Oschmann et al. [3] and Schmidt et al. [4]). The mentioned publications focused on thermal fluxes and inhomogeneities in combination with resolved particle temperatures but were limited to fixed particle arrangements or two-dimensional approaches. Nevertheless, the findings of Oschmann et al. [3] support our conclusions that thermal fluxes and therefore the effective thermal conductivity is affected when relying on unresolved particle temperatures.

In Chapter 4, *ParScale* is applied to a bounded shear flow, driven by moving walls with a constant velocity. Thereby, it was shown that the state of the granular system (i.e., unjammed, jammed or crystallized) can be characterized only by considering the conductive thermal flux. The critical jamming volume fraction is independent of the speed of shearing (i.e., the Peclet number) and for a linear spring-dashpot model, a linear scaling of the conductive thermal flux in combination with the Biot number is found over the dimensionless contact pressure. Surprisingly, this scaling is found to be valid over five orders of magnitude. A simple explanation of this robust scaling is that an increase of the conductive flux must be caused by an increase of the average particle-particle overlap, which is proportional to the contact pressure. Most important, the convective flux stays nearly unaffected by the jamming transition, i.e., this thermal flux is not a function of the contact pressure.

Chapter 5 introduces a new algorithm to estimate radiative thermal exchange rates between discrete particles based on the solid angle. A successful verification against literature data, as well as data generated using a finite volume Discrete Ordinate Method for a static particle bed is performed. The algorithm is embedded into the DEM solver *LIGGGHTS* to enable simulations of radiative thermal exchange in moving particle beds. The aim was to quantify the importance of the radiative heat transport mode over a wide range of system parameters, and to outline scenarios in which radiation is of major importance and the leading transport mechanism. Thereby, good agreement with literature data (i.e. Felske [5] and Jones [6]) was found for simple verification cases and the dominance of radiation at high temperatures could be confirmed as mentioned by e.g. Glicksman et al. [7], [8] and Goshayeshi et al. [9]. Furthermore, a relative evaluation of conductive, convective and radiative thermal fluxes for a variety of flow situations is presented, and a successful collapse of the normalized radiative flux over an appropriate dimensionless group is identified.

The next Section gives an outlook in terms of ideas for follow-up work, and future challenges that could be attacked with the developed software.

6.2 Outlook

Since the aim of the thesis was to introduce new modeling approaches, several open questions, future challenges and ideas for follow-up work can be identified.

There is a latent need to account for the area which is covered in case of particle-particle contacts when calculating the heat transferred to the ambient fluid. Currently, this transferred heat flux is calculated based on the entire particle surface. Certainly, a strong limitation of the presented simulation setup arises with the fixed temperature for the surrounding fluid. A more advanced setup would be to couple the simulation setup to a CFD solver. Then, one could use drag correlations and the resolved temperature field to compute relevant forces and heat source (or sink) terms on the particles.

Moving to the presented radiation model, there is a clear need for boundary conditions for the radiative flux from walls. Such a boundary condition could be based on the local particle volume fraction close to a wall, as well as the wall normal position of a particle. Furthermore, studies that quantify the effect of an emission coefficient different from unity have to be performed. Finally, the algorithm should to be extended to poly-disperse granular materials. Consequently, the correction term for the solid angle has to account for the relative size ratio of particles, as well as the size of the shadowing particle. Finally, it has to be pointed out that some researchers are already actively using *ParScale* and consequently the development should be speed up to allow the simulation of more general systems. For example, implementing particle properties that depend on the local particle temperature, or offering more complex porosity and diffusion models could critically impact the future usage of *ParScale*.

6.3 Bibliography

[1] S. Chialvo, J. Sun, and S. Sundaresan. Bridging the rheology of granular flows in three regimes. *Physical Review E - Statistical, Nonlinear, and Soft Matter Physics*, 85:021305, 2012.

[2] P. Rognon and I. Einav. Thermal transients and convective particle motion in dense granular materials. *Phys. Rev. Lett.*, 105:218301, 2010.

[3] T. Oschmann, M. Schiemann, and H. Kruggel-Emden. Development and verification of a resolved 3D inner particle heat transfer model for the discrete element method (DEM). *Powder Technology*, 291:392–407, 2015.

[4] R. Schmidt and P. Nikrityuk. Numerical simulation of the transient temperature distribution inside moving particles. *The Canadian Journal of Chemical Engineering*, 90:246–262, 2012.

[5] J. D. Felske. Approximate radiation shape factors between spheres. *Journal of Heat Transfer*, 100(3):547–548, 1978.

[6] L. R. Jones. Diffuse radiation view factors between two spheres,. *Journal of Heat Transfer*, 87(3):421–422, 1965.

[7] N. Decker and L. R. Glicksman. Heat transfer in large particle fluidized beds. *International Journal of Heat and Mass Transfer*, 26(9):1307–1320, 1983.

[8] D. Gloski, L. Glicksman, and N. Decker. Thermal resistance at a surface in contact with fluidized bed particles. *International Journal of Heat and Mass Transfer*, 27(4):599–610, 1984.

[9] A. Goshayeshi, J. R. Welty, R. L. Adams, and N. Alavizadeh. Local Heat Transfer Coefficients for Horizontal Tube Arrays in High-Temperature Large-Particle Fluidized Beds: An Experimental Study. *Journal of Heat Transfer*, 108(4):907–912, 1986.

7 Publication List

7.1 Peer-Review Articles

- T. Forgber, B. Mohan, C. Kloss, and S. Radl. Heat transfer rates in sheared beds of inertial particles at high biot numbers. *Granular Matter*, 19(1):14, 2017.
- T. Forgber and S. Radl. Heat transfer rates in wall bounded shear flows near the jamming point accompanied by fluid-particle heat exchange. *Powder Technology*, 315:182 – 193, 2017.
- T. Forgber and S. Radl. A novel approach to calculate radiative thermal exchange in coupled particle simulations. *submitted to Powder Technology*, 2017.

7.2 Conference Articles

- T. Forgber, J. R. Tolchard, A. Zaabout, P. I. Dahl, and S. Radl. Optimal Particle Parameters for CLC and CLR Processes - Predictions by Intra-Particle Transport Models and Experimental Validation. *IV International Conference on Particle-based Methods – Fundamentals and Applications (PARTICLES 2015)*, pages 101–111, 2015.
- S. Radl, T. Forgber, A. Aigner, and C. Kloss. ParScale - An Open-Source Library for the Simulation of Intra-Particle Heat and Mass Transport Processes in Coupled Simulations. *IV International Conference on Particle-based Methods – Fundamentals and Applications (PARTICLES 2015)*, pages 46–55, 2015

7.3 Technical Reports

- T. Forgber T., F. Municchi, R. Pichler, and S. Radl. Strömungstechnische Kriterien für die Projektierung und den Betrieb spezieller Reinraumkomponenten. Technical report, 2015

- T. Forgber, F. Municchi, and S. Radl. Investigation of Leakage Rates and Flow in a Wafer Washing Unit. Technical report, 2016.